N° d'ordre : 40879

UNIVERSITE LILLE 1 - SCIENCES ET TECHNOLOGIES (France)
UNIVERSITE DE TECHNOLOGIE DE WROCLAW (Pologne)

THESE en cotutelle

présentée par

LESZEK LATKA

pour l'obtention du

GRADE DE DOCTEUR EN MECANIQUE
de l'Université de Lille et de l'Université de Wroclaw

intitulée

Développement de la projection plasma de suspension de dépôts d'hydroxyapatite, d'oxyde de titane et de zircone yttriée et leur caractérisation mécanique.

Soutenue à Wroclaw, le **30 Novembre 2012** devant le jury d'examen :

Directeurs de Thèse FRANCE : ***Pr. Lech PAWLOWSKI (Université de Limoges)***
Pr. Didier CHICOT (Université de Lille 1)

Directeurs de Thèse POLOGNE : ***Pr. Andrzej AMBROZIAK (Université de Wroclaw)***
Dr. Stefan KOZERSKI (Université de Wroclaw)

Rapporteurs : ***Pr. Eli Saul PUCHI-CABRERA (Université de Caracas – Venezuela)***
Pr. Thomas LAMPKE (Université de Chemnitz – Allemagne)
Pr. Zbigniew MIRSKI (Université de Wroclaw – Pologne)

to my Beloved Wife

CONTENT

LIST OF ABBREVIATIONS

APS	Atmospheric Plasma Spraying
AS	Arc Spraying
BSE	Back-Scattered Electrons
CAPS	Controlled Atmosphere Plasma Spraying
CGMS	Cold Gas Method Spraying
CVD	Chemical Vapor Deposition
DC	Direct Current
DEO	Design of Experiment
D-Gun™	Detonation Gun Spraying
FS	Flame Spraying
GND	Geometrically Necessary Dislocations
HA	Hydroxyapatite, $(Ca_{10}(PO_4)_6(OH)_2)$
HIT	Contact hardness
HM	Martens hardness
HVOF	High Velocity Oxy Fuel spraying
IIT	Instrumented Indentation Tests
IPS	Inert Atmosphere Plasma Spraying
ISE	Indentation Size Effect
JCPDS	Joint Committee on Powder Diffraction Standards
MB	Methylene Blue
PSR	Proportional Specimen Resistance
PVD	Physical Vapor Deposition
RF	Radio Frequency
RT	Room temperature
SBF	Simulated Body Fluid
SE	Secondary Electrons
SEM	Scanning Electron Microscope
SGP	Strain Gradient Plasticity
slpm	Standard liter per minute

SOFC	Solid oxide fuel cell
SPPS	Solution Precursor Plasma Spraying
SPS	Suspension Plasma Spraying
TBC	Thermal Barrier Coating
TCP	Tri-calcium Phosphate
TEM	Transmission Electron Microscopy
TTCP	Tetra-calcium Phosphate
UV	Ultraviolet
VPS	Vacuum Plasma Spraying
YCSZ	Yttria with Ceria Stabilized Zirconia
YSZ	Yttria Stabilized Zirconia
XRD	X-ray Diffraction

LIST OF SYMBOLS

LATIN SYMBOLS

a	thermal diffusivity; lattice parameter
A	representative area of the residual indent
A_c	projected contact area
b	Burger's vector; lattice parameter
B	fitting parameter (used in eq. 3.3)
c	lattice parameter
c_p	specific heat
C_A	content of anatase
C_{Acor}	corrected content of anatase
C_f	frame compliance
C_T	total compliance
d	diagonal of Vickers indent; scratch width; sample thickness; length of cell for spectroscopic measurements
d_{VS}	volume to surface main diameter
E_i	elastic modulus of diamond indenter
E_m	elastic modulus of tested material
E_P	photon irradiance
E_R	reduced modulus
f	corrective factor (used in eq. 3.9); content of ingredient (used in eq. 2.6)
H	hardness number
H_0	macrohardness
h	corrected indentation depth (used in eq. 3.20)
h^*	characteristic scale-length
h_c	contact indentation depth
h_f	fitting parameter (used in eq. 3.3)
h_m	maximum indentation depth
h_{meas}	measured indentation depth

h_r	residual indentation depth
H_{LSF}	hardness length-scale factor
HS_L	scratch hardness (used in scratch test)
HV	Vickers hardness
I_A	intensity of anatase (101) peak
I_R	intensity of rutile (110) peak
l_c	coating thickness (used in eq. 2.2)
L	large diagonal of the Knoop indent
L_C	critical load (used in scratch test)
m	fitting parameter (used in eq. 3.3)
n	exponent (used in eq. 3.13)
P	applied load in instrumented indentation test; porosity
P_0	initial deviation in the applied load
P_{max}	maximum applied load in instrumented indentation test
Q_0	absorbed energy density
R_a	average roughness, defined as the arithmetical average of the absolute values of the amplitudes of the surface with regard to a mean line along the measured distance
R_{dark}	specific degradation of MB in the dark
R_{max}	maximum roughness, defined as the deepest valley in the surface inside the measured distance
R_{irr}	specific degradation of MB during UV irradiation
R_z	average roughness – a mean of the absolute values of five greatest heights and five greatest cavities on a surface
rpm	rotations per minute
S	slope of the unloading part of the load-depth curve; surface of coating
$t_{0.5}$	half rise time
V	volume of the solution

GREEK SYMBOLS

β	corrective factor (used in eq. 3.19)
γ	corrective factor (used in eq. 3.19)
Γ	reflection coefficient at the interface between coating and surface
ΔA	variation of the absorbance of MB
$\Delta L/L$	thermal dilatation
ε	shape parameter of indent; molar extinction coefficient of MB
ε_c	thermal effusivity of coating
ε_s	thermal effusivity of substrate
ζ	zeta potential
ζ_{MB}	photon efficiency
θ	angle between the surface of the conical indenter and the plane of the surface
λ	thermal conductivity
μ	shear modulus
ν_i	Poisson’s ratio of diamond indenter
ν_m	Poisson’s ratio of tested material
ρ	density
ρ_{300}	apparent density
ρ_A	density of anatase
ρ_R	density of rutile
ρ_s	density of statistically stored dislocation

LIST OF FIGURES

LIST OF TABLES

CHAPTER 1

INTRODUCTION

1.1. THERMAL SPRAYING

Thermal spraying is one of many techniques of coating depositions, whose main types are presented in Fig. 1.1. Besides thermal spraying other methods are used, such as chemical and physical vapor deposition, CVD and PVD, respectively. At thermal spraying used material, a mainly powder, is melted by high temperature jet or flame and then these droplets hit onto substrate [1].

Among many techniques of coating deposition thermal spraying has the greatest range of coating materials, thicknesses as well as possible coatings applications and characteristics [2].

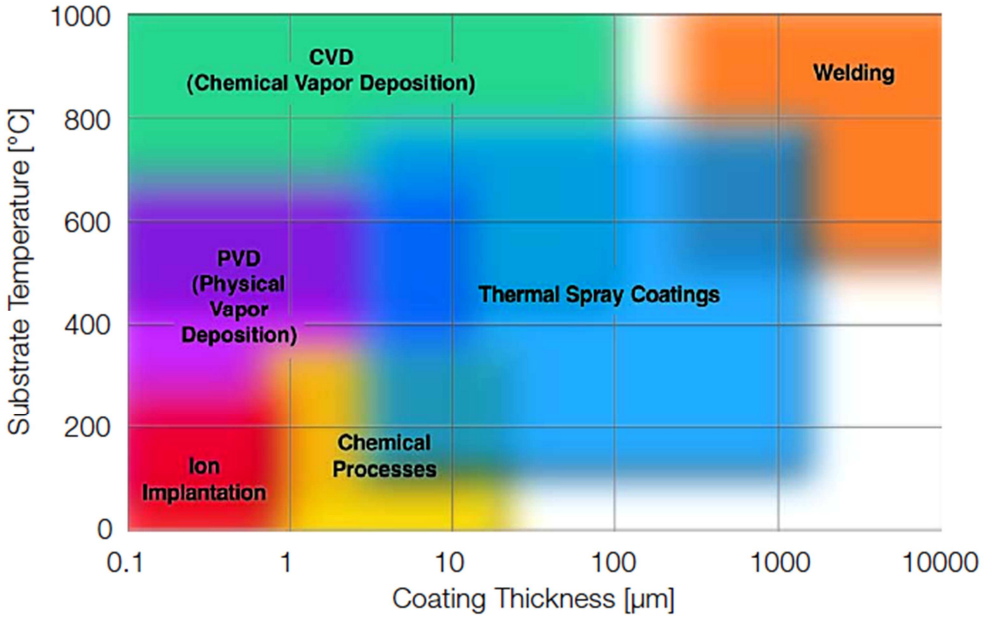

Fig. 1.1. Coating process comparison [2].

In the area of thermal spraying there are many techniques, which can be characterized by the temperature of the jet or flame (from about 3000 K to even 20000 K) and by the velocities of sprayed particles of sprayed material (from about 100 m/s to even up 1000 m/s). The main methods of thermal spraying are presented in Fig. 1.2. In all thermal spraying processes the adopted energy source should provide sufficient amount of energy to melt the sprayed material. On the other hand, this source is used to accelerate material onto substrate by transfer kinetic energy [3].

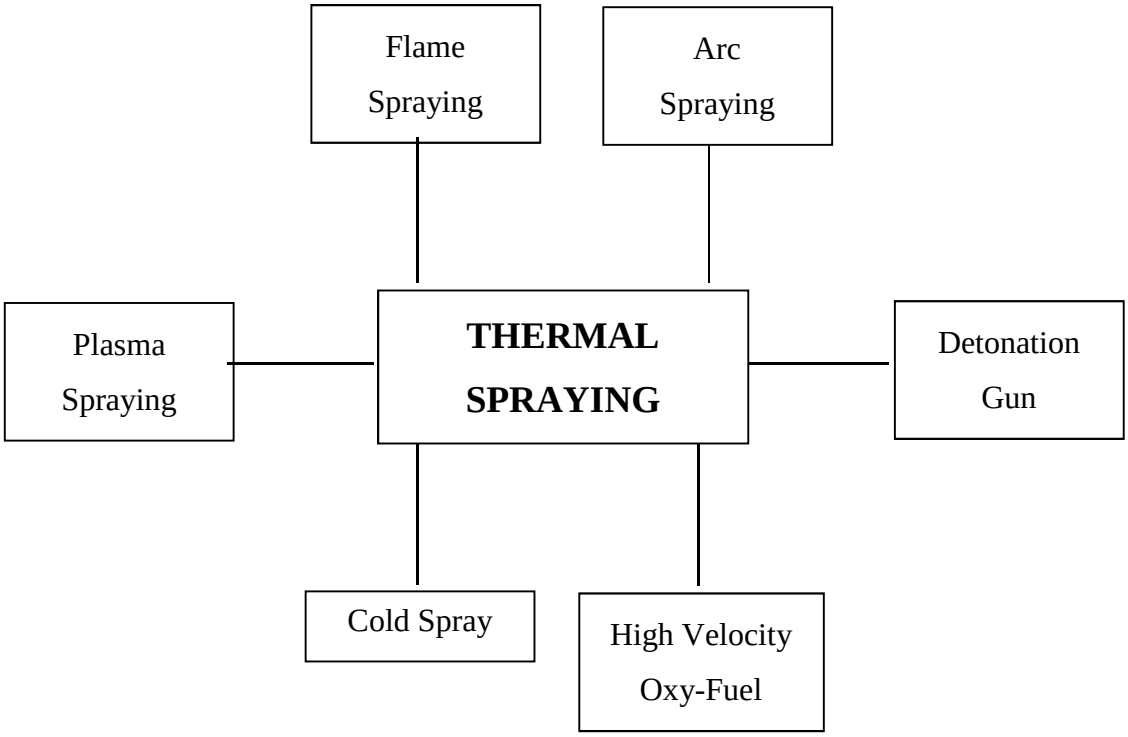

Fig. 1.2. Fundamental thermal spraying techniques.

Different thermal spray techniques used in industry are briefly described below.

Flame Spraying (FS)

This technique is also called combustion flame spraying, because of using combustion energy of the fuel gas burnt out in oxygen to melt the material in a hot flame. The temperatures are in the range from 3000 to 3350 K, while velocity of the flame ranges from 80 to 100 m/s.

Arc Spraying (AS)

In this technique melting of the material is realized by an electric arc, which is ignited between electrodes. These electrodes are wires of spray material. Molten particles are accelerated onto a substrate. The arc temperature may reach 6100 K and particle velocity is up to 150 m/s. This process can be used only for electrically conducting materials.

Detonation Gun (D-Gun)

This kind of thermal spraying is used to produce very dense coatings. The mixture of gases, oxygen with fuel one (acetylene, propane, butane are mostly used) is fed into the long barrel. Explosion is ignited by a spark plug. The maximum temperature of combustion gas is 4500 K. Particle velocity can even reach up to 1000 m/s, which is caused by detonation wave.

High Velocity Oxy-Fuel spraying (HVOF)

In this technique, fuel (acetylene, kerosene, propylene, etc.) and oxygen are fed into a combustion chamber, where hot and high pressure flame is produced, which is form by a nozzle to increase velocity. It results in very high particle velocity, which may reach up to 2000 m/s. The temperature of flame is similar to the one of flame spraying.

Cold Spray

This technique bases on compression of gas (commonly helium or nitrogen), which is heated up to 700 K, compressed to very high pressure and then it expands. The gas is fed through a special nozzle and accelerates particles to very high velocity, being in range of 1500 m/s.

Plasma Spraying (PS)

This technique is described in detail in the next part of the chapter.

1.2. PLASMA SPRAYING

Plasma spraying is at present well understood, and seems to be the most popular among all thermal spraying processes. The temperature of plasma jet reaches the temperature up to about 20000 K, melts sprayed particles and accelerate them to the velocity about 800 m/s. The plasma is generated in Direct Current (DC) or Radio Frequency (RF) torches [3]. The following techniques can be distinguished:

- Atmospheric Plasma Spraying (APS)
- Vacuum Plasma Spraying (VPS)
- Controlled Atmosphere Plasma Spraying (CAPS)
- Inert Atmosphere Plasma Spraying (IPS)
- High Pressure Plasma Spraying (HPPS)

The principle of plasma spraying is shown schematically in Fig. 1.3. The energy source in plasma spraying techniques is an electric arc, which is ignited between a nozzle (which is an anode, made from cooper) and a cathode (made from tungsten). This arc is used to heat up working gases, mostly mixtures of argon, hydrogen, helium and nitrogen. These gases are ionized and transformed into plasma. In plasma spraying different gases are used. Table 1.1 shows the main physical parameters of these gases. The torch, used in plasma spraying, is intensively cooled by water, which prevents electrodes from melting.

Table 1.1. Main physical parameters of gases used for plasma spraying [3].

Physical parameter	Ar	He	H_2	H	N_2
Density, kg/m^3	1.780	0.178	0.098	–	1.250
Energy of ionization, eV	15.7	24.9	15.4	13.6	14.5
Energy of dissociation, J/mol	–	–	$4.3 \cdot 10^5$	–	$9.4 \cdot 10^5$
Specific heat, J/(mol·K)	21	21	35	–	–
Thermal conduction coefficient at 6000 K, W/(m·K)	0.17	1.50	2.00	3.80	–

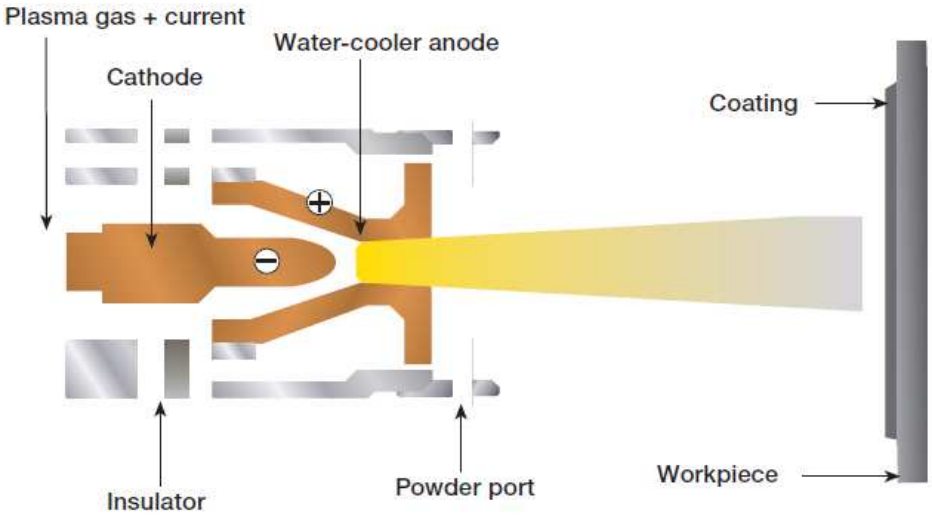

Fig. 1.3. Schematic diagram of the plasma spray process [2].

In these techniques powder is the most often sprayed material and it is transported by additional carrier gas, mostly argon. Injection of the powder is realized by radial or axial feed, inside or outside mode. The average size of the used powder is in range from 20 to 90 μm, sometimes it can reach can reach 150 μm, in important applications [1].

CHAPTER 2

SUSPENSION PLASMA SPRAYING

2.1. INTRODUCTION

Due to their very interesting mechanical, electrical, physical and optical properties, nanostructured materials have been intensively studied since the nineties of the last century. According to the definition, the nanostructured materials have crystals smaller than 100 nm [4]. Such small grains modify properties of materials, e.g. ceramics become slightly ductile [5]. Strengthening of metallic materials results from that the nanophased metals are nearly dislocation-free. Improvement of nanostructured materials in strength, resistance to wear and thermal shock, reduction of micro-cracking caused increasing interest in research and possible applications of such materials [6]. More generally, mechanical properties are dependent on the presence of defects in material or its formation facility. Initiation of defects is more difficult, when dimensions of grains are smaller. It results in changing mechanical properties. Uncommon features, such as plasticity or ductility result from huge a quantity of interfacial boundaries. Most probably, these phenomena are the result of diffusion and slippage in grains boundaries. One of the most remarkable property in nanostructured materials is superplasticity. It is huge deformation during tension without damage [7].

Surface engineering is one of the most growing branches of nanoscience. Coatings based on nanostructured materials are mainly produced with vapor condensation methods, such as physical vapor deposition, *PVD* and chemical vapor deposition, *CVD* and similar methods [5]. These methods make it possible to obtain rather thin coating, with a thickness generally not greater than a few micrometers. On the other hand, conventional thermal spraying techniques, especially plasma spraying, allow us to deposit thick coatings, even over 1 mm, with good efficiency. But these coatings haven't nanostructured architecture [6]. Other problems are connected with transporting and feeding of fine and dry particles, even in a

submicrometric range, smaller than 10 μm. Also the injection of such small powder particles and penetration of a jet or flame imply difficulties. This results from a smaller mass of particles and, consequently lower momentum causing that fine particles are moved in the colder and outer zones of the plasma jet. One proposition to solve this problem was proposed using a greater carrier (transport) gas flow rate. But it was not practical because it resulted in plasma jet cooling [8].

Completely different solution was proposed by a group from Sherbrooke University, about fifteen years ago. They developed a new technique, in which fine particles are transported into the plasma jet, or flame, by liquid transport media, such as a suspension or a solution [9]. In this technique, visualized in Fig. 2.1, the liquid including solid fraction is injected into a hot temperature zone. Suspension and solution thermal spraying techniques make it possible to obtain finely structured, even nanostructured, coatings with thickness from a few up to hundreds of micrometers [6].

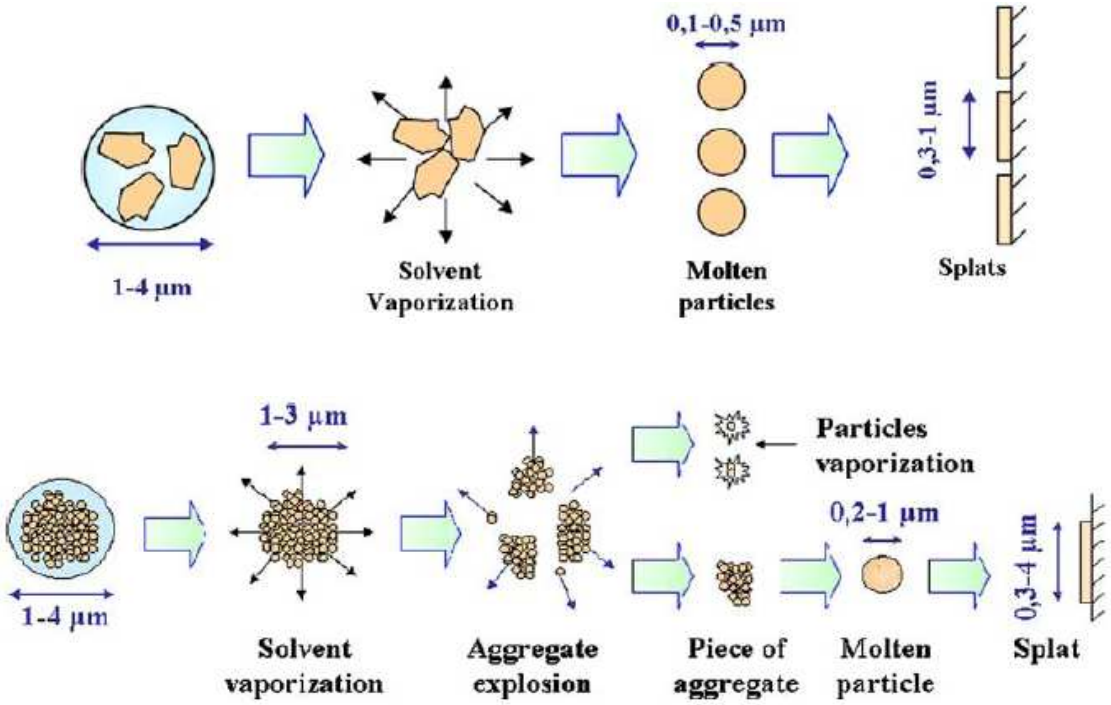

Fig. 2.1. Scheme of suspension droplet treatment: submicrometer particle size, from attrition milling (top) and nanometer particle size (bottom) [10].

2.2. SUSPENSION PREPARATION

Technology of suspension is a part of chemistry of colloids. Formulation of suspension is not only limited to mixing a liquid solvent with fine particles of sprayed material. These systems also contain additional components (such as dispersing and stabilizing agents), which minimize processes of agglomeration and sedimentation of fine particles and improve the rheological properties of the suspension. The stabilization of suspension is considered as an action of preventing the sedimentation and agglomeration of fine solids. The process can be controlled by the control of pH of the suspension or by adding a dispersant agent.

One way to obtain fine particles is milling of coarse powder. It's realized in the attrition milling device using cooling media (e.g. ethanol). The size distribution of milled particles depends on many parameters. If the time of milling is too long, fine particles start to agglomerate. Another important parameter is the energy of milling. Optimization of this parameter is realized by rotation velocity of the milling device and the balls' quantity and diameter, as well as by a mass ratio between the balls and the powder [8]. The last stage in the milling procedure is drying of the powder and sieving using calibrated sieves to prevent big particles to enter the suspension.

The solid phase is put in the liquid solvent, which is usually water, alcohol (ethanol, isopropanol) or their mixture. Physical parameters of the most often used solvents are presented in Table 2.1.

Table 2.1. Physical parameters of the solvents [3, 5].

Solvent	Evaporation temperature [K]	Evaporation enthalpy [kJ/g]	Reaction enthalpy [kJ/g]	Density at 20 °C [kg/m^3]
Water	373.0	2.26	–	998.2
Ethanol	351.3	0.84	29.7	789.3
Isopropanol	355.0	0.64	33.4	785.5

Depending on the kind of solvent, different interactions with the jet or flame take place. Water cools down the jet, whereas alcohol un the contrary, heats it up. On the other hand, the minimal velocity, which makes penetration into plasma jet possible, is lower in case of the water based suspension than the one for alcohol. The details are presented in Table 2.2. [5].

Table 2.2. Minimal velocities of different liquid streams make penetration possible into Ar + 25 vol.% H_2 plasma jet having temperature of 10000 K [5].

Velocity of plasma, m/s	Minimal velocity of water stream, m/s	Minimal velocity of ethanol stream, m/s
1000	1.71	3.42
2000	1.92	2.95

The dispersant is another component, which is added to the suspension. It is used to prevent the agglomeration of the particles and keeps the suspension well dispersed. It is surface active agent, which is absorbed on the particle surface and worked by electrostatic and steric repulsion [3].

One of the most important factors of suspension formulation is stability, which results in the particles, which do not agglomerate. The stability is characterized by zeta potential. The potential is defined as an electric potential difference between the particle surface and the liquid beyond the charge cloud of ions [11]. Around each particle there exists the double electrical layer, which consists of two parts. In the inner one, called Stern layer, the ions are strongly associated, whereas in the outer layer, called the diffuse layer, association of ions is not so strong. The potential on the board between the ambient and external layer is zeta potential. It is presented in Fig. 2.2.

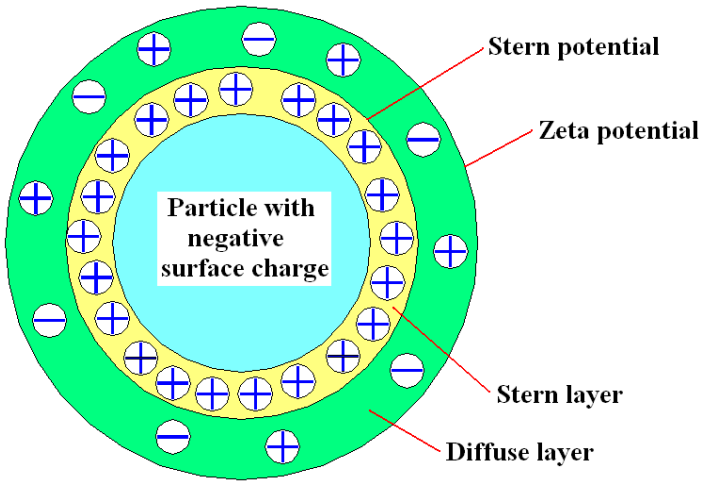

Fig. 2.2. Scheme of zeta potential phenomena occurring on particle surface.

If all particles in suspension have a large negative or positive zeta potential then they trend to repel each other and there is no tendency to agglomerate. However, if the particles have low values of zeta potential, there is no force to prevent the particles from coming together and agglomerating. The suspensions is stable if potential is outside the limits of +30

mV or -30 mV [12]. Stability of suspensions is the resultant of sum of attraction forces (Van der Waals) and the repulsion ones (electrostatic), which influence the particles moving in the suspension. It is schematically presented in Fig. 2.3.

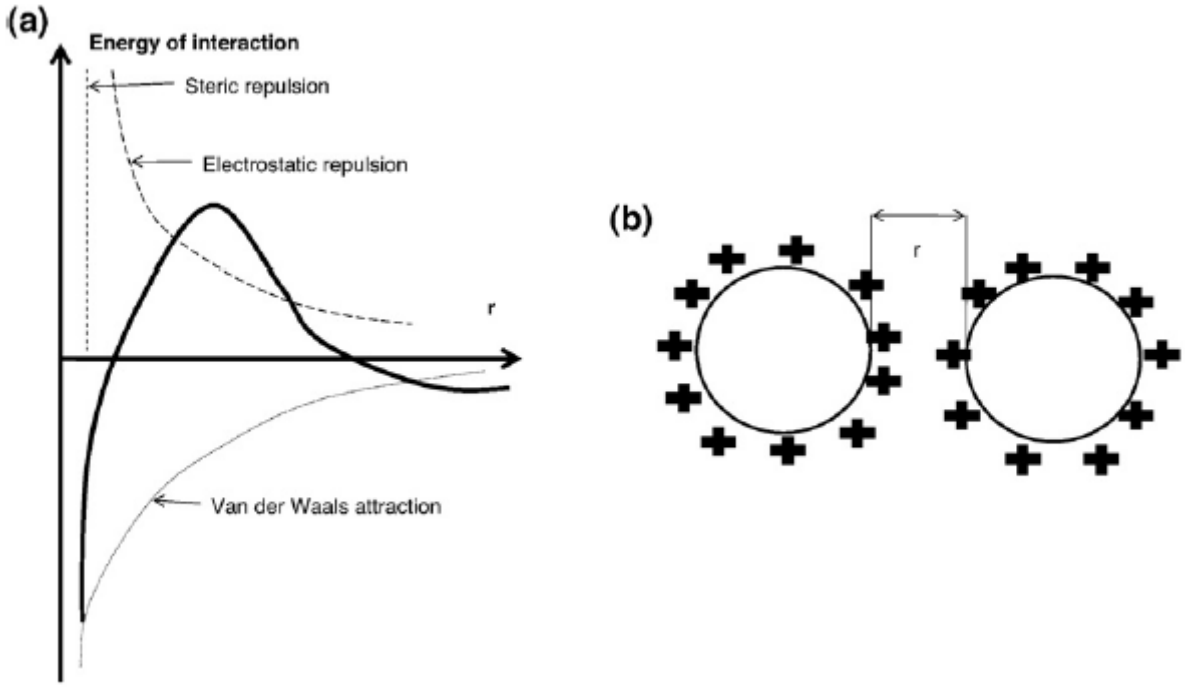

Fig. 2.3. Schematic representation of the interaction energy between two colloidal particles with the acting forces (a); charged particles — electrostatic stabilization (b) [8].

Zeta potential depends on pH, especially on isoelectric point (IEP), in which the suspension is the least stable, because the zeta potential value equals zero, as it is presented in Fig. 2.4. From the point of view of the suspension stabilization, IEP value should be lower or higher, than pH of the suspension. Another parameter, which could influence IEP is nonspecific ion adsorption. For some materials, e.g. $LiNO_3$, it can result in changing IEP value.

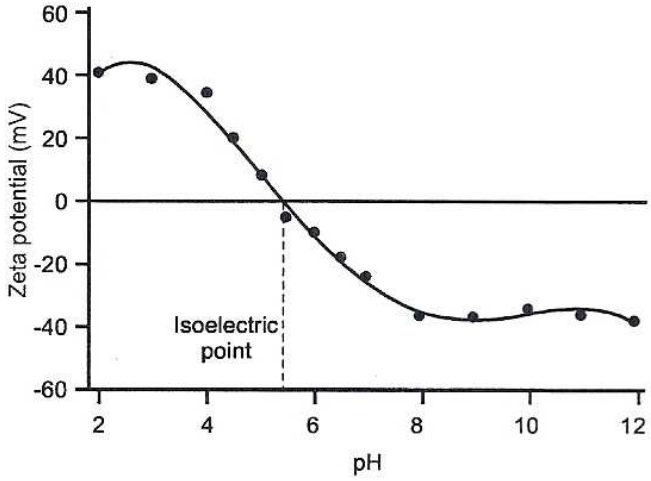

Fig. 2.4. Zeta potential vs pH of suspension [12].

A suspension is also characterized by viscosity. This parameter determines how easily suspension is pumped and transported through a pipeline. The viscosity of the stable suspension is lower than that of the unstable one and it increases with the fraction of solid phase, as it is shown in Fig. 2.5. The pumping is easier if viscosity is lower [8].

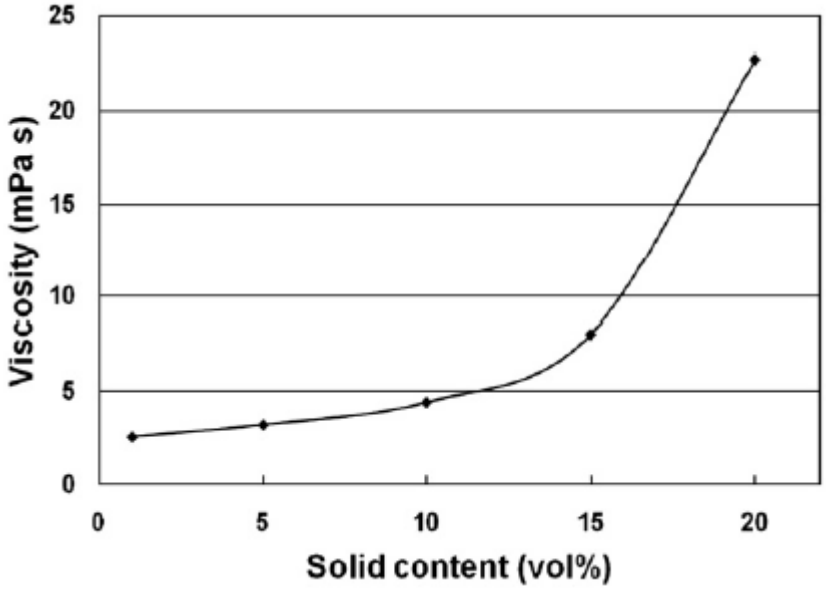

Fig. 2.5. Suspension viscosity in function of solid phase content [8].

The rheological property of the suspension is strongly influenced not only by the solid content, but also by the type of the powder (particle size and surface chemistry) and the type of the solvent and dispersant agent [13].

2.3. TRANSPORT AND INJECTION OF LIQUID INTO JETS

There are a few methods of transport suspensions into a jet. Feeding particles in a liquid solvent may be realized by a pneumatic system, peristaltic or perfusion pumps. The mode with a pressurized reservoir makes it possible to control the injection velocity by the pressure of compressed air. It is quite a simple and easy method. However peristaltic pumps require electronic control, but it enables to design and perform multilayer coatings (different suspensions), resulting in modification of coatings' chemical composition. The flow rate of the transported suspension in case of perfusion pumps is controlled by the rotation velocity of motor rollers [5]. These two systems of suspension transport are presented in Fig. 2.6.

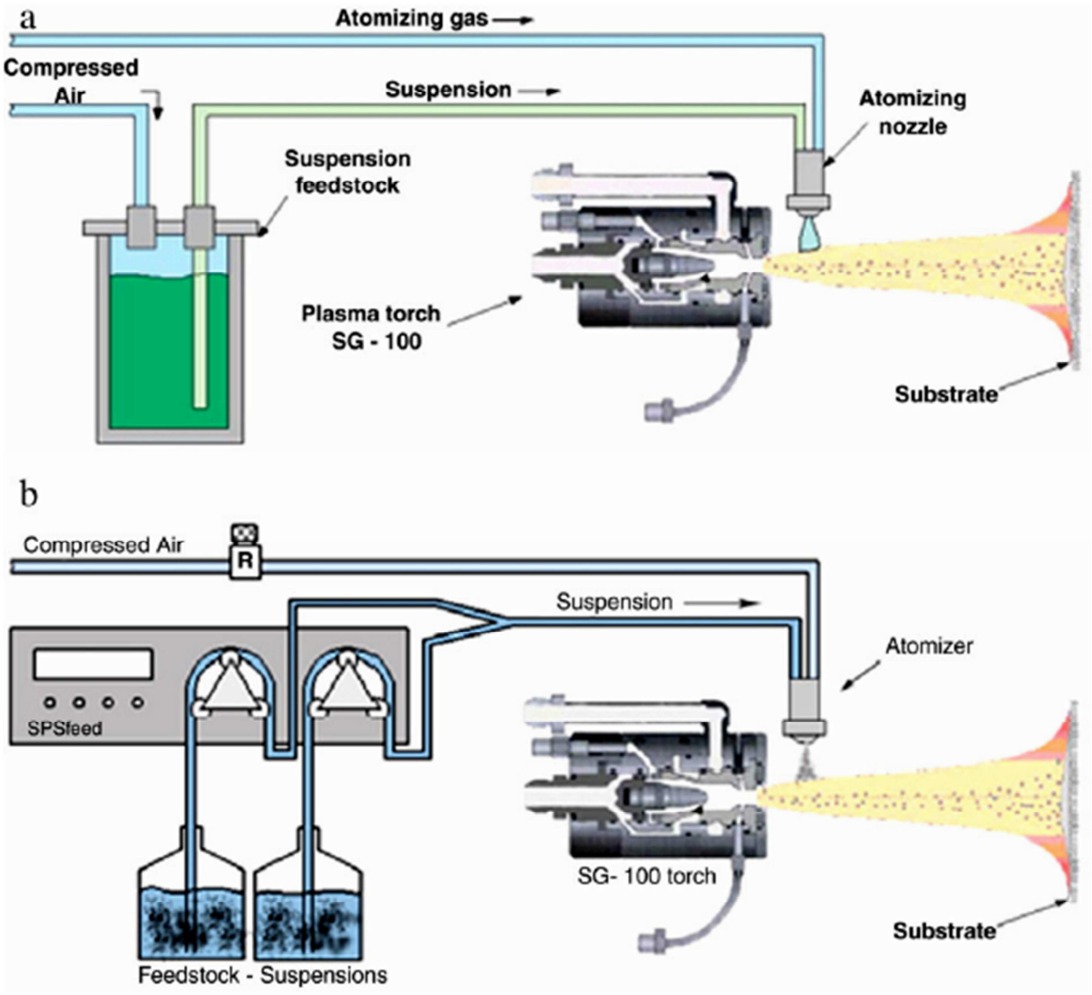

Fig. 2.6. System of liquid delivery applicable in thermal spraying:
(a) pressurized vessel, (b) peristaltic pumps [14].

Independently of the transport mode, suspension injection can be achieved in two ways: (i) with a continuous stream nozzle or (ii) with an atomization system, which are presented in Fig. 2.7.

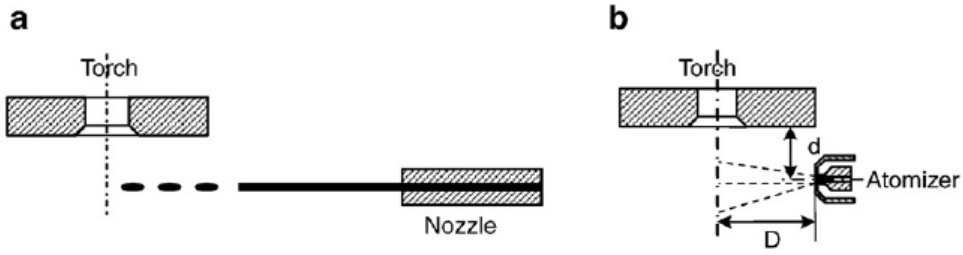

Fig. 2.7. Injection systems: (a) nozzle, (b) atomizer [5].

The liquid jet coming from a pipeline keeps initially its cylindrical structure. Then, the jet starts to break up under the action of external forces such as gravitation, resistance of surrounding air, etc. The disruption of the jet depends on the geometry of liquid, velocity of

liquid relative to that of the surrounding medium and on the liquid properties such as density, viscosity and surface tension [8].

Atomization needs an external energy to break up the liquid bulk. The energy can result from centrifugal forces, external pressure, kinetic energy or another fluid, acoustic energy, etc. Consequently the atomizers can be categorized as [8]:

- rotary atomizers using centrifugal forces;
- pressure atomizers including centrifugal pressure nozzle;
- pneumatic nozzle including “two fluids” nozzles;
- sonic nozzle basing on acoustic energy.

The way of injecting has a great influence on how liquid can penetrate plasma jet or flame, as a jet or as the droplets. The important condition of successful coating deposition is the penetration of the liquid in the hot temperature zone. It is very important in case of using radial injection, which is common for most of the commercial torches. The dynamic pressure of the suspension liquid must be greater than that of the plasma jet one to ensure particle penetration into the central zone of the jet or flame, which is shown by the following relationship:

$$\frac{\rho_l \cdot v_l^2}{2} > \frac{\rho_p \cdot v_p^2}{2} \qquad (2.1)$$

where:

ρ_1 – liquid density [kg/m^3]

v_1 – liquid velocity [m/s]

ρ_2 – plasma density [kg/m^3]

v_2 – plasma velocity [m/s]

2.4. PHENOMENA AT SUSPENSION THERMAL SPRAYING

Injected droplets of the suspension into the plasma jet are accelerated. Evaporation of liquid phase takes place at the same time and only solids remain. These particles are in contact with hot gases and as a result are heated and molten. However, morphology of suspension sprayed coatings depends on the way of the suspension injection into the plasma jet. In case of the external atomizing injector coatings were quite homogeneous with finely grained microstructure in the cauliflower-like form. In turn coatings sprayed with the internal continuous-stream injector exhibited a bimodal microstructure, which contains *dense zone*,

which is large, molten lamellae and the *sintered zone*, which is molten and solidified spherical particles [8]. Different microstructures could depend on the phenomena occurring in the suspension thermal spraying, presented in Fig. 2.8.

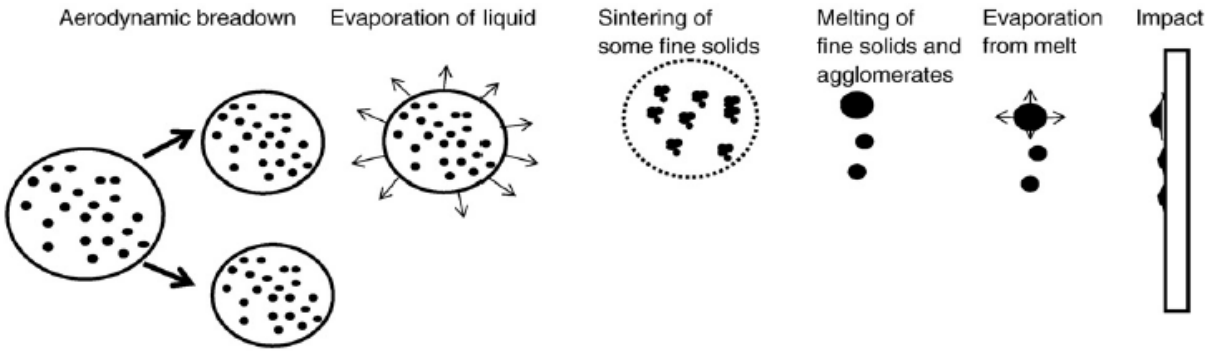

Fig. 2.8. Evolution of a suspension droplet in the high temperature plasma or flame [8].

The large droplets injected or formed from the liquid jet by atomization are submitted into high velocity plasma jet. The drag force between the droplet and the plasma creates shear deformation of the droplet. It can lead to the atomization of large droplets into smaller one, depending upon droplet size and surface tension. This effect is called *aerodynamic breakup*. It occurs shortly after the injection of large droplet in time of microseconds. The next stage is rapidly decreasing of the droplet's diameter, which is the result of the liquid suspension evaporation. The evaporation is caused by the difference of the moisture content. After the evaporation of liquid, the sintering process of fine particles can start. The driving force of the solid state sintering is the decrease in the surface area and lowering of the surface free energy by the elimination of solid-vapour interfaces. The agglomeration of the liquid fine particles is nearly instantaneous. Melting of the fine solids and evaporation from their surface are typical phenomena for thermal spraying [8].

2.5. APPLICATION OF SUSPENSION PLASMA SPRAYED COATINGS

The possible applications of the coatings sprayed with suspension result from their unique properties, which are based on fine structure. This takes effect in denser and less

porous coatings [8]. The range of emerging applications is very wide, from aircraft industry up to medicine and electronic. Details will be given below.

2.5.1. THERMAL BARRIER COATINGS

Thermal barrier coatings, TBC have been tested extensively because of their ability to reduce the temperature profiles in gas turbines. Due to the low thermal conductivity, ceramic top coating decreases the temperature of combustion gases to the level acceptable for metallic components of the turbine. It is presented schematically in Fig. 2.9. Typical material used for TBC is 8 wt.% yttria stabilized zirconia. However ceria stabilized zirconia and compounds based on lanthanum are intensively tested as an alternative materials for TBCs [15].

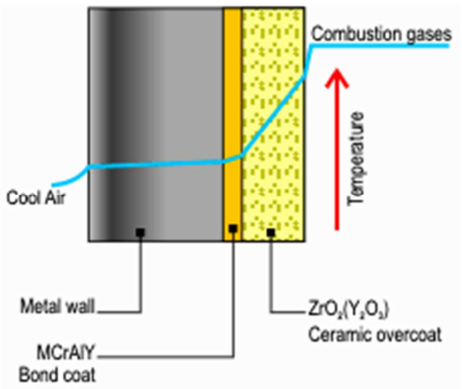

Fig. 2.9. Scheme of the structure of a two layer thermal barrier coating
on a turbine blade surface together with a temperature profile [16].

2.5.2. PHOTOCATALYTIC SURFACES

The degradation and destruction of organic pollutants (Fig. 2.10) are an important issues in the chemical industry. Titanium dioxide, TiO_2 is the most investigated material for this application, because it is excellent photocatalyst [1].

The SPS technique makes it possible to obtain titania coatings, which exhibit at least good photocatalytic properties, even with small content of the anatase phase. It is connected with its fine structure and high value of the specific surface area. On the other hand, with the SPS process it is possible to produce titania coatings, which are rich in anatase phase, e.g. [17].

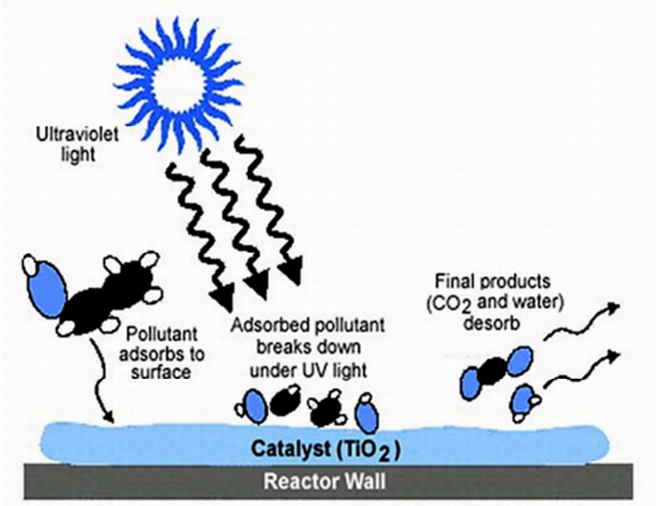

Fig. 2.10. Scheme of pollutant degradation on the surface with TiO_2 coating [18].

2.5.3. ENERGY

Solid oxide fuel cells, SOFC, are very efficient energy conversion systems even for rather small units in the kW range [19].They convert chemical energy into electrical one at high temperature [8]. Scheme of SOFC is presented in Fig. 2.11.

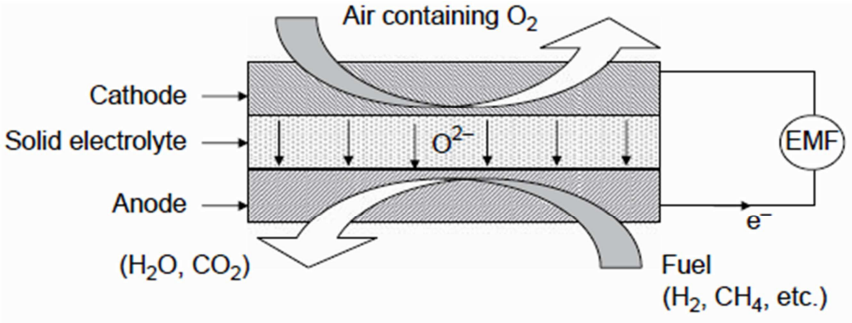

Fig. 2.11. Principles of a solid-oxide fuel cell [1].

The SPS method can be used to produce three elements of SOFC. It could be an electrolyte, where the material is yttria stabilized zirconia, YSZ tested e.g. by Wang *et al*. [20], Brousse *et al*. [21] and Waldbilig and Kasler [22]. Both electrodes in SOFC could be also manufactured with the same technique. In case of the anode, the composition of NiO with YSZ is mainly used, e.g. Marchand *et al*. [23]. On the other hand, for the cathode rare earth elements are used, mostly based on lanthanum, e.g. LSM ($(La_{0.65}Sr_{0.3})MnO_3$) used by Kassner *et al*. [24]. The SPS deposition technique of these components makes it possible to produce coatings, in which high porosity level is combined with fine pore size, presented in Fig. 2.12. Such microstructures are advantageous for a good electrochemical performance.

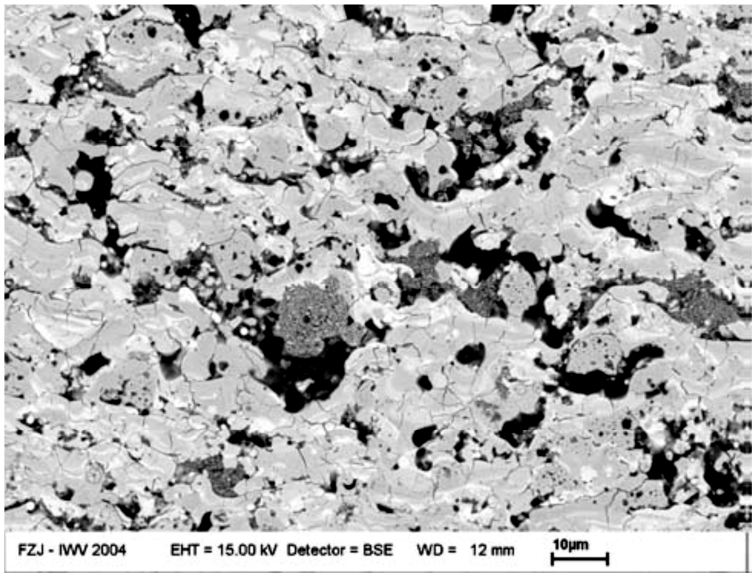

Fig. 2.12. Microstructure of a LSM cathode layer produced by SPS [25].

In the field of energy the SPS deposition technique is used to produce layers in another type of cells, such as photovoltaic ones. One of example is TiO_2 layer in Graetzel cells [26], where SPS method helps to obtain high surface area with a very fine grain structure.

2.5.4. BIOACTIVE COATINGS

Medical applications of suspension plasma sprayed coatings are mainly connected with hydroxyapatite, HA, which is coated on the surface of prosthesis or implants (Fig. 2.13). They apply them because chemical composition and crystal structure of HA is similar to a human bone. With SPS technique it is possible to obtain thinner coatings, in range 10 to 50 µm, than with conventional thermal spraying, e.g. APS. Of course it is connected with reduction of prosthesis production costs [13].

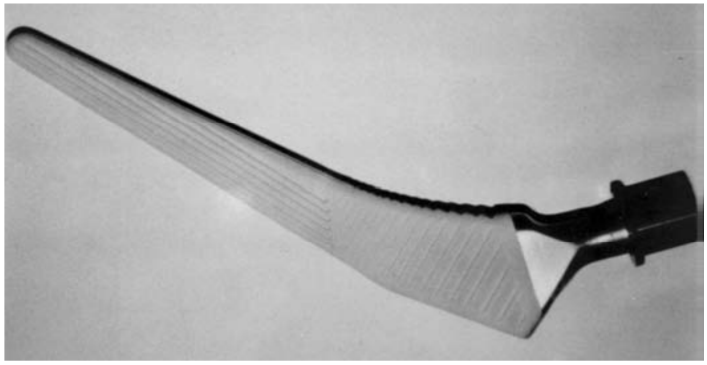

Fig. 2.13. A femoral stem of a hip prosthesis with a part coated with bioactive hydroxyapatite ceramics [1].

2.5.5. WEAR-RESISTANCE COATIGNS

There is a wide range of materials for wear-resistance coatings e.g. tungsten carbide-cobalt, WC-Co, alumina, Al_2O_3, alumina-zirconia Al_2O_3-ZrO_2, etc. In literature there are many research publications dealing with wear-resistance coatings produced with suspension plasma spraying. The SPS technique is a promising candidate for manufacturing of wear-resistance coatings, because of improved tribological behavior. The microhardness is higher than in the conventional deposition process (Fig. 2.14), moreover porosity is reduced.

These phenomena result from the fine structure of the coatings. The coatings manufactured with SPS methods exhibit a dense structure and the layers are more cohesive [27]. It results in significantly lower coating wear rate than that produced with conventional spraying, which is presented in Fig. 2.15.

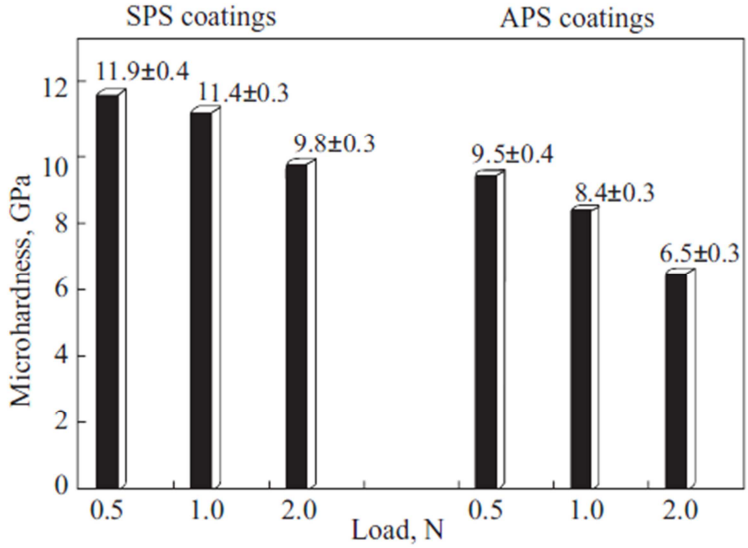

Fig. 2.14. Microhardness of SPS and APS coatings under different load [28].

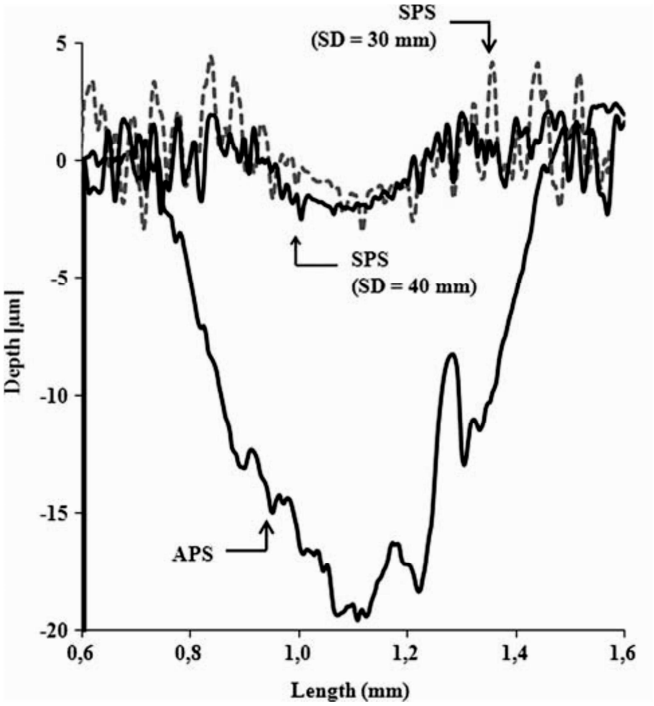

Fig. 2.15. Wear profiles for Al_2O_3 coatings, microstructure produced by APS and submicrometer produced by SPS, details in original paper [29].

2.5.6. ELECTRON EMITTERS

Titania coatings have been intensively studied because of their interesting electrical properties. The idea of using the suspension plasma spraying technique to obtain these coatings results from two factors, which promote electron emission [5]:

- enhancement of the local electric field on small (nano- and/or submicrometer) grains on the emitting surface;
- presence of small conducting grains (Magneli phases) embedded into the dielectric matrix (rutile and/or anatase), presented in Fig. 2.16.

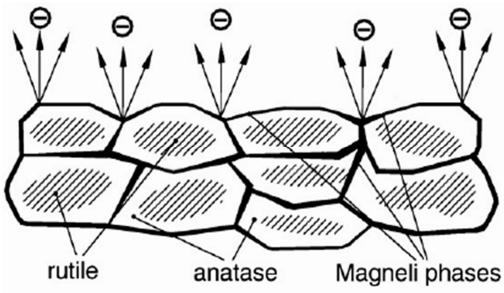

Fig. 2.16. Scheme of emission from suspension plasma spayed TiO_2 coating [5].

The presence of the fine grains is the main advantage of SPS methods, with which titania coatings were obtained. The emission current depends on the applied voltage and increases with time of emission [5], which is presented in Fig. 2.17.

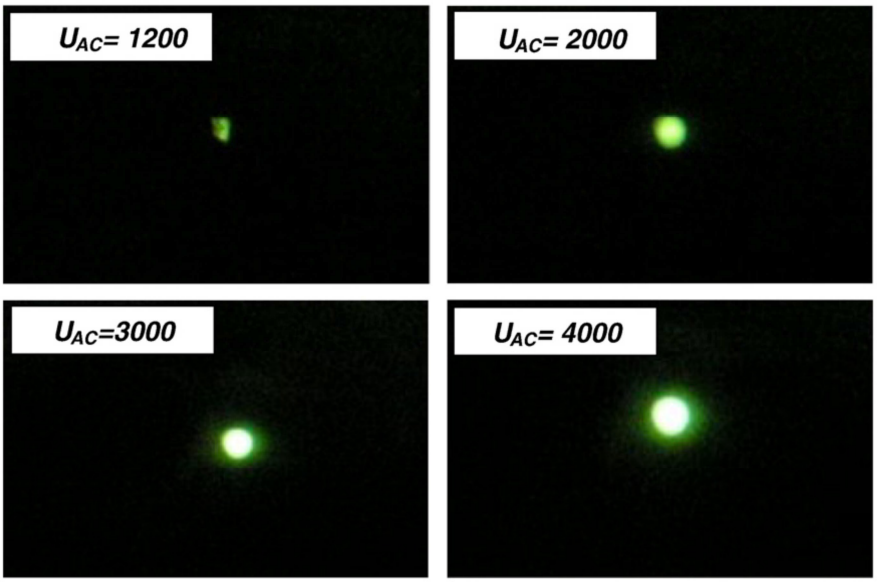

Fig. 2.17. Light emitted by a prototype emitter produced with a suspension plasma sprayed TiO_2 under increasing voltage between anode and cathode, U_{AC} [8].

2.6. SUMMARY

The scientific interest in nanostructured or finely structured coatings is still increasing. The interest results from the material properties modifications caused by nanosized crystal grains. These coatings are easy to manufacture using methods of gas condensation, such as CVD, PE-CVD, PVD, EB-PVD etc. The coatings obtained with these techniques are generally thin and their thickness can hardly be higher than a few micrometers. On the contrary, SPS or SPPS techniques make it possible to produce finely structured coatings in range of thickness from a few micrometers up to a few hundred of micrometers and moreover, coatings exhibit unique properties, in comparison to the conventional ones [6]. On the other hand, the thickness of conventional thermal spraying techniques is limited to about 50 μm, because of the use of coarse powders, which have big grains [13]. The methods of thermal spraying from liquids can be a better way to obtain dense or controlled porosity coatings than conventional thermal spraying. However, SPS and SPPS are more complex than conventional methods of the manufactured coatings because of phenomena such us fragmentation and vaporization of the liquid etc. [6]. Moreover, new industrial standards for SPS and SPPS methods have to be defined, which should concern the storage of ultrafine powders, suspension or solution preparation and feeding of material [13].

CHAPTER 3

INSTRUMENTED INDENTATION TESTS

3.1. INTRODUCTION

Coatings obtained in thermal spraying processes can be tested with different methods to determine their mechanical properties, such hardness, bulk modulus, etc. The indentation test is the most popular and useful technique. This method is based on material penetration by, most often, a diamond indenter under given indentation load. The indenters have different geometry, like pyramidal, spherical or conical ones, which is effective in variations in elastoplastic deformation of the material below the indenter. Different shapes of the indenter are mostly connected with determination of different mechanical properties, e.g. hardness, bulk modulus and cracking resistance are determined with pyramidal indenters, whereas spherical ones are used to determine tensile properties and bulk modulus. Depending on the range of indentation test, a different scale of loads should be chosen, nano- (loads lower than 1 gram), micro- or macro- (loads higher than 1 kilogram) ones [30]. These scales are relative to the research area of mechanical properties, local, for nano- and microindentation or global, for macroindentation. There are two main methods of analyzing the carried out indentation test to determine mechanical properties. One of them is usual indentation, which is based on the measurement of the geometrical dimensions of the residual indenter. In the other one, called instrumented indentation tests, the mechanical properties are determined from the analysis of a load-depth curve.

3.2. HARDNESS

The hardness number is commonly used to represent the resistance of a material to plastic deformation, usually by indentation [30]. The general formula in hardness calculation is as follows:

$$H = \frac{P}{A} \qquad (3.1)$$

where:

H – the hardness number, [MPa]

P – the applied load, [N]

A – representative area of the residual indent, [mm^2]

From a general point of view, different types of indenters can be used to characterize the mechanical properties by indentation, i.e. spherical or sharp indenters, as mentioned in the introduction. Among the last category, the most often employed indenters are Vickers (square based pyramid), Knoop (lozenge base pyramid) and Berkovich (triangular base pyramid). In consequence, the representative area, *A*, depends on the shape of the indenter. Moreover, it is also possible to consider the true contact area between the indenter and the material or the projected one in the plan of the surface of the material. As an example for Vickers and Knoop indenters, the hardness number calculation can take different forms listed in Table 3.1.

Table 3.1 Different hardness number calculations depending on true of projected area for two kinds of indentation, Vickers and Knoop [30].

	True contact area	Projected contact area
Vickers indenter	$HV = 1.8544\frac{P}{d^2}$	$Hm = 2\frac{P}{d^2}$
Knoop indenter	$HK_T = 12.873\frac{P}{L^2}$	$HK_P = 14.229\frac{P}{L^2}$

In Table 3.1, *d* represents the diagonal of the Vickers residual indent and *L* the large diagonal of the Knoop indent.

It is noticeable that in literature a direct comparison between the two hardness numbers is done. But it is not possible since the Vickers hardness considers the true contact area whereas the Knoop hardness takes into account the projected one.

In case of instrumented indentation tests (IIT), the hardness number is calculated from different parameters, which result from the analysis of a load-depth curve, this original method being proposed by Olivier and Pharr [31]. Depending which indentation depth is taken, the hardness calculation can have different forms. All possibilities are collected in Table 3.2. The symbols used to represent the different indentation depths in Table 3.2. are presented are in Fig. 3.1 which shows various indentation depths in a schematic representation of a section through an indentation [3.1].

Table 3.2 Different hardness number calculations, depending on different indentation depth definition, considering true or projected area [30].

	Indentation depth		
	Maximum	Residual	Contact
True contact area	$HM=\frac{P}{26.43\cdot h_m^2}$	$H=\frac{P}{26.43\cdot h_r^2}$	$H=\frac{P}{26.43\cdot h_c^2}$
Projected contact area	$H=\frac{P}{24.5\cdot h_m^2}$	$H=\frac{P}{24.5\cdot h_r^2}$	$HIT=\frac{P}{24.5\cdot h_c^2}$

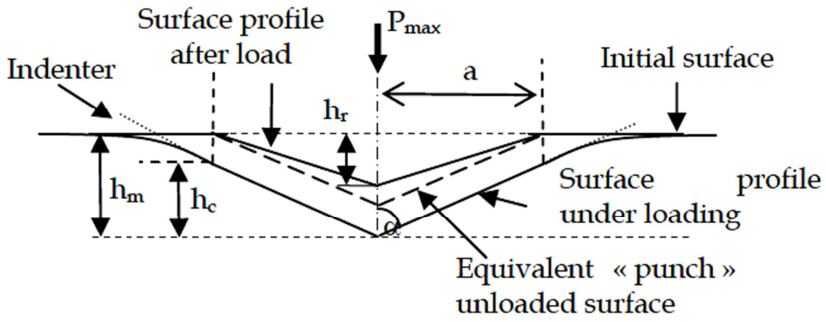

Fig. 3.1. Schematic cross-section of a conical indent; h_m – maximum indentation depth, h_r – residual indentation depth, h_c – contact indentation depth [30].

As indicated in Fig. 3.1, different indentation depths can be defined. The maximum indentation depth, noted h_m, is the distance reached by the indenter under the maximum applied load. The residual indentation depth, h_r, is the residual depth which is obtained after the withdrawal of the indenter. Oliver and Pharr [31] defined a contact indentation depth, h_c, Between these two distances which corresponds to the depth where the tested material is always in contact with the indenter under the application of the maximum load. If two others distances can be well-determined, it is not the case for h_c. That is why the authors have defined a procedure from the analysis of the unloading part of the load-depth curve (Fig. 3.2).

In Fig. 3.2. typical load-depth curve is presented. It is the result, which is obtained after a single indentation test. Then, using the Olivier and Pharr methodology [31], the presented curve is analyzed. All symbols in Fig. 3.2 are correspond to the ones presented in Fig. 3.1 and Table 3.2.

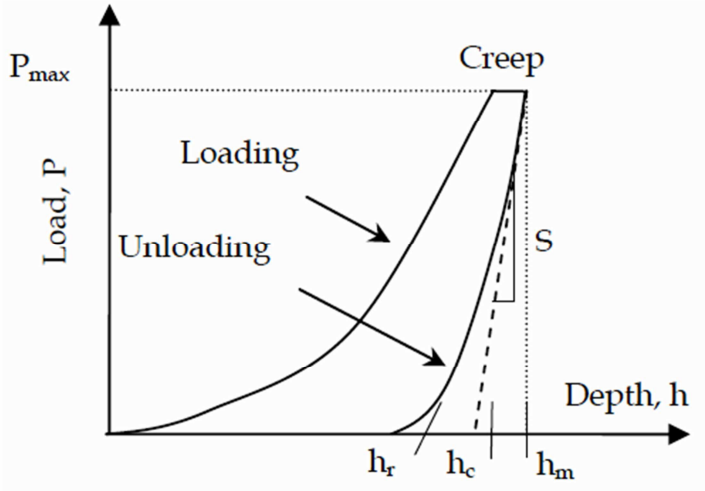

Fig. 3.2. Typical load-depth curve, obtained in indentation tests [30].

The contact distance is calculated with the following relation:

—

where:

P_{max} is the maximum applied load, ε is the parameter equal to 0.75 for sharp indenter and 1 for spherical indenter and S is the slope of the unloading part of the load-depth curve as shown in Fig. 3.2.

As it can be seen in this figure, the unloading curve cannot be adequately represented by a straight line. That is why Oliver and Pharr suggest fitting the unloading curve using a simple power law between 40 and 98% of the maximum applied load:

where B, h_f and m are the fitting parameters.

In a consequence, S is derived from eq. (3.3) with:

—

It is clear that according to the definition of the indentation depth and the consideration of the projected or true contact area, the hardness calculation can differ in a great extent. For simplicity, Table 3.2 shows the different possibilities to calculate a hardness number. Note that usually, two kinds of hardness number are calculated: the Martens hardness, *HM*, considering the true contact area calculated with the maximum indentation depth and the contact hardness, *HIT*, calculated from the projected contact area using the contact depth. It is clear that these two hardness numbers are not comparable since the area in

HIT is always lower than the area in *HM*. On the other hand, the Martens hardness is interesting to study since its value is directly comparable to the Vickers hardness. Indeed, from a simple geometrical consideration of the shape of the Vickers indenter, it can be deduced that the diagonal to the depth ratio is equal to 2 tan 74°, close to 7 where 74° is the half angle measured between two opposite edges of the pyramid at the top of the indenter. Finally, we can observe that the most often use hardness numbers are Martens hardness, *HM*, in microindentation and contact hardness, *HIT*, in nanoindentation. Moreover, *HM* is equivalent to HV, when is considering the diagonal to the depth ratio of Vickers indenter.

3.3. INDENTATION SIZE EFFECT

When analyzing the indentation test to determine hardness of the material, some variations of the hardness number as a function of the applied load can be observed. This phenomenon represents the hardness-load dependence and it is called indentation size effect (ISE). It is relative to many parameters and factors, like geometry of the indenter, roughness, work hardening, pilling-up, sinking-in, surface energy, different composition and crystal anisotropy [32]. There are two main streams to characterize ISE. One of them, based on polynomial laws, expresses applied load, *P*, as the function of the indent diagonal, *d*. On the other hand, the other group of equations is based on strain gradient plasticity theory [33], in which hardness, *H*, is expressed as a function of indentation depth, *h*.

Before analyzing the Indentation Size Effect, it must be noted that ISE strongly depends on the scale of hardness measurement. Indeed, it has been noted by Bückle [34] that the hardness number has a constant value in macroindentation. Usually in microindentation, the hardness number increases when the load decreases and the tendency is mandatory in nanoindentation but other problems such as roughness, indenter tip defect, polishing effect are enhanced the scale of measurement. In general there are two approaches to ISE characterization. One is purely descriptive and is based on the mathematical relations between the applied load and the indent diagonal. Note that these relations are also applicable when considering the indentation depth. Among the most useful ones are the relation of Meyer [35] which connects the load to the diagonal by the power law where the exponent can be linked to a strain-hardening factor. More recently, the Proportional Specimen Resistance (PSR) model proposed by Li and Bradt [36] is probably the most commonly employed in this group of

relations. The applied load is expressed as a polynomial of degree 2 as a function of the indent diagonal:

$$P = A_1 \cdot d + A_2 \cdot d^2 \tag{3.5}$$

According to the hardness definition in Table 3.1, the PSR model makes it possible to represent the hardness number by introducing the macrohardness (being the hardness which will be obtained by the application of an infinite load) and the parameter representing the ISE called K_{ISE}.

$$H = H_0 + \frac{K_{ISE}}{d} \tag{3.6}$$

The other approach has been suggested by Nix and Gao [33]. This model is based on the Strain Gradient Plasticity (SGP) theory. The main interest of such a model is that the parameter used to characterize the hardness can be linked to intrinsic properties. Here, the hardness , *H*, is expressed as a function of the inverse of the indentation depth.

$$\left(\frac{H}{H_0}\right)^2 = 1 + \left(\frac{h^*}{h}\right) \tag{3.7}$$

where:

H – hardness for a given depth of indentation, *h*

H_0 – macrohardness

*h** – characteristic scale-length, which represent the hardness-load dependence.

The above model uses the concept of geometrically necessary dislocations (GND), which is based on Taylor's dislocation theory. Strain gradient plasticity theory assumes for simplicity that the indentation deformation process is accommodated by GND, which is required to account for the permanent shape change at the surface. Fig. 3.3 schematically represents the model of Nix and Gao. It can be seen, that GND are homogenously distributed below the indent in a semi-hemispheric region for which the size is equivalent to that of the indent [37].

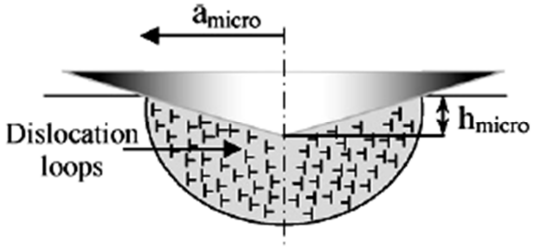

Fig. 3.3. Microindentation range of geometrically necessary dislocations created by a rigid conical indentation where the dislocation structure is idealized as circular dislocation loops [37].

After above-mentioned simplifications it is possible to express macrohardness, H_0 and characteristic scale-length, h^*, in the following relations:

$$H_0 = \frac{3\sqrt{3}}{2} \cdot \mu \cdot b \cdot \sqrt{\rho_s} \qquad (3.8)$$

$$h^* = \frac{81}{8} \cdot \frac{1}{f^3} \cdot b \cdot \tan^2\theta \cdot \left(\frac{\mu}{H_0}\right)^2 \qquad (3.9)$$

where:

μ – shear modulus

b – Burger's vector

ρ_s – density of statistically stored dislocations

θ – angle between the surface of the conical indenter and the plane of the surface, its value is equal to 19.3°

f – corrective factor

With the parameter f it is possible to take into account the GND effect on the size of the plastic zone. It was introduced by Durst et al. [38]. In microindentation range it is equal to 1.

Because of the problems to determine dislocation density before the indentation test and with implicit function, which characterizes h^* parameter, another approach was presented by Chicot [37]. In this work, a different scale-length parameter was proposed, H_{LSF}, which is proportional to an indentation toughness thus it can represent the ability of the material to be plastically deformed by indentation. Based on Nix and Gao model [33] a new parameter, called hardness length-scale factor was introduced, as follows:

$$H^2 = H_0^2 + \frac{H_{LSF}^2}{h} \quad \text{where} \quad H_{LSF} = H_0 \cdot \sqrt{h^*} \qquad (3.10)$$

This parameter is expressed as an indentation toughness in MPa·m$^{1/2}$ [30], and it can be expressed as a function of the shear modulus and the Burger's vector by using the equation (3.9). Finally:

$$H_{LSF} = \alpha \cdot \mu \cdot \sqrt{b} \qquad (3.11)$$

is obtained, where $\alpha = \left(\frac{81}{8} \cdot \frac{1}{f^3} \cdot tan^2\theta\right)^{1/2}$ is a constant. θ is equal to 19.3° and the factor f only depends on the size of the indentation experiment, i.e. it is equal to 1 in microindentation and 1.44 in nanoindentation.

From the general point of view when analyzing hardness variation, it is always necessary to take into account the indentation size effect (ISE) which represents the hardness-load dependence. Hardness length-scale factor, H_{LSF} [37] can represent the ability of the material to deform itself under the indentation. In any case, for well-characterized the hardness behavior of a material it is necessary to provide the macrohardness and a term to represent the ISE.

3.4. CONTINUOUS MEASUREMENT HARDNESS

In the typical load-depth curve, presented in Fig. 3.2, its loading part can be described by a parabolic relation between applied load, *P* with indentation depth, *h*, which is as follows:

$$P = C_1 \cdot h^2 \qquad (3.12)$$

where:

C_1 – constant, depending on the geometry of the indenter tip and the material properties. This constant can take different forms, which depend on mechanical behavior of the material. It can be e.g. the function of the elastic properties or yielding stress [30]. In spite of validation of eq. 3.12, in numerous results, e.g. [39, 40], some deviations from above-mentioned formula in comparable with experimental curves could be seen [30]. As a result, another model, more general, was suggested, originally based on Meyer law [35]

$$P = C_2 \cdot h^n \qquad (3.13)$$

where:

C_2 – constant, depending on material

n – exponent, which was generally found to be less than 2.

Another model was proposed by Zeng and Chiu [41]. The original approach of authors considers the influence of tip's defects on the discrepancies between the experimental data and the applied models. They suggested divide loading part of the load-depth curve into two parts, in order to obtain better fit. The first one, in range of initial 20-50 data points, should be fitted with following formula:

$$P = C_3 \cdot h^{3/2} \qquad (3.14)$$

where:

C_3 – constant, which could be estimated from fitting of experimental data. In this part, the authors consider the rounded tip effect on the penetration depth and they compare the sharp indentation to a spherical indentation.

Then the other part of the loading curve should be fitted with expression 3.12 if a shift in load is introduced as follows:

$$P = P_0 + C_4 \cdot h^2 \qquad (3.15)$$

where:

P_0 – initial deviation in the applied load

C_4 – constant, which is estimated with P_0 from fitting of experimental data of this part of curve.

Moreover, this deviation, which is represented by the parameter P_0, probably comes from the initial contact load definition at the surface. The additional problem is indenter tip imperfection, which could influence P_0 value. In case of microindentation eq. 3.14 can be applied for the entire loading part of load-depth curve since the rounded tip effect of the indenter can be neglected [30].

The initial contact load, called zero contact, may contain some deviations. To prevent the former deviations, the constant load, P_0 was added into the formula, which defines Martens hardness. This new formula is called continuous measurement hardness and is as follows:

$$HM = \frac{(P - P_0)}{26.43 \cdot h^2} \qquad (3.16)$$

Eq. 3.16 can be slightly different, when it is explained with eq. 3.15. The continuous Martens hardness is then the following:

$$HM = \frac{C_4}{26.43} \qquad (3.17)$$

As it can be seen, in eq. 3.17 the constant value, C_4 was introduced to relate it to the hardness. Consequently, hardness number becomes a constant [30]. As previously mentioned, it is always necessary to take into account the indentation size effect (ISE), which represents the hardness-load dependence. For this reason, in model Chicot *et al.* [42] Martens hardness is expressed as a function of parameter H_{LSF}, eq. 3.10 and put it into eq. 3.17. These combinations were then introduced to eq. 3.15 and loading part of the load-depth curve is a function of applied load in indentation depth, as follows:

$$P = P_0 + 26.43 \cdot \left(HM_0^2 + \frac{H_{LSF}^2}{h} \right)^{1/2} \cdot h^2 \qquad (3.18)$$

This model involves three constants: (i) the deviation load, P_0, which considers the rounded tip effect and the zero shifts, (ii) the continuous measurement hardness, HM_0, of the tested material and (iii) the hardness length-scale factor, H_{LSF}, which represents ISE of the material [30], [52].

3.5. BULK MODULUS

Indentation tests make it possible to determine bulk modulus instead of the Young modulus. It can be estimated using Knoop indenter, called Marshall's method [43] or from load-depth curve analyzing, according to the methodology proposed by Oliver and Pharr [31]. Nix and Gao [33] proposed bulk modulus determination from the inversed slope of the linear part unloading curve of the load-depth curve, obtained in the indentation tests, as it is presented in Fig. 3.2. The main relation, from which elastic properties of tested material are calculated, bases on the equation proposed by Doerner and Nix [44] and it is as follows:

$$\frac{1}{S} = \left(\frac{dh}{dP}\right) = C_T = C_f + \frac{\sqrt{\pi}}{2} \cdot \frac{1}{\beta \cdot \gamma \cdot E_R \cdot \sqrt{A_C}} \qquad (3.19)$$

where:

S – slope of linear part unloading curve; it's reverse of total compliance, C_T

C_f – frame compliance

A_C – projected contact area

E_R – reduced modulus

β, γ – corrective factors

Most of the time, researchers calibrate their system by performing indentations on fused silicate to calculate the frame compliance C_f which is subsequently introduced as a constant into the numerical analysis of the data. However, this approach is not entirely correct, since Chicot *et al.* [45] has shown that this parameter is not a constant for a given apparatus, but depends on the nature, size, and shape, mounting and testing conditions of the sample [45]. It is a very important remark, because C_f is used to correct the value of the obtained depth, as follows:

$$h = h_{meas} - C_f \cdot P \qquad (3.20)$$

where:

h_{meas} – measured indentation depth

h – corrected indentation depth

Correction factors, β and γ, were intensively discussed. Parameter β is connected with indenter geometry. The earliest value was proposed by King and it was 1.012 [46]. On the other hand, Dao *et al.* suggested the value of 1.07 in their model [47]. A different approach was proposed by Antunes *et al.* They used three dimensional model of Vickers indenter in

simulations. As a result, the obtained value of β factor was 1.05 [48]. The parameter γ was added by Hay *et al.*, as a solution for the overestimated values of the obtained elastic modulus using Sneddon's model. Authors proposed this factor, which depends on indenter shape [49].

Finally, by considering the correction factors, β and γ, introduced by Antunes *et al*. [48] and Hay *et al*. [49], respectively, Chicot *et al*. [50] have proposed the following expressions:

$$\left(\frac{dh}{dP}\right)_{h=h_m} = C_f + \sqrt{\frac{\pi}{24.5}} \cdot \frac{1}{2 \cdot (\beta \cdot \gamma) \cdot E_R} \cdot \frac{1}{h_c} \qquad (3.21)$$

$$E_R = \left(\frac{1-\nu_m^2}{E_m} + \frac{1-\nu_i^2}{E_i}\right)^{-1} \qquad (\mathbf{3.22})$$

where, E_m, E_i, ν_m and ν_i represent the elastic modulus and the Poisson's ratio of the material and the indenter, respectively. For the diamond indenter, the elastic modulus is equal to 1140 GPa and the Poisson's ratio to 0.07 [51].

In case of Vickers indenter, the correction factor γ solely depends on Poisson's ratio value of tested material:

$$\gamma = \pi \cdot \frac{\frac{\pi}{4} + 0.1548 \cdot \cot\lambda \cdot (1-2\nu) \cdot [4 \cdot (1-\nu)]^{-1}}{\left(\frac{\pi}{2} - 0.8312 \cdot \cot\lambda \cdot (1-2\nu) \cdot [4 \cdot (1-\nu)]^{-1}\right)^2} \qquad (3.23)$$

When Poisson's ratio, ν, is equal to 0.3, e.g. for stainless steel, then γ factor is equal to 1.07. A typical plot, from which frame compliance, C_f and bulk modulus of material, E_m are determined, is presented in Fig. 3.4.

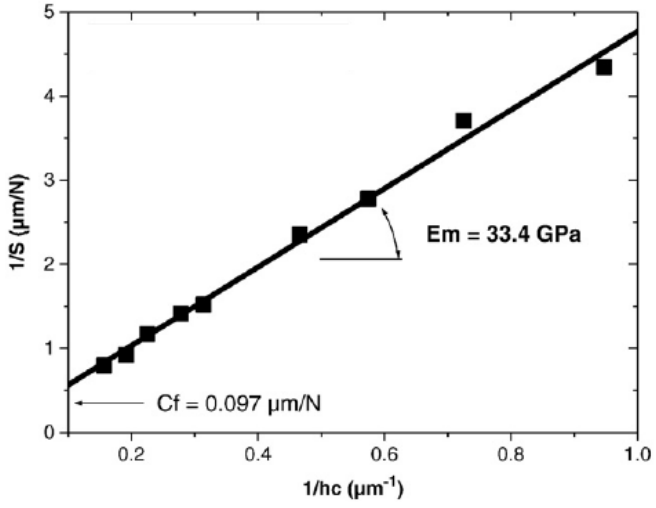

Fig. 3.4. Inverse of the unloading slope as a function of the inverse of the indentation depth, to determine frame compliance and bulk modulus for HA coatings [52].

CHAPTER 4

AIM OF THE WORK AND RANGE OF RESEARCH

As a result of literature review it is clear, that suspension plasma spraying is one of the most intensively studied deposition technique. It leads to wide range of possible applications of these coatings. The thesis of this PhD work is:

"It is possible to obtain with suspension plasma spraying coatings with appropriate properties, will enable them to be implemented in different applications."

The scientific goal of the PhD work is to put knowledge of the microstructure and mechanical, thermal transport and photocatalytic properties of suspension plasma sprayed coatings. Moreover, the influence of spray parameters on the properties should be known.

The useful goal is to find rewarding spray parameters for all materials used to obtain the coatings: hydroxyapatite, titanium dioxide and stabilized zirconia

Scheme of research range, made in PhD work is presented in Fig. 4.1.

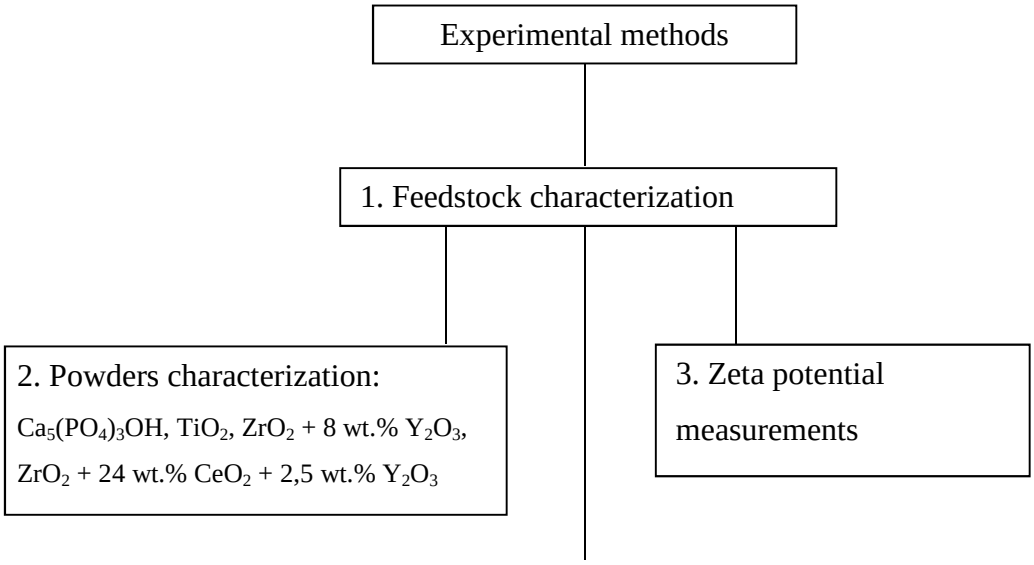

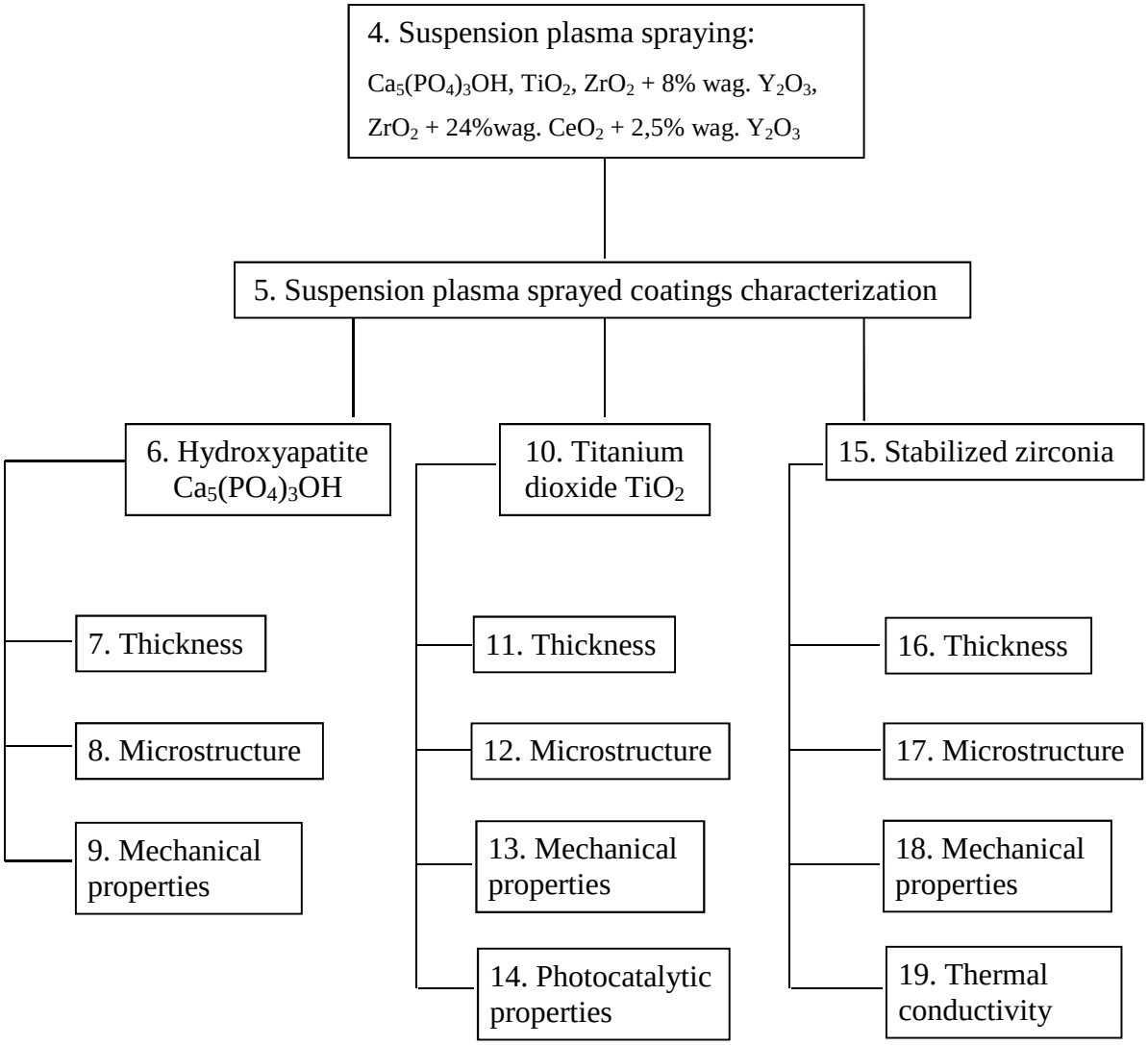

Fig. 4.1. Scheme of research range.

CHAPTER 5

CHARACTERIZATION OF USED MATERIALS

In this thesis four powders were used, hydroxyapatite, $Ca_{10}(PO_4)_6(OH)_2$, *HA*, titanium dioxide, *TiO_2* and two types of ceramic powder based on zirconia dioxide, yttria stabilized zirconia, ZrO_2 + 8 wt.% Y_2O_3, *YSZ*, and yttria with ceria stabilized zirconia, ZrO_2 + 25 wt.% CeO_2 + 2.5 wt.% Y_2O_3, *YCSZ*. All kinds of powder were been handled as solid fraction into liquid carrier (suspensions). Details concerning using powders and suspensions formulation are presented below.

5.1. HYDROXYAPATITE

Hydroxyapatite, $Ca_5(PO_4)_3OH$, *HA* belongs to the biomaterials. It means that these materials interact with biological systems not causing any unacceptable harm to the body. *HA* has been used since 1990 as coating on prostheses of e.g. hip, knees, teeth in order to enhance their biointegration to a bone [52]. HA powder was synthesized by a wet method using calcium nitrate and diamonium phosphate in ammoniacal solution by Dr R. Jaworski (ENSC Lille, France). Details are described elsewhere [53, 54]. The morphologies of the HA powder are presented in Fig. 5.1. After the synthesis the powder has a very small grain size, whereas after calcination it is observed, that grains started to be larger. Consequently, powder after calcination needed to be crushed.

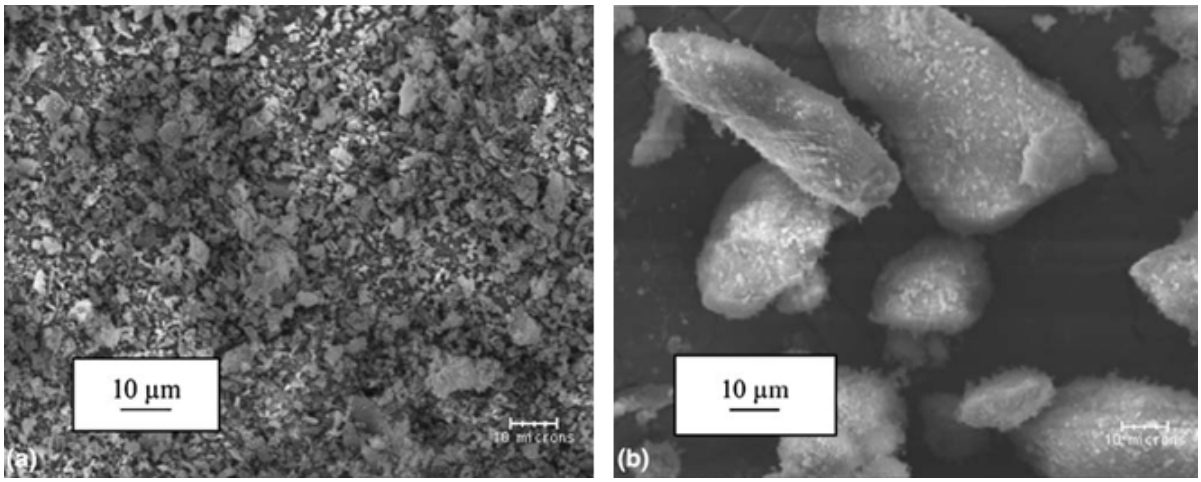

Fig. 5.1. Morphologies of HA powder particles after synthesis and drying (a) and after calcinations (b) [53].

Selected physical properties of bulk HA were given by Dyshlovenko et al. [55] and are presented in Table 5.1.

Table 5.1. Selected properties of bulk HA [55].

Property	Value
Heat of melting, kJ/mol	15.50
Melting point, K	1843
Heat of evaporation, kJ/mol	45.24
Boiling point, K	3500
Molecular mass, kg	$1.668 \cdot 10^{-24}$
Density, kg/m^3	3156
Thermal expansion coefficient., K^{-1}	$13.3 \cdot 10^{-6}$

The powder had a monomodal size distribution with a mean diameter of about 1 μm when tested in ethanol (Fig. 5.2a). The distribution, while tested in water, has bimodal character with the agglomerates centered around 3 and 10 μm [54], which is visible in Fig 5.2b. This difference is caused by more negative zeta potential of ethanol based suspension and consequently, it was more stable.

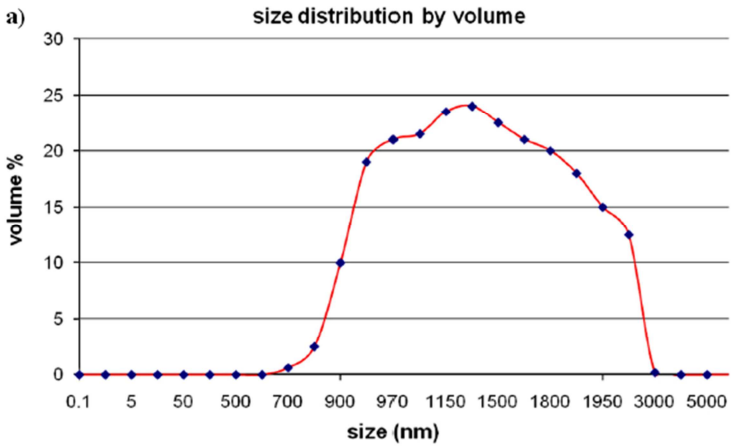

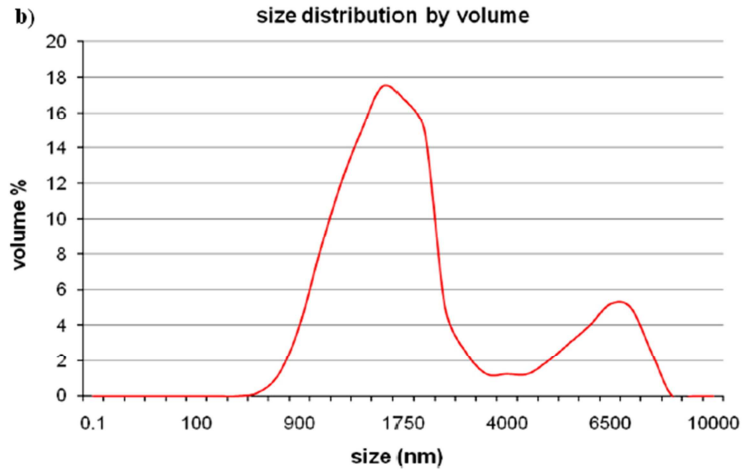

Fig. 5.2. Size distribution of calcinated and ball-milled HA in ethanol (a) and in distilled water (b) measured by dynamic laser scattering [54].

5.2. TITANIUM DIOXIDE

Titanium dioxide, TiO_2 coating have been intensively studied in the past years. There are many applications of these coatings, such as, hydrogen and oxygen sensors, self-cleaning and photocatalytic surfaces for the degradation of organic pollutants, electron emitters for light emitting devices and even destruction of some types of bacteria [56]. Titanium dioxide was a commercial rutile *Tioxide R-TC90* powder (Huntsmann Tioxide, England). Size distribution of TiO_2 powder and its photos are presented in Figs 5.3 and 5.4, respectively.

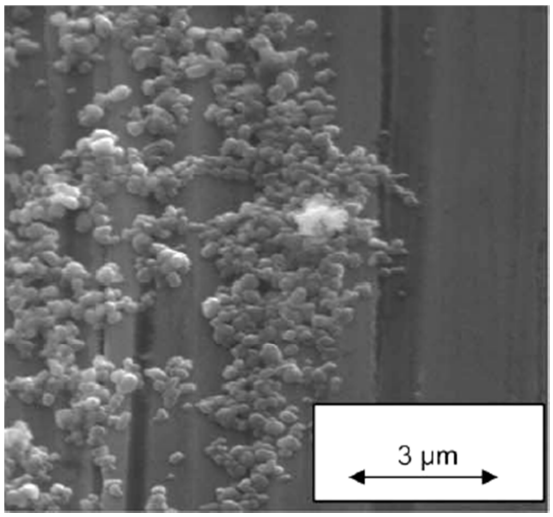

Fig. 5.3. SEM (secondary electrons) of TiO_2 powder [57].

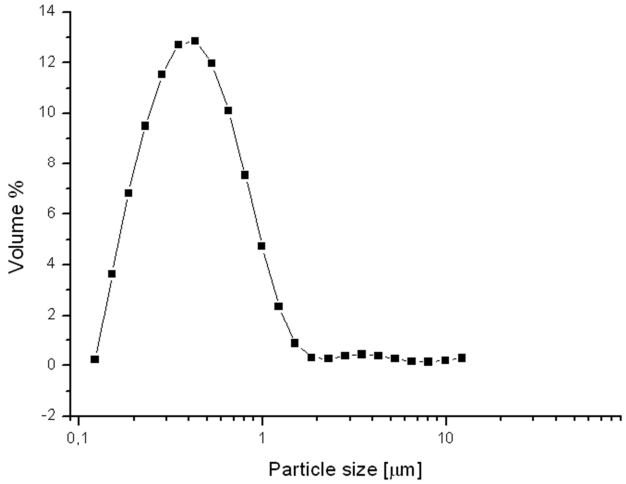

Fig. 5.4. Size distribution of TiO_2 powder measured by dynamic laser scattering.

Morphology and chemical properties of this powder are described in [57]. Selected properties of TiO_2 are collected [58] and presented in Table 5.2.

Table 5.2. Selected properties of TiO_2 [58].

Property	Value
Density*, kg/m^3	4260 or 3840
Modulus of elasticity, GPa	230
Microhardness, (HV 0.5)	880
Shear modulus, GPa	90
Thermal expansion coefficient., K^{-1}	$9 \cdot 10^{-6}$
Thermal conductivity (at 25°C), W/(m·K)	11.7

* it depends on TiO_2 phase, rutile or anatase, respectively

5.3. STABILIZED ZIRCONIA OXIDES

In this work two kinds of ceramics based on zirconium dioxide were used, it was yttria stabilized zirconia, *YSZ*, and yttria with ceria stabilized zirconia, *YCSZ*. The initial powders were commercially available products: Metco 204NS and 205NS, respectively. The composition of commercial product is ZrO_2 + 8 wt.% Y_2O_3, it is prepared by spray drying and particle size is in range -125 + 11 μm. The apparent density of this powder is 2.3±0.2 g/cm^3 and the melting point is equal to 2800°C [59]. The mean diameter of the coarse powder was measured to be equal to d_{VS} = 38 μm. The composition of the 205NS powder is ZrO_2 + 25 wt.% CeO_2 + 2.5 wt.% Y_2O_3 and it was prepared by spray drying. Particle size is in range -90 + 16 μm and the volume-surface mean diameter was measured to be equal to d_{VS} = 38 μm. The morphology of coarse 204NS and 205NS powders is presented in Fig. 5.5.

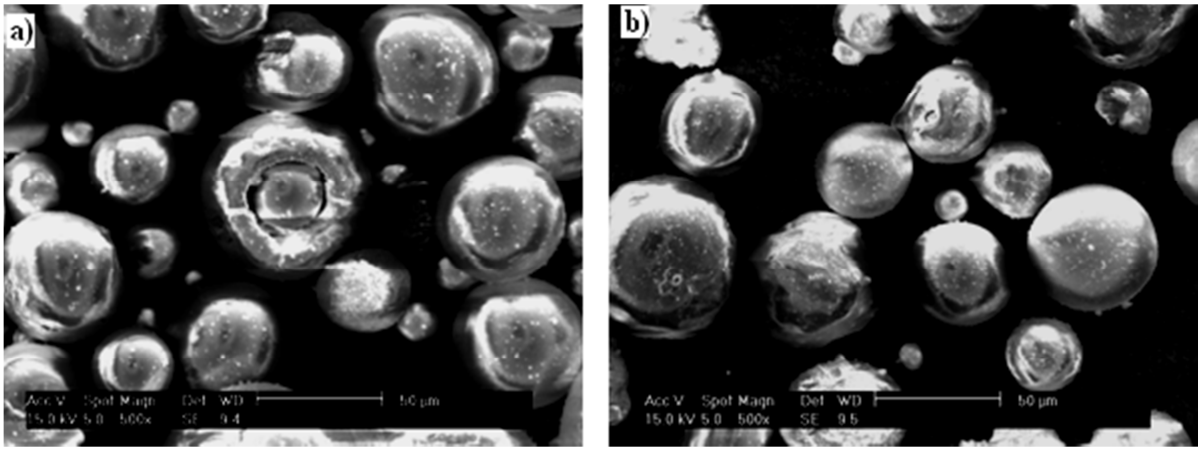

Fig. 5.5. SEM (secondary electrons) of coarse powders, 204NS (a) and 205NS (b).

Both of these powders, but more often 204NS, are frequently used to obtain thermal barrier coating. 205NS powder has good shock resistance and good resistivity to high temperature corrosion, so it is often used for turbine hot section components [60].

Before spraying powders were crushed in attrition milling device.

CHAPTER 6

EXPERIMENTAL METHODS

6.1. POWDER AND SUSPENSION PREPARATION

Coatings deposition by suspension plasma spraying needs fine powders to be used, even in a nanometric scale. Also the technology of suspension preparation is one of the fundamental parameters, which could influence on coating properties.

6.1.1. BALL MILLING

Because of a great size of initial size of coarse powders, it was necessary to crush them. Mechanical ball milling was used to this end. This process was realized using moliNEx system (NEZTSCH, Germany), which is presented in Fig. 6.1. Zirconia balls were used as grinding medium whereas ethanol was used as cooling medium. Milling was performed with some dispersant to prevent agglomeration during process.

After the milling process powders were sieved using sedimentation sieves to prevent big particles from moving into the suspension.

Fig. 6.1. View of attrition milling device moliNEx system (NETZSCH).

6.1.2. GRANULOMETRY

Particle size distribution was measured with two types of devices, based on the laser diffraction analysis. The first one was Malvern Mastersizer X, presented in Fig. 6.2, and the other one was Partica LA-950V2 (Horiba), presented in Fig. 6.3.

Fig. 6.2. View of Malvern Mastersizer X particle size device [61].

In both equipments the principle of measurement was the same. The particles were transported through the cell and detected by laser beam. Finally its size distribution was registered and characteristic diameters, e.g. d_{VS}, were obtained from measurements.

Fig. 6.3. View of Partica LA-950V2 (Horiba) device.

6.1.3. SUSPENSION FORMULATION

In the presented work all formulated suspensions had the fraction of fine solids and the same liquid solvent. Every suspension consists of 20 wt.% of dry powder, with or without

milling, depending on the initial particles size distribution, and 40 wt.% of distilled water and 40 wt.% of ethanol. Scheme of suspension preparation is presented in Fig. 6.4.

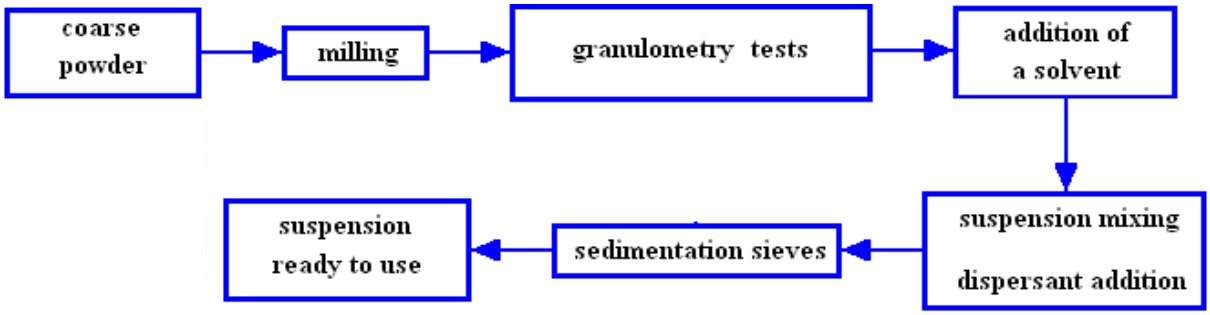

Fig. 6.4. Scheme of suspension formulation for suspension plasma spraying.

6.2. THERMAL SPRAY INSTALATION

Thermal spraying experiments and coatings manufacturing were performed using a set up installation presented in Fig. 6.5. The plasma torch was mounted on 5-axis IRB-6 of ABB industrial robot. Work table was connected with vacuum pump and had a function of sample holder. Substrates were fixed on table by vacuum pump and airflow duct system.

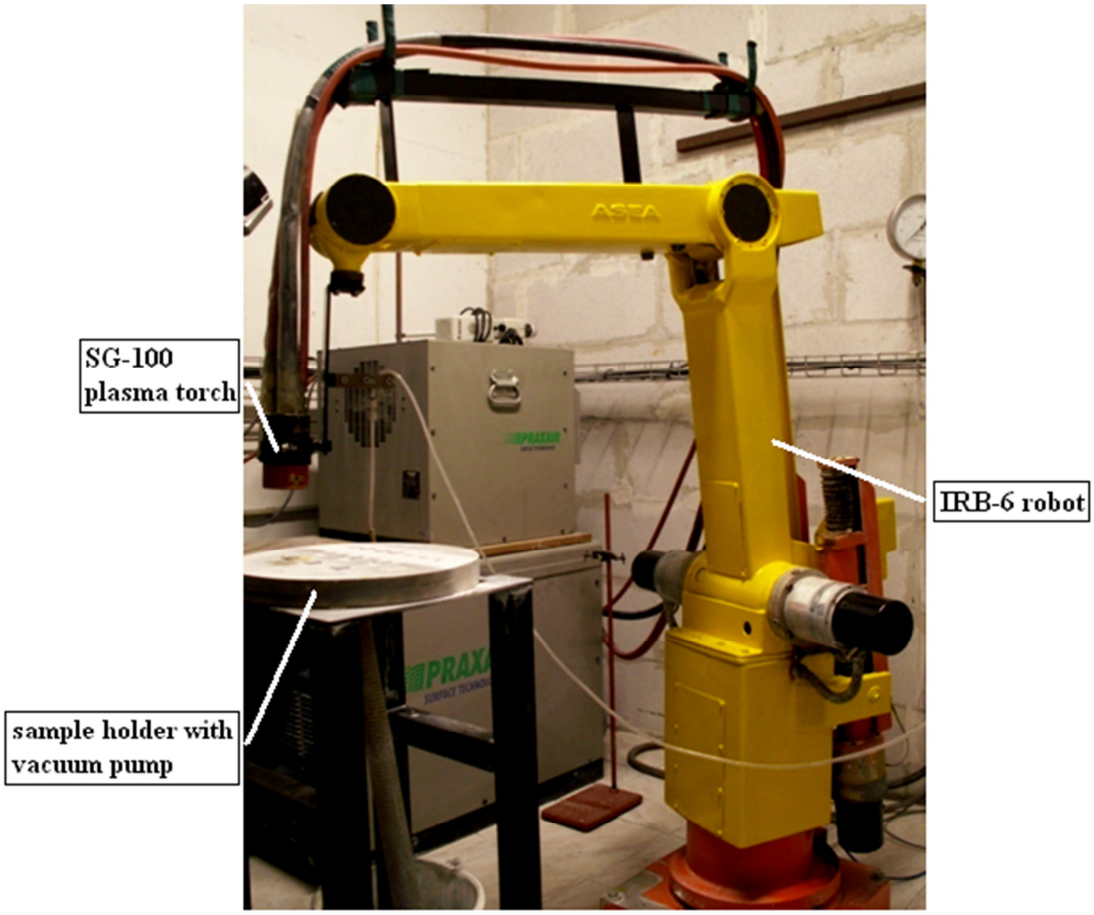

Fig. 6.5. View of plasma spraying installation set up.

The surface temperature was measured using a pyrometer IN 5 Plus of Impac (Erstein, France), which is presented in Fig. 6.6. This device is sensible in the far i.r. (wavelength's from 8 to 14 μm). The measurements of coating surface temperature were performed with distance of 30 cm from the surface.

Fig. 6.6. View of pyrometer IN 5 Plus.

To register the changes in coatings surface temperature as a function of time an *InfraWin* software was used. Typical coatings surface temperature vs. time of spraying is presented in Fig. 6.7.

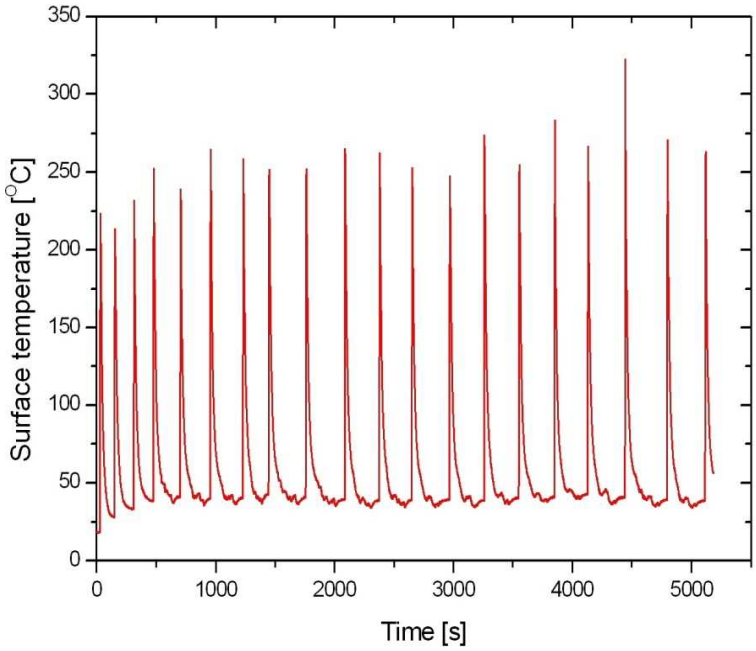

Fig. 6.7. Typical function of coatings surface temperature in time during spraying.

6.2.1. PLASMA TORCH

All experiments were performed using a plasma torch model SG-100 of Praxair S.T. (Indianapolis, IN, USA) with the anode 03083-175 and the cathode 03083-129 and the gas injector 03083-112. It is a single cathode DC torch. The diagram of a typical DC torch is presented in Fig. 6.8.

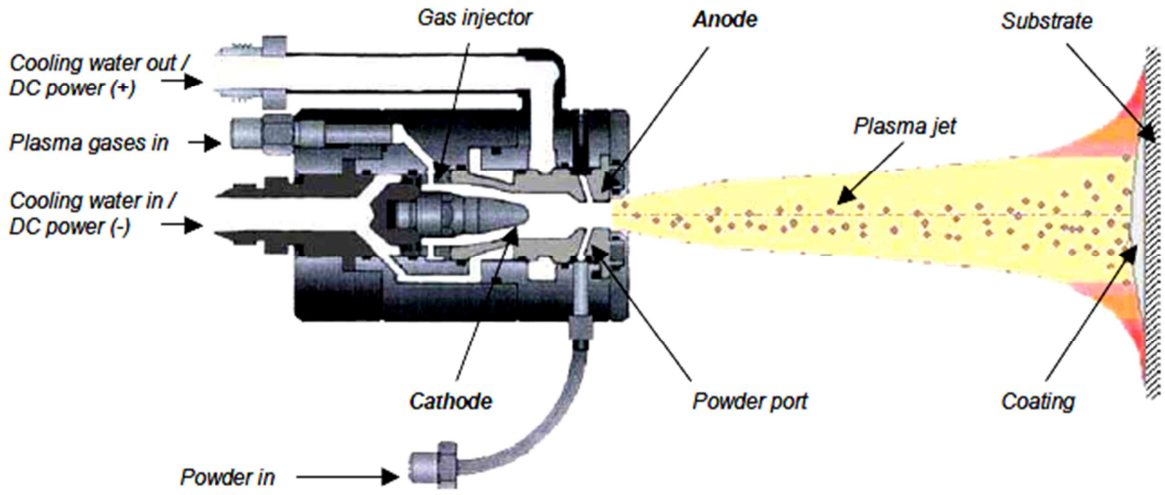

Fig. 6.8. Diagram of SG-100 plasma torch [3].

6.2.2. SUSPENSION INJECTION

The suspensions were introduced radially inside of a torch anode-nozzle (Fig. 6.9) using a continuous jet injector with internal diameter, *ID*, equal to 0.5 mm.

Fig. 6.9. View of set up of internal mode with the use of continuous jet nozzle injector installed inside the plasma torch [56].

Before injection of the suspension into plasma jet, it is mixed by a magnetic agitator, in a container. The pneumatic system for the suspension plasma spraying with the diagram of the reservoir with suspension are presented in Fig. 6.10a and b, respectively. This mode makes it possible to control the flowrate of suspension by the pressure of compressed air.

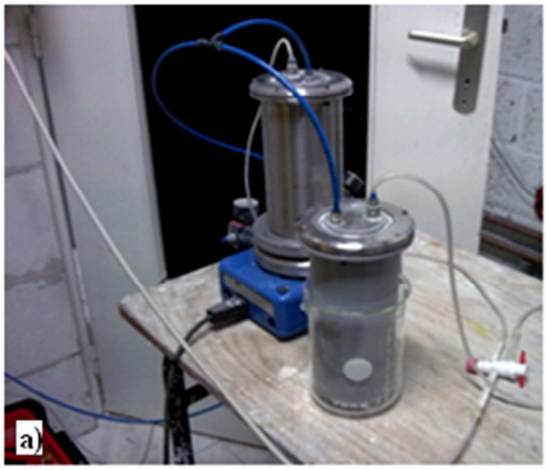

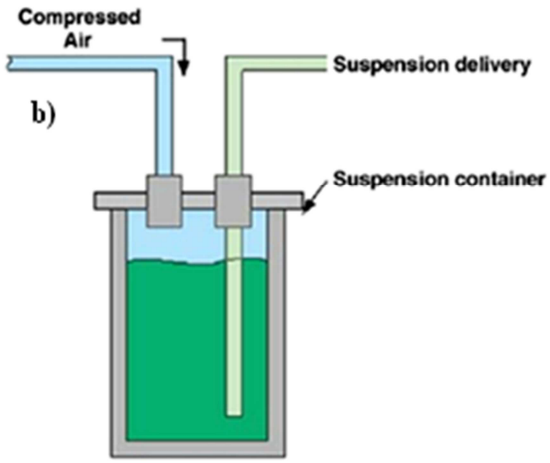

Fig. 6.10. Pneumatic system of reservoirs with suspension and cleaning water (a) and schematic of liquid feedstock delivery by pneumatic system (b) [8].

6.2.3. SPRAY PARAMETERS

In all thermal spraying techniques there are many parameters, which influence the coatings properties. That is why one needs a careful control and good understanding of the process [62]. In this work, two-level full factorial design (2^k) was used to optimize produced coatings. This method was chosen, consider the interactions between spray parameters. The plan of experiment also includes an experiment in the center of the area. The example of full factorial (2^k, k = 2) design of experiment (DEO) is presented in Fig. 6.11. Numbers in circles correspond to the experimental runs.

The most frequently chosen variables were spray distance, linear torch velocity and electric power input. On the other hand constant parameters were injection nozzle internal diameter, composition and feed rate of working gases (45 slpm of argon and 5 slpm of hydrogen). Liquid phase was composed from water and ethanol in mass ratio 1:1 and solid phase was 20 wt.%. Suspension feed rate was about 20 g/min.

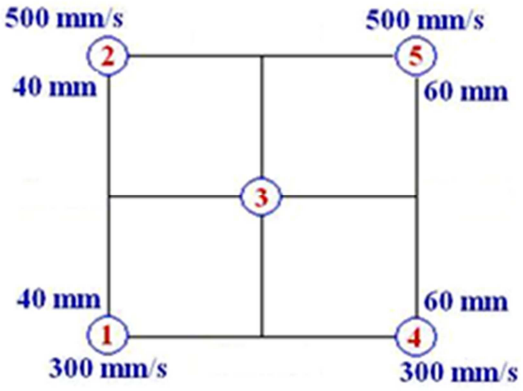

Fig. 6.11. Full factorial design of experiment, 2^k, k = 2, method.

6.2.4. POST SPRAY TREATMENT

In this work only one type of post spray treatment was used. It was a in vitro corrosion test, which was realized by immersion of the samples in simulated body fluid (SBF). This liquid has a composition originally proposed by Kokubo *et al*. [63]. SBF used in this work, was formulated from products, which are presented in Table 6.1. After mixing all ingredients,

pH of liquid was measured and it was equal to 7.4. Samples with HA coatings were closed in small containers with SBF and put into distilled water kept in a constant temperature of 37 °C. Samples were submitted in SBF bath for 3, 7, 14, 28 and 60 days.

Table 6.1. Products used to formulate simulated body fluid used *in vitro* tests [64].

Products	Quantity
Water ultra-pure (Milli Q)	750 ml
NaCl	7.996 g
$NaHCO_3$	0.350 g
KCl	0.224 g
K_2HPO_4	0.174 g
$MgCl_2 \cdot 4H_2O$	0.251 g
HCl (1 mol/l)	40 ml
$CaCl_2$	0.278 g
Na_2SO_4	0.071 g
$(CH_2OH)_3CNH_2$	6.057 g

6.3. COATINGS' CHARACTERIZATION

Coatings, which were prepared by suspension plasma spraying were characterized to find thickness, roughness, microstructure and other properties obtained coatings.

6.3.1. THICKNESS

Thickness of coatings was estimated on metallographically prepared cross-section of samples, which were observed using the optical microscope Nikon Eclipse LV100, presented in Fig. 6.12. The mean thickness of a coatings was found from 15, up to 30 measurements in different region of coatings.

Fig. 6.12. View of optical microscope Nikon Eclipse LV100 set up.

6.3.2. ROUGHNESS

Roughness investigations were performed by using two kinds of instrument. One of them it was Somicronic ST-11a, presented in Fig. 6.13a. With this equipment it was possible to estimate roughness of the coatings and represent it by three, the most fundamental parameters, R_a, R_z and R_{max}. The measurements were carried out three times, with length of line equal to 8 mm. Then average values and standard deviation, σ, were calculated.

The principle of this measurement was the following. Measuring head, presented in Fig 6.13b, which is mobile during the measurement, was applied with a small force, only to make roughness profile of the coating surface. Work table, which is mobile too, during the measurement is fixed. The graphs represent roughness profiles were plotted on the screen.

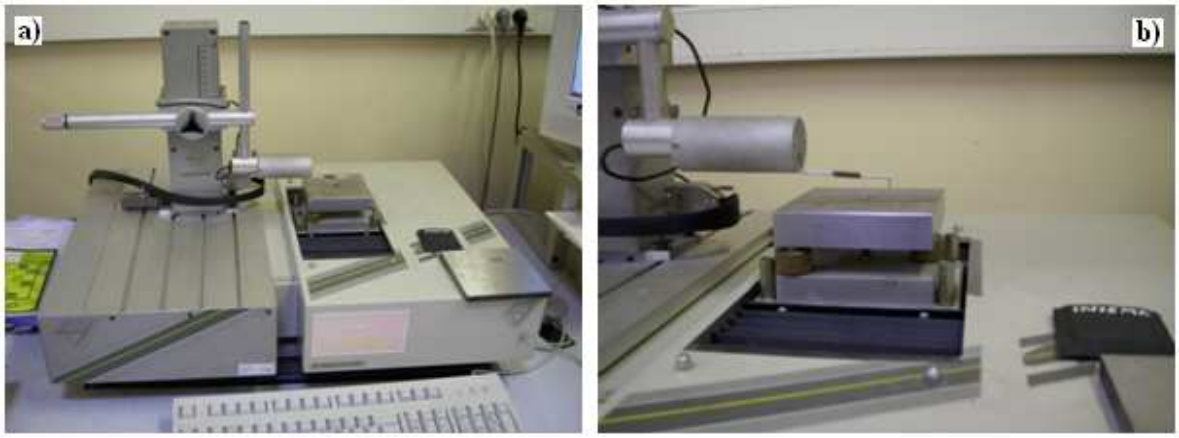

Fig. 6.13. Somicronic ST-11a instrument (a), and working table with measuring head (b).

Another instrument, which was used to determine roughness of the obtained coatings was Surtronic 25, Taylor Hobson product, presented in Fig. 6.14. With this equipment it is possible to estimate 10 parameters of roughness, according to specify application. In this work only two of them, R_a and R_z, were used. Principle of measurements and its technique were the same, like in case of Somicronic ST-11a instrument.

Fig. 6.14. View of Surtronic 25 instrument.

6.3.3. MICROSTRUCTURE

Microstructure of obtained coatings was characterized with scanning electron microscope (SEM) and X-ray diffraction (XRD) analysis.

Coating and powder morphologies were estimated using four different types of scanning electron microscopes:

- JEOL (Tokyo, Japan) set up of type JSM 5800LV;
- Philips 515 (Eindhoven, Netherlands);
- ZEISS NEON40 field emission SEM;
- JEOL (Tokyo, Japan) set up of type JSM 7404 field emission SEM.

The morphologies were observed on the surfaces of coatings as well as their cross-sections. Most of investigations were performed with secondary electrons, SE mode, but sometimes back-scattered electrons, BSE mode was used.

The phase composition was estimated with the use of X-ray diffraction analysis using a D8- Bruker apparatus (Bruker AXS, Karlsruhe, Germany) with Cu-Kα radiation in the range of 2θ angles from 20° to 60° and in some cases from 17° up to 120° (coatings based on zirconium oxide). The obtained patterns were identified using DIFFRAC+ Eva software, which bases on International Centre of Diffraction Data JCPDS-ICDD. The percentage of the phases in coatings were determined from the reference intensity ratio (RIR) method described

by Prevey [65], which uses the comparison of the strongest peak intensities. RIRs were calculated using the following files of the JCPDS data base:

- HA, hydroxyapatite, JCPDS 73-1731;
- α-TCP, tricalcium phosphate $Ca_3(PO4)_2$, JCPDS 70-0374;
- β-TCP, tricalcium phosphate $Ca_3(PO4)_2$, JCPDS 70-2065;
- TTCP, tetracalcium phosphate, $Ca_4P_2O_9$, JCPDS 70-1379;
- CaO, calcium oxide, JCPDS 82-1690.
- anatase (TiO_2), JCPDS 21-1272;
- rutile (TiO_2), JCPDS 78-2406;
- tetragonal zirconia 8YSZ, JCPDS 48-0224;
- monoclinic zirconia 8YSZ, JCPDS 06-9855;
- tetragonal zirconia 24CeYSZ, JCPDS 13-9723.

The phase composition of some coatings (based on zirconium oxide) was estimated in details using TOPAS V4.1 software, which is based on Rietveld method, which makes it possible to determine the phase composition and the lattice parameters estimation.

6.4. COATINGS' PROPERTIES

Suspension plasma sprayed coatings can have many possible applications. Depending on possible application adequate properties of sprayed coatings are tested. In this section methods of properties determination are presented. It is divided into three parts related to mechanical, thermal transport and photocatalytic properties.

6.4.1. MECHANICAL PROPERTIES

The most important property of all coatings is adhesion to the substrate. In case of conventional thermal spraying techniques testing this property is normalized by ASTM 633-01 [66] tensile adhesion test and in Polish standard PN-EN 582:1993 [67]. The required thickness of the coating is 380 μm. However in case of suspension thermal spraying the typical coatings' thicknesses are in range from 10 to 50 μm. In consequence, these coatings need another methods of adhesion determination.

The appropriate methods of SPS coatings' adhesion determination are the scratch test and the interface indentation test [8]. There are two criteria guiding selection the appropriate method, namely their thickness and hardness. For thinner coatings the scratch test is more useful, whereas for thicker and harder ones, the interface indentation test is better. Moreover, with the latter it is possible to know the influence of the residual stresses or thermal treatments effect on the adhesive properties [30]. On the other hand, the scratch test helps to estimate of coatings' cohesion. The scratch test is used mainly to determine the adhesion of thin, hard films, obtained by PVD or CVD methods [2.22]. This method is also useful to adhesion characterization of thin suspension plasma sprayed coatings. Fig. 6.15. presents experimental set up scratch test.

Fig. 6.15. CSM+ instrument for scratch test investigations.

The method bases on the displacement of Rockwell diamond tip on the coating surface. Velocity of stylus is constant, whereas normal load can be either constant or can

increase with a constant rate. During the test, the indenter introduces stresses at the interface between coating and substrate. It results, finally, in a coating delamination, which is schematically presented in Fig. 6.16. The adhesion of the coating is represented by the critical load, L_C, at which the failure is detected. This parameter is most often determined by detecting the changes in acoustic emission. Optical microscope is used to confirm the value of the critical load. The specification of a critical load by optical microscope observation bases on identification of beginning of visibility of substrate inside of the scratch channel [68]. The scratch test makes it possible to determine the coatings' cohesion. The cohesion is related to scratch hardness. This test is very similar to the typical scratch one, with one exception, namely the normal load is constant. The scratch hardness is calculated from the following equation:

where:

HS_L – scratch hardness [Pa]

L – applied normal load [N]

d – corresponding scratch width [m]

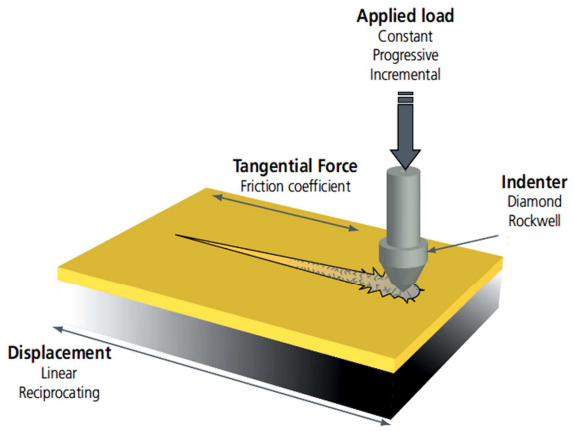

Fig. 6.16. Scheme of scratch test [69].

Hardness and elastic modulus of suspension plasma sprayed coatings were estimated with microhardness tester CSM 2-107 equipped with Vickers indenter, presented in Fig. 6.17.

Fig. 6.17. Microhardness tester CSM 2-107 equipped with Vickers indenter.

Measurements and calculations of hardness and elastic modulus of tested coatings were made with methodology described in chapter no. 3.

6.4.2. THERMAL TRANSPORT PROPERTIES

Thermal diffusivity could be measured with a non-destructive method, single side thermographic technique, described in detail in [70] and presented in Fig. 6.18. Thermal diffusivity of a two-layer sample, ceramic coating and metallic substrate, was determined by fitting the spatial average temperature in function of time, *T(t)*, of the front sample surface after being heated by a laser pulse. It can be a laser or xenon lamp. Temperature evolution can be observed by an infrared camera. The maximum coatings surface temperature increases by just a few milliseconds after the flash of 10-30 K. To fit the experimental data one-dimensional two layer model was adopted, as follows:

$$T(t) = \frac{Q_0}{\varepsilon_c \cdot \sqrt{\pi \cdot t}} \cdot \left[1 + 2 \sum_{n=1}^{\infty} \Gamma^n \cdot e^{-\frac{n^2 l_c^2}{\alpha_c t}} \right] \qquad (6.2)$$

where:

Q_0 – absorbed energy density

ε_c, ε_s – thermal effusivity of coating and substrate

Γ – reflection coefficient at the interface between coating and substrate

l_c – coating thickness

The relations, from which thermal effusivity, ε and reflection coefficient, Γ are determined, are presented in detail elsewhere [71].

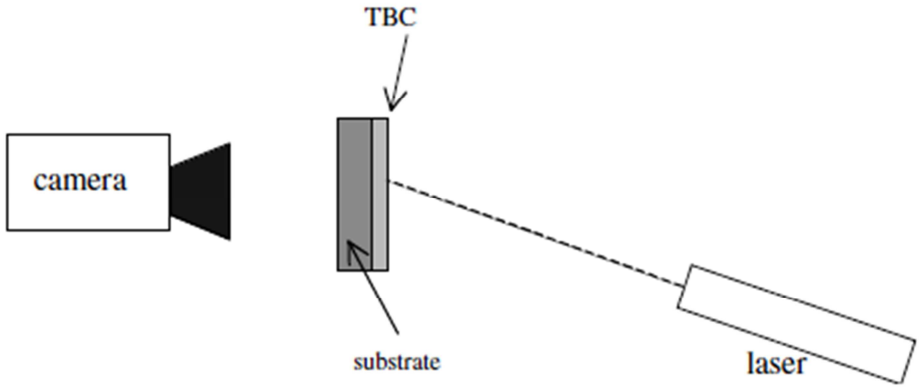

Fig. 6.18. Diagram of experimental laser flash set-up to measure thermal diffusivity of coatings [70].

Before measurements, a thin layer of colloidal graphite was painted on the coatings. This treatment was used to render coatings opaque for the flash radiation. As it was reported in [70, 72], the uncertainty of this method was determined in the range 5 to 7%. Thermal conductivity is calculated from following relation:

where:

a – thermal diffusivity [m^2/s]

ρ – density [kg/m^3]

c_p – specific heat [J/(kg·K)]

Thermal diffusivity of coatings was be determined using NETZSCH's LFA 447 NanoFlash® Light Flash System. The diagram of this instrument is presented in Fig. 6.19. The set up has the temperature range from RT to 250°C. The measurements were made with the use of the coatings sprayed on the substrate and the 2-layers numerical model was developed to determine thermal diffusivity of the coatings. Thermal diffusivity was calculated from the well-known expression [73]:

$$a = \frac{0.1388 \cdot d^2}{t_{0.5}} \qquad (6.4)$$

where:

a – thermal diffusivity [m^2/s]

d – sample thickness [m]

$t_{0.5}$ – half rise time [s]

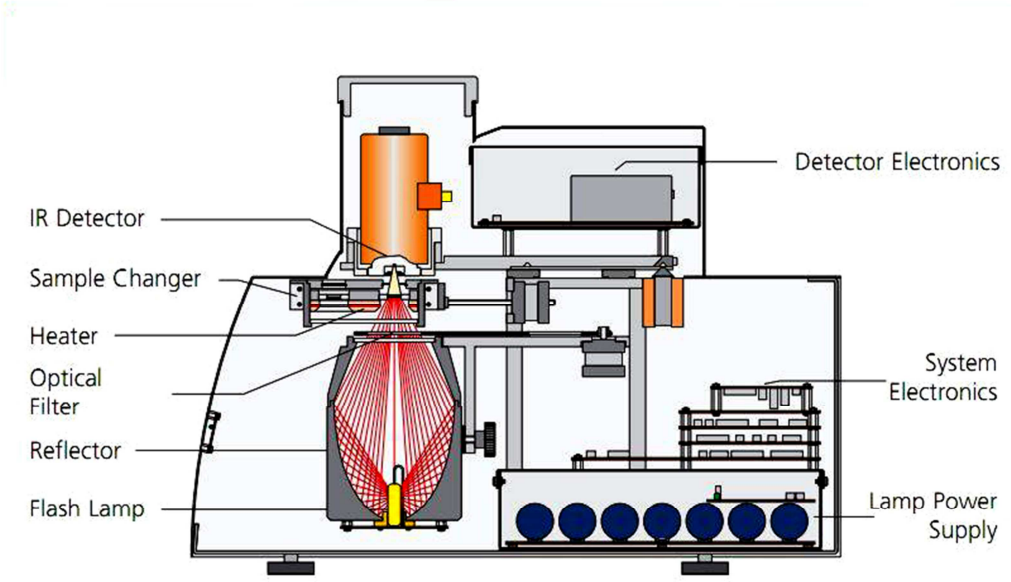

Fig. 6.19. Diagram of LFA 447 NanoFlash® Light Flash System [74].

The value of $t_{0.5}$ corresponds to the 50 % of sample's back face temperature rise. The measurements of thermal diffusivity were made for the coatings on stainless steel substrates. Consequently, the corresponding model of two layers was used. The model includes corrections resulting from: (i) heat losses; (ii) pulse duration, and (iii) contact resistance. The model is incorporated in the diffusivity set-up software.

Thermal conductivity was calculated from the following expression:

$$\lambda = a \cdot \rho_{300} \cdot c_p \cdot \left(\frac{\Delta L}{L}\right)$$

where:

λ – thermal conductivity [W/m·K]

c_p – specific heat [J/(kg·K)]

ρ_{300} – apparent density [kg/m^3]

$\Delta L/L$ – thermal dilatation [–]

Specific heat for alloys or composites is calculated from Kopp-Neumann law, which from mathematical point of view is weighted average of specific heat and content of every ingredient in alloy or composite.

$$c_p = \sum_{i=1}^{n} (c_{pi} \cdot f_i) \qquad (6.6)$$

where:

c_{pi} – specific heat of ingredient

f_i – content of ingredient

6.4.3. PHOTOCATALITYC PROPERTIES

Photocatalytic activity is one of the interesting features of TiO_2 coatings. The possible applications of these coatings is self-cleaning of the surfaces [75]. In general, photocatalytic activity is correlated with the content of the anatase phase in the coating. This content is calculated from following equation [76]:

$$C_{Acor} = \frac{8 \cdot \frac{I_A}{\rho_A}}{13 \cdot \frac{I_R}{\rho_R} + 8 \cdot \frac{I_A}{\rho_A}} \qquad (6.7)$$

where:

C_{Acor} – volume percentage of the TiO_2 anatase phase

I_A – intensity of the [101] peak of anatase

I_R – intensity of the [110] peak of rutile

ρ_A – density of anatase, is equal to 3.9 g/cm^3

ρ_R – density of rutile, is equal to 4.2 g/cm^3

The photocatalytic activity of TiO_2 suspension sprayed coatings was evaluated by the degradation of an aqueous solution of methylene blue (MB) according to the German standard DIN 52980 [77]. TiO_2 samples, previously cleaned by irradiation (using a UV-lamp with the wavelength of λ = 254 nm) for about 16 hours, were immersed in a 10-µM aqueous solution of MB; after the adsorption equilibrium between MB and TiO_2 was reached, the system was irradiated with the UV-lamp (λ = 366 nm, density of radiation of 10 W/m^2) for 3 hours. The degree of discolouration of the MB solution was determined by absorbance measurements at λ = 664 nm using a UV-NIS-NIR spectrometer Varian Cary 500 at every 20 min. The specific photocatalytic activity, P_{MB} and the photon efficiency, ζ_{MB} of the coatings were calculated using the following equations:

$$P_{MB} = R_{dark} - R_{irr} \qquad (6.8)$$

where:

P_{MB} – specific photocatalytic activity, [mol/(m^2·h)]

R_{dark} – specific degradation of MB in the dark (without UV radiation), [mol/(m^2·h)]

R_{irr} – specific degradation of MB during UV-irradiation, [mol/(m^2·h)]

and they are expressed by the formula:

$$R_{dark} = \frac{\Delta A \cdot V}{\Delta t \cdot \varepsilon \cdot d \cdot S} \quad \text{or} \quad R_{irr} = \frac{\Delta A \cdot V}{\Delta t \cdot \varepsilon \cdot d \cdot S} \qquad (6.9)$$

where ΔA is the variation of the absorbance of MB (determined at λ = 664 nm) in the time Δt, S [m^2] is the surface of titania coatings, d is the length of cell for spectroscopic measurements, in this case d was equal to 10 mm, V is the volume of the solution (corresponding to the volume percentage of the anatase phase, eq. 6.7), ε is the molar extinction coefficient of MB (ε_{MB} = 7402.8 m^2/mol).

Photon efficiency is calculated with the following formula:

$$\zeta_{MB} = \frac{P_{MB}}{E_P} \cdot 100 \qquad (6.10)$$

where:

ζ_{MB} – photon efficiency [%]

E_P – photon irradiance, E_P = 0.110 mol/(m^2·h)

CHAPTER 7

RESULTS

This chapter includes all information about feedstock and coating characterization. It is divided into two main parts: the first one deals with powders and suspensions characterization, whereas the other one focuses on coatings and their analysis.

7.1. FEEDSTOCK CHARACTERIZATION

The feedstock, which was used to produce different coatings, always contained 20 wt.% of solid, 40 wt.% distilled water and 40 wt.% of ethanol. Ceramic powders, based on zirconium oxide, were milled. Hydroxyapatite (HA) and TiO_2 powders were sprayed without milling.

7.1.1. POWDERS CHARACTERIZATION

As it was described in the previous chapter, four types of powder were used in following investigations: hydroxyapatite, titanium dioxide, yttria stabilized zirconia and yttria with ceria stabilized zirconia. The first two powders were described, because their particle diameters were small enough. Milling was carried out only for ceramic powders based on zirconium oxide.

A – yttria stabilized zirconia.

The initial powder was a commercial Metco 204NS. To crush it an attrition milling device (Fig. 6.1) was used. Zirconia balls with diameter of 1.85 mm were used as gridding medium whereas ethanol was used as cooling medium. Milling was performed without a dispersant to prevent agglomeration during the process. Rotation speed of the rotor was equal to 1000 rpm and the time of milling was 14 hours. 8YSZ powder after milling is presented in Fig. 7.1.

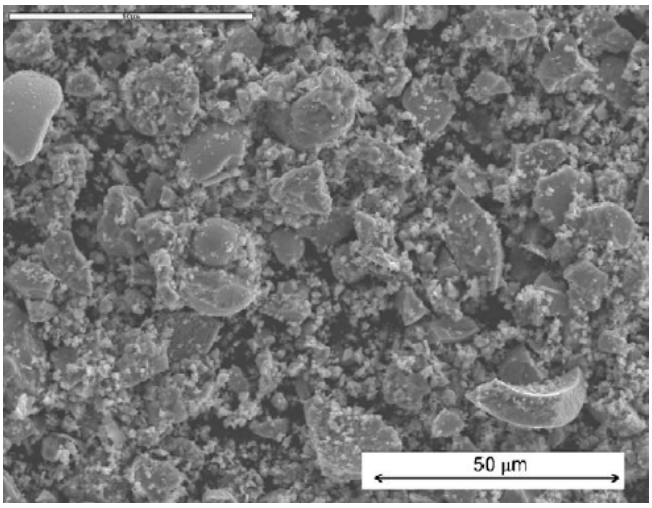

Fig. 7.1. SEM (secondary electrons) micrographs of 8YSZ powder after milling [71].

After milling, the granulometry tests were performed using dynamic laser scattering. The results are presented in Fig. 7.2. The mean diameter was equal to 1 µm, but the size distribution was bimodal with two maxima at about 0.3 µm and about 12 µm. The size distribution did not change significantly with longer milling time. Moreover, the bimodal size distribution was always observed.

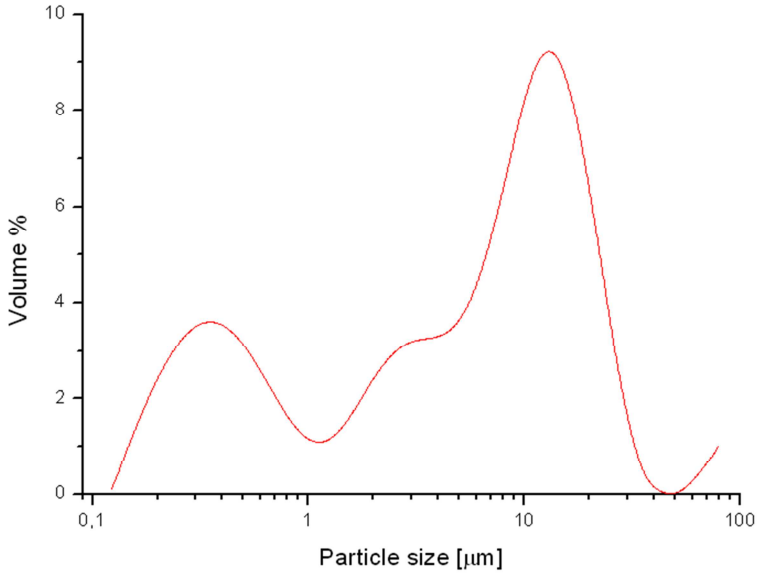

Fig. 7.2. Size distribution of 8YSZ powder after milling.

The results of the powder size distribution were not satisfactory because of the wide grain size distribution. The other milling parameters were used and the dispersant agent, Beycostat C213 was added. The change resulted in narrower and nearing to Gaussian grain size distribution. Fig. 7.3 presents powder 8YSZ after milling with the changed parameters.

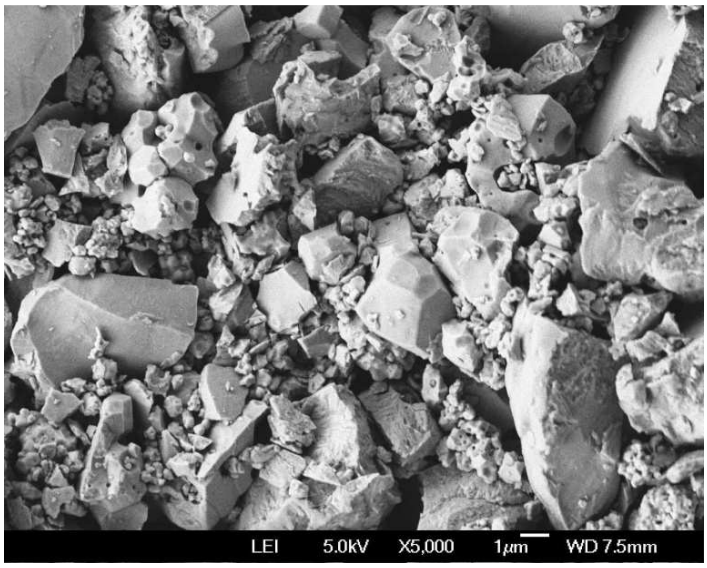

Fig. 7.3. SEM (secondary electrons) micrographs of 8YSZ powder after milling with changed parameters [78].

After milling, the granulometry tests were performed using dynamic laser scattering to determine the size distribution of particles. The results are shown in Fig. 7.5. The mean diameter was equal to 4.5 μm and more than 90 % of powder particles have diameter below 10 μm. Moreover, the size distribution was monomodal.

B – yttria with ceria stabilized zirconia.

This commercially available powder, Metco 205NS was crushed with the same milling parameters as in the case of the second series of 8YSZ powder. Powder 24CeYSZ after milling is presented in Fig. 7.4.

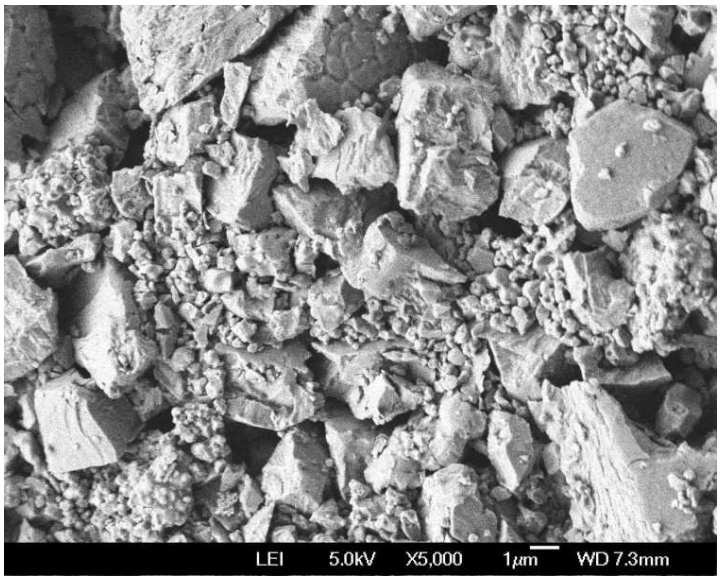

Fig. 7.4. SEM (secondary electrons) micrographs of 24CeYSZ powder after milling with changed parameters [78].

Similarly, as in the previous case, after milling the granulometry tests were performed using dynamic laser scattering to determine the size distribution of particles. The mean diameter was equal to 3.9 μm. Also more than 90 % of particles of this powder have diameter below 10 μm and the size distribution was monomodal.

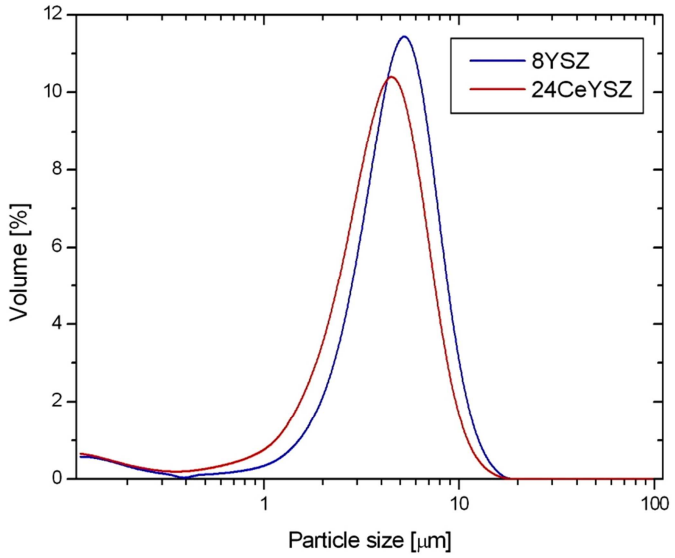

Fig. 7.5. Size distribution of 8YSZ and 24CeYSZ powders after milling with changed parameters and adding dispersant agent.

7.1.2. SUSPENSION CHARACTERIZATION

All suspensions were formulated with 20 wt.% of solid particles, 40 wt.% of distilled water and 40 wt.% of ethanol. The zeta potential of suspensions was characterized with Zetasizer Nano ZS (Malvern). The results of zeta potential measurements, ζ of HA suspensions are presented in Fig. 7.6. The measurements were made with two liquids solvents, ethanol and distilled water. In both cases the suspension was not stable enough, but it was better for ethanol-based one, ζ = -9 mV, than water-based, ζ = 4 mV.

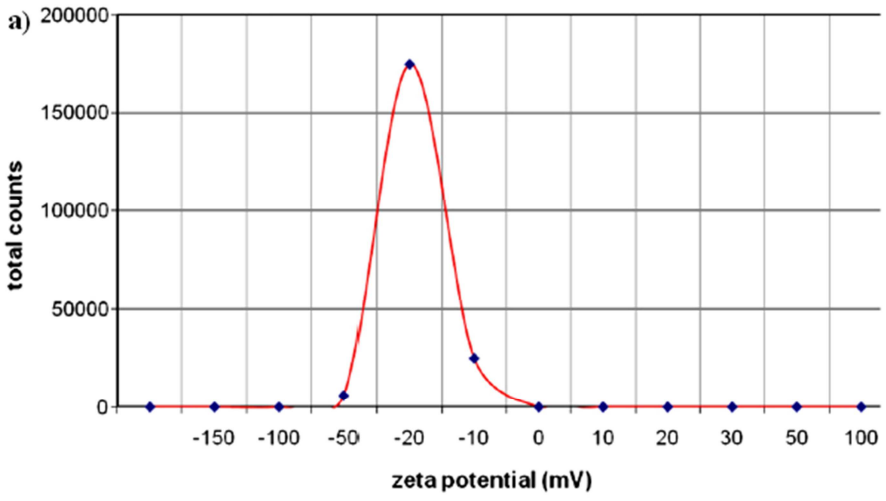

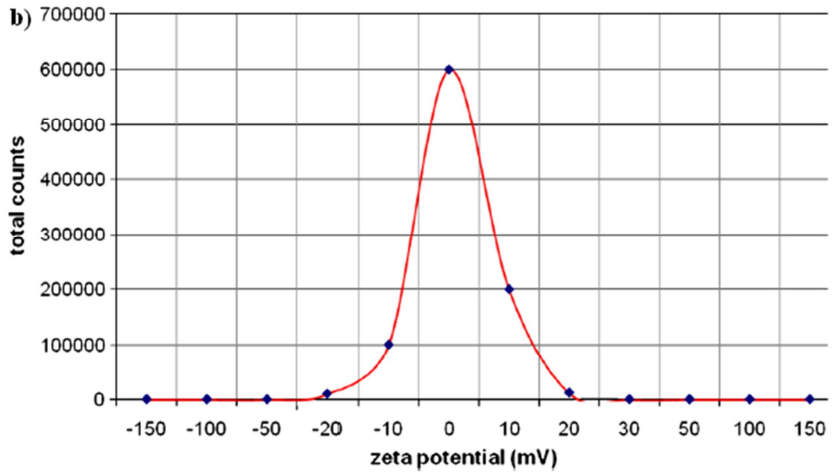

Fig. 7.6. Zeta potential distribution of HA suspensions: ethanol-based (a) and water-based (b) [54].

Zeta potential of the suspension formulate with 20 wt.% of TiO_2 powder with water and ethanol, in ratio 1:1, was equal to -3.4 mV, as it is presented in Fig. 7.7.

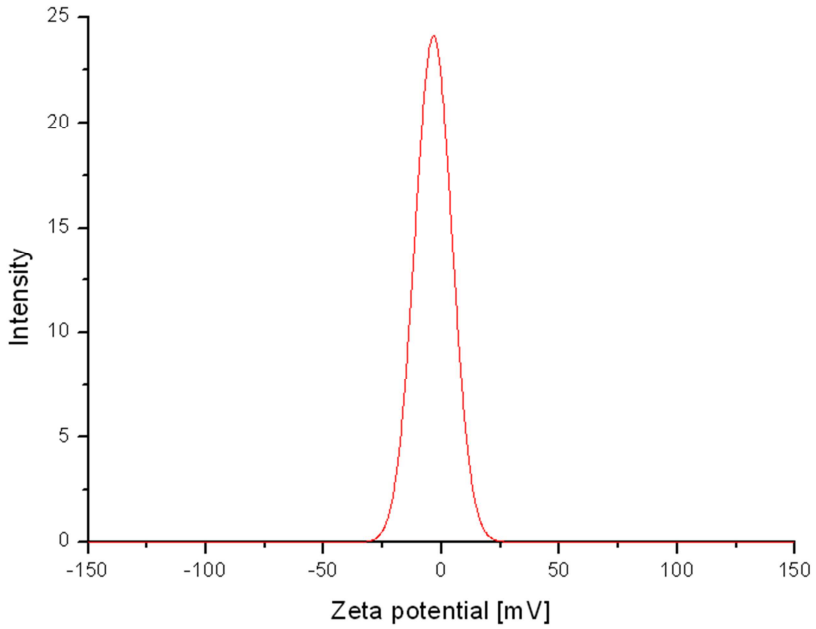

Fig. 7.7. Zeta potential of the suspension prepared using TiO_2 powder with water and ethanol (1:1 ratio).

During the preliminary studies on yttria stabilized zirconia coatings, different suspensions were be formulated and their zeta potential was estimated, as it is presented in Fig. 7.8. Zeta potential was -22 mV for water-based suspension, whereas for water and ethanol (ratio 1:1) it was -6 mV.

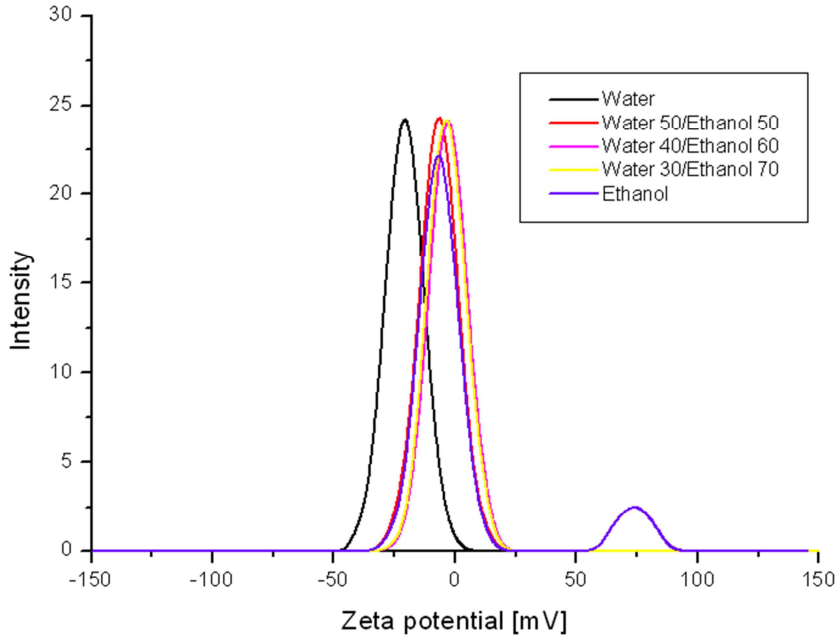

Fig. 7.8. Zeta potential distribution of different suspensions with ball milled ZrO_2 + 8 wt. % Y_2O_3 [71].

Ceramics based on zirconium oxide, yttria stabilized zirconia, 8YSZ and yttria with ceria stabilized zirconia, 24CeYSZ suspensions were not stable. To prevent particles agglomeration, a dispersant agent, phosphate ester (Beycostat C213, CECA) was added to both suspensions. They were formulated with water and ethanol, in ratio 1:1. The zeta potential distribution for these suspensions is presented in Fig. 7.9. The results of measurements are following: for 8YSZ, ζ was equal to -8,6 mV and for 24CeYSZ ζ was equal to -6,2 mV.

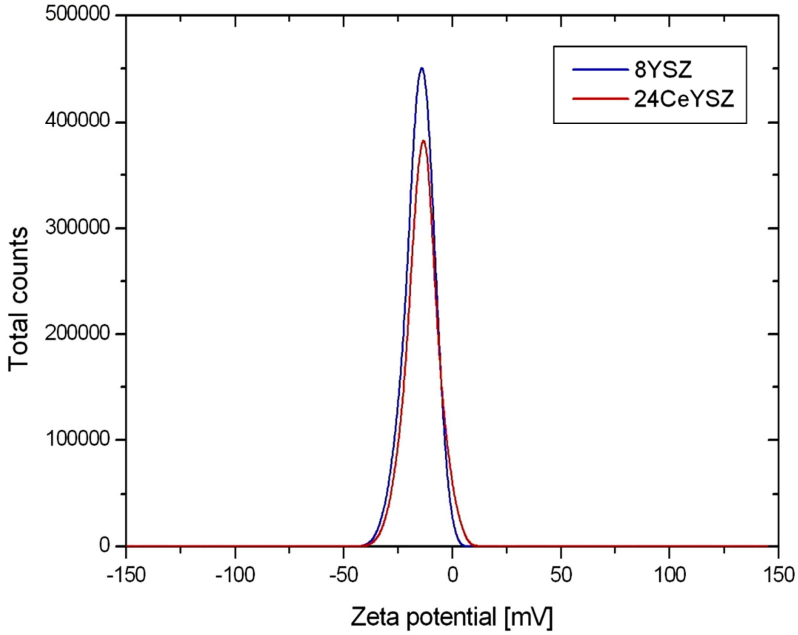

Fig. 7.9. Zeta potential of the suspension prepared using 8YSZ and 24CeYSZ powders with water and ethanol (1:1 ratio).

7.2. COATINGS CHARACTERIZATION

In this section the results of coatings characterization are presented. The spray parameters for every feedstock and all conditions of investigations are given. This section is divided into four parts, namely microstructure, mechanical, thermal transport and photocatalytic properties characterization.

7.2.1. MICROSTRUCTURE

Microstructure investigations of the obtained coatings concerned their morphology, investigated with scanning electron microscopy (SEM) and the phase composition determined using X-ray diffraction (XRD).

7.2.1.1. HYDROXYAPATITE COATINGS

SEM investigations were made on the coatings' surfaces and in their cross-sections using JEOL (Tokyo, Japan) set up of type JSM 5800 LV. Both kinds of detectors, secondary electrons and back-scattered electrons, were used in morphology investigations. Variable spray parameters are collected in Table 7.1. The surface of as-sprayed coating is shown in Fig 7.10 and their cross-section in Fig 7.11.

Table 7.1.Variable spray parameters and sample codes of suspension plasma sprayed HA coatings.

Experimental run no.	Spray distance [mm]	Electric power [kW]
1	60	30
2	50	27

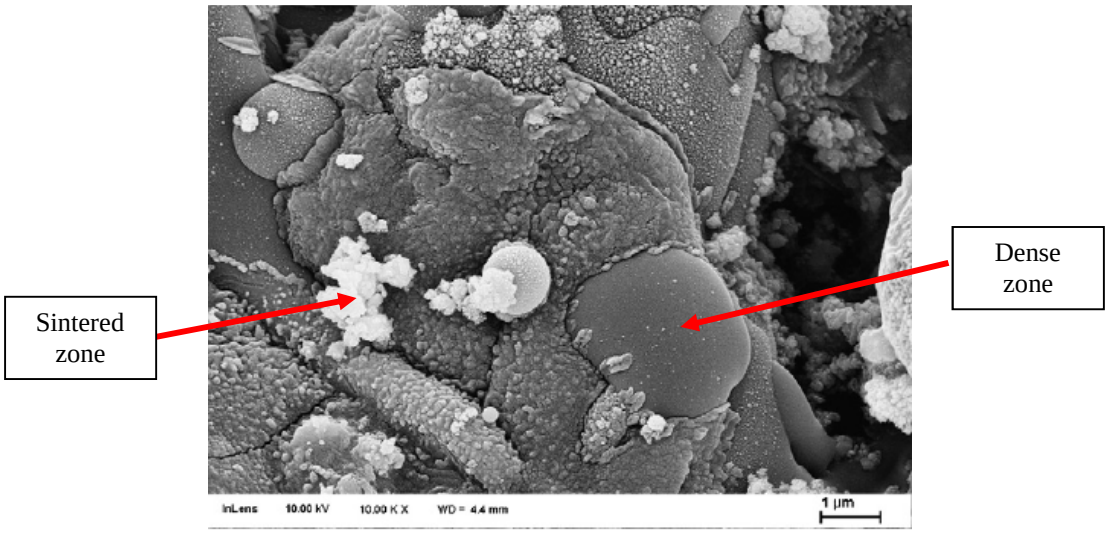

Fig. 7.10. SEM micrograph (secondary electrons) of the surface of as-sprayed sample no. 1 [52].

The microstructural research made it possible to find in the as-sprayed deposits two characteristic zones: (i) the dense zone corresponding to the lamellas, observed usually in thermally sprayed coatings; (ii) the sintered zone containing fine hydroxyapatite grains being the fine solids from the initial suspension. The coating is composed of well molten lamellae having the size of tenths of micrometers, which belong to the dense zone. The lamellae are neighbored by the sintered zone, which includes small nanometric or submicrometric grains corresponding to the initial solid feedstock in the suspension [64, 78, 79]. A similar microstructure was observed in all experimental runs. The sintered zone disappears at soaking and the coatings seem to be less porous. This densification was interpreted as the reprecipitation of the calcium phosphates dissolved in the SBF during soaking [4.5]. The microscopic observations indicated that the sintered zone starts to get dissolved in the SBF after 14 days of soaking.

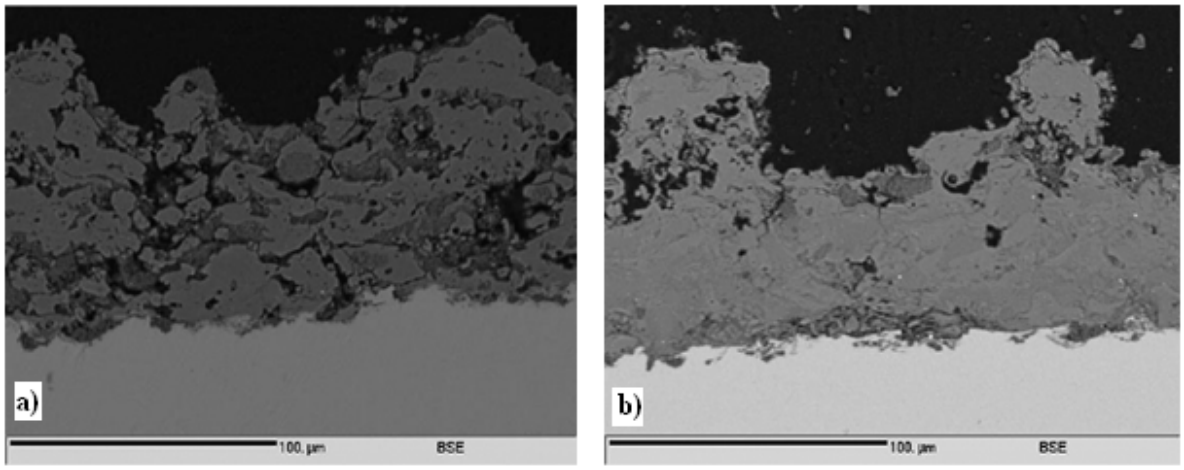

Fig. 4.10. SEM micrographs (back-scattered electrons) of the cross-sections:
as-sprayed sample no. 2 (a) and sample no. 2, soaked in SBF for 60 days (b) [52].

The soaking results in the increase in HA content in the coatings. The phases, which get dissolved at the quickest in SBF are CaO and TTCP. A careful analysis of the phases' evolution on soaking was carried out with the use of X-ray diffraction and Raman spectroscopy and evidenced no amorphous phase in the suspension plasma sprayed coatings [52].

7.2.1.2. TITANIUM DIOXIDE COATINGS

Titanium dioxide coatings were obtained in two series of experiment. One of them, described in this work in “A” part of this chapter, was focused on the influence the type of the injector, and in “B” part of this chapter the coatings produced with continuous-stream injector are described.

A – Titanium dioxide coatings obtained with different injectors

Morphology of TiO_2 coatings was investigated using a JEOL JSM 5800LV scanning electron microscope (SEM) and conducted in polished cross-sections and top surfaces. Variable spray parameters are collected in Tables 7.2 and 7.3. Two systems of suspension injection were used to manufacture the coatings: external atomizing (Fig. 7.12) and the internal continuous-stream injector (Fig. 6.9).

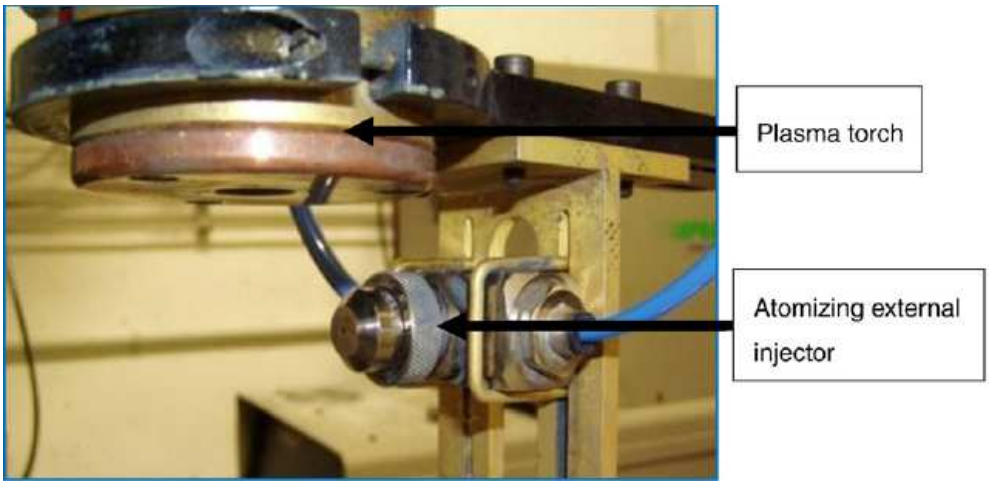

Fig. 7.12. Set up of the suspension injector – external atomizing mode [4.9].

Table 7.2. Variable spray parameters and sample codes of suspension plasma sprayed TiO_2 coatings obtained with atomizing external injection.

Experimental run no.	Suspension feed rate [ml/min]	Spray distance [mm]	Electric power [kW]
T1	20	80	38
T2	40	80	38
T3	20	120	38
T4	40	120	38
T5	20	80	40
T6	40	80	40
T7	20	120	40
T8	40	120	40
T9	30	100	39
T10	30	100	39

Table 7.3. Variable spray parameters and sample codes of suspension plasma sprayed TiO_2 coatings obtained with continuous-stream internal injection.

Experimental run no.	Pressure in the suspension container [MPa]	Solid mass ratio in the suspension [%]	Number of passages in one cycle
S1	0,04	10	10
S2	0,05	20	5
S3	0,04	20	5
S4	0,05	10	10
S5	0,04	10	10
S6	0,04	20	5
S7	0,04	20	10

Figs. 7.13 and 7.14 presented SEM micrographs of TiO_2 coatings obtained with the use of the external and internal injection mode, respectively. Differences in the coatings morphologies depending on different suspension injection systems can be clearly observed. For the coatings sprayed with the internal continuous-stream injector the microstructural examinations revealed two principal characteristics: dense zones with well molten big lamellae and porous zones containing fine nanometric and submicrometric grains. On the other hand, coatings sprayed with the external injection mode are composed of fine particles, which agglomerated and have dimensions of tens of micrometers. In both cases an important porosity is observed.

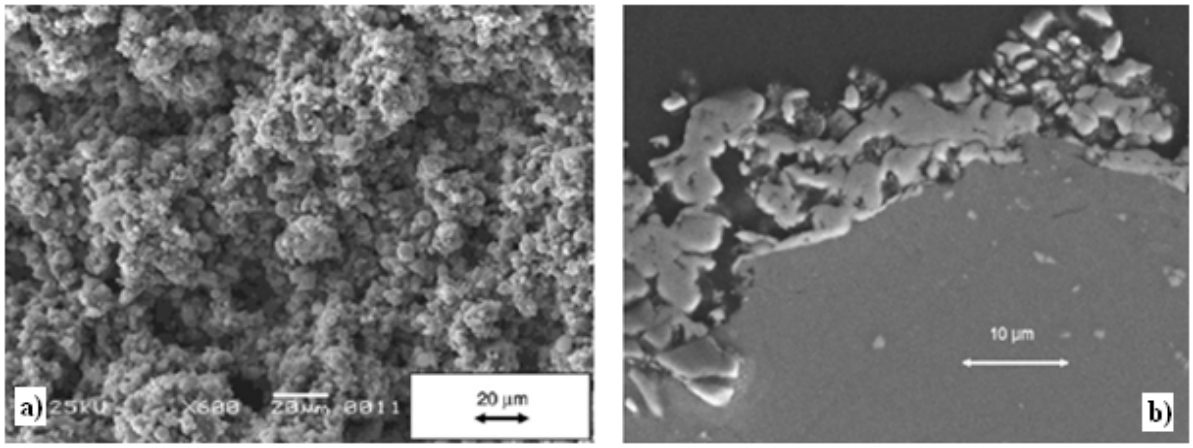

Fig. 7.13. SEM-microstructure of TiO_2 suspension sprayed coatings using the atomizing injector: top surface (a) and cross section (b) [56].

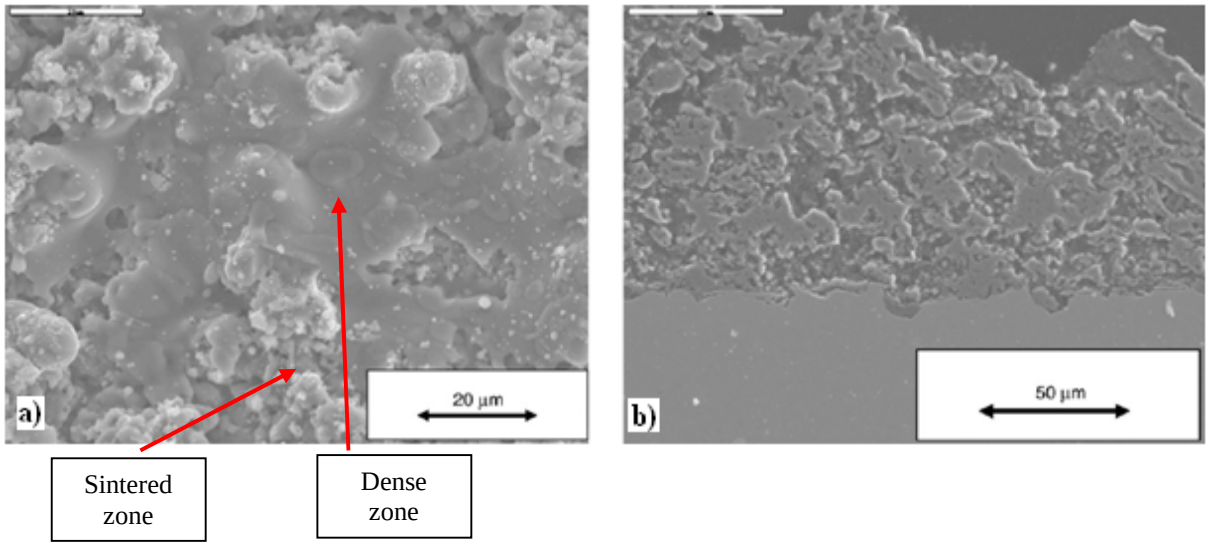

Fig. 7.14. SEM-microstructure of TiO_2 sprayed coatings obtained by internal injection of the suspension: (a) top surface (run no. 2); and (b) cross section [56].

The phase composition was estimated by X-ray diffraction analysis using a *D8-Bruker* apparatus (*Bruker AXS*, Karlsruhe, Germany) with Cu-Kα radiation in the range of 2θ angles from 20^o to 60^o. The patterns were identified using *Diffrac^{plus} Eva* software. The volume percentages of the TiO_2 anatase phase were determined using eq. 6.7. The phase composition of the titania coatings depends strongly on the mode of injection as well as, on the spraying parameters (Fig 7.15).

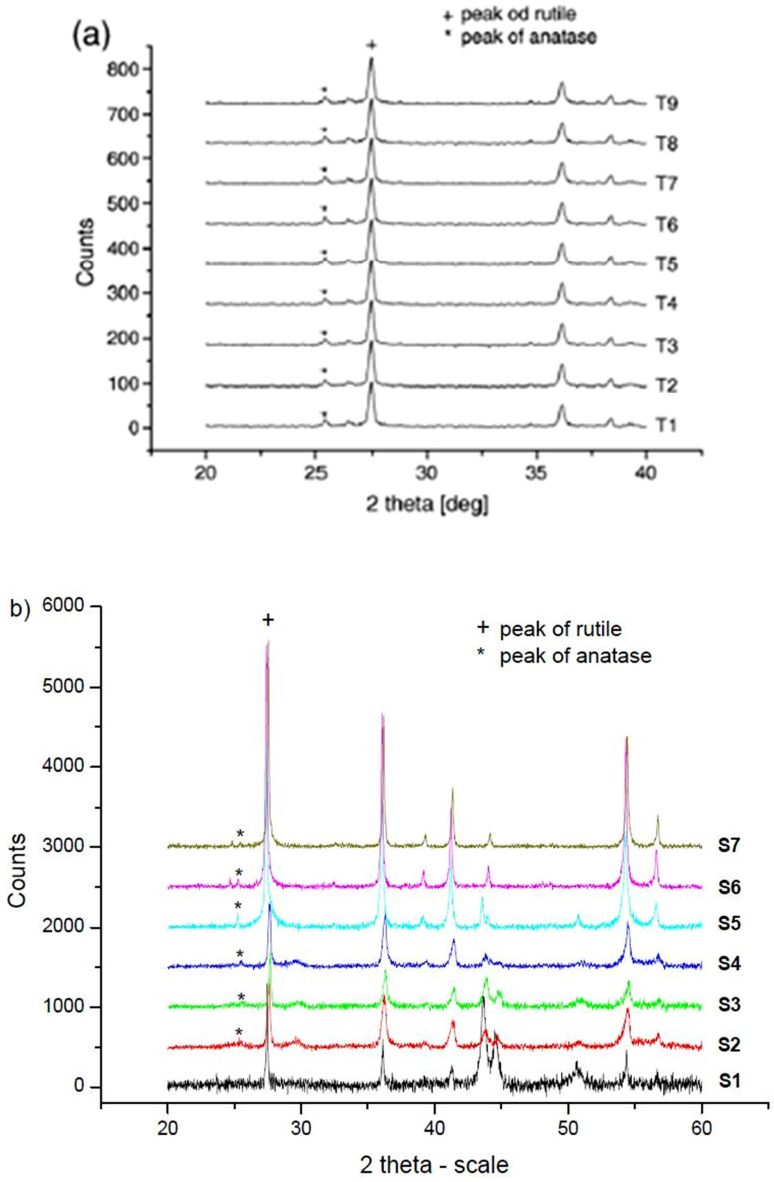

Fig. 7.15. XRD-diffraction diagrams of TiO_2 coatings using different suspension injection systems:
(a) all experimental runs for atomizing injector; and
(b) continuous-stream injector sample sprayed in the experimental run no. 5 [56].

The amount of the anatase phase in the coatings was determined from the X-ray diagrams, using Eq. 6.7 and the obtained values are collected in Table 7.4. A very low content of anatase (from 1.6% to 8.8 vol.%) is present in the coatings sprayed with the use of the internal injector. In some cases (run no. 7), the amount of anatase was about one order of magnitude lower than that determined in the coatings prepared with the external injection. The content of anatase in the coatings sprayed with the use of the external injector was greater and varied from 9.4% to 15.4 vol.%.

Table 7.4. Anatase content in suspension plasma sprayed TiO_2 coatings using different injectors system [56].

Fraction of anatase in samples sprayed using atomizing injector [73], vol.%									
T1	T2	T3	T4	T5	T6	T7	T8	T9	T10
9,4	11,8	13,8	15,3	9,7	9,9	15,4	14,5	13,1	12,1
Fraction of anatase in samples sprayed using internal continuous-stream injector, vol.%									
S1	S2	S3	S4	S5	S6	S7	–	–	–
5,6	8,8	6,6	6,6	5,0	2,3	1,6	–	–	–

B – Titanium dioxide coatings obtained with continuous-stream injector

The coating characterization was conducted on the top surfaces using a scanning electron microscope (SEM) Philips 515. Variable spray parameters are collected in Table 7.5. The SEM micrographs of the top surfaces of the coatings sprayed onto different substrates are shown in Figs. 7.16-7.18. The microstructure of the coatings depended mainly on their deposition temperature.

Table 7.5. Variable spray parameters and sample codes of suspension plasma sprayed TiO_2 coatings obtained on different substrates.

Experimental run	Spray distance [mm]	Linear torch velocity [mm/s]	Range of maximum surface temperature °C		
			Aluminium	Stainless steel	Titanium
1	60	300	300–340	200–290	420–500
2	60	400	250–300	175–350	420–510
3	65	350	275–350	200–320	450–600
4	70	300	275–300	250–350	420–500
5	70	400	275–350	150–275	400–450

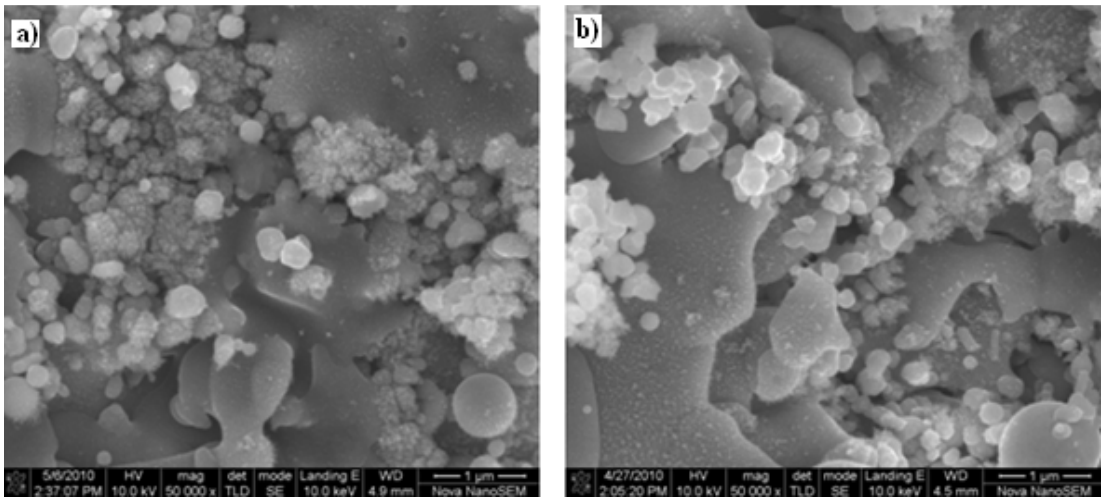

Fig. 7.16. SEM (secondary electrons) micrographs of suspension plasma sprayed TiO_2 coatings sprayed in run no. 1 (a) and run no. 5 (b) on aluminum substrate [75].

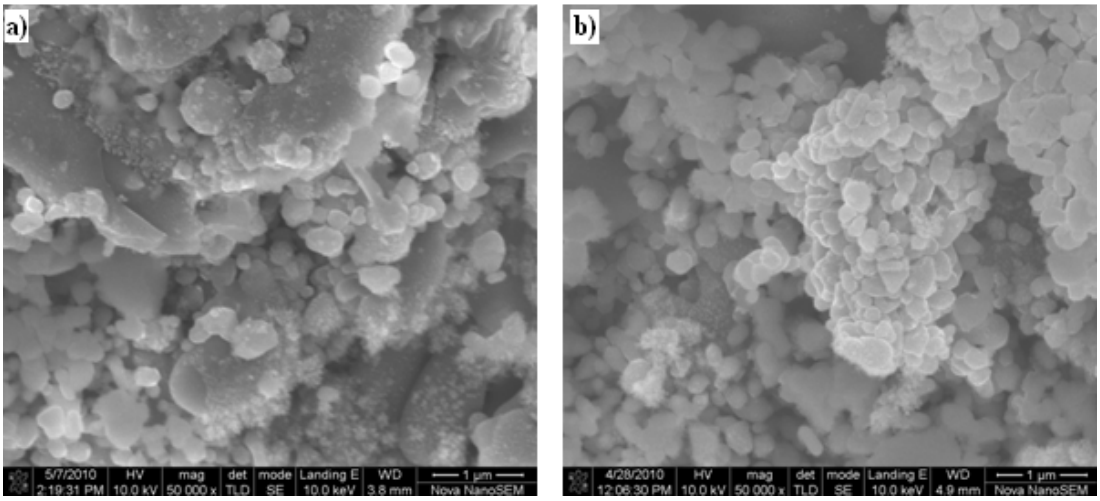

Fig. 7.17. SEM (secondary electrons) micrographs of suspension plasma sprayed TiO_2 coatings sprayed in run no. 1 (a) and run no. 5 (b) on stainless steel substrate [75].

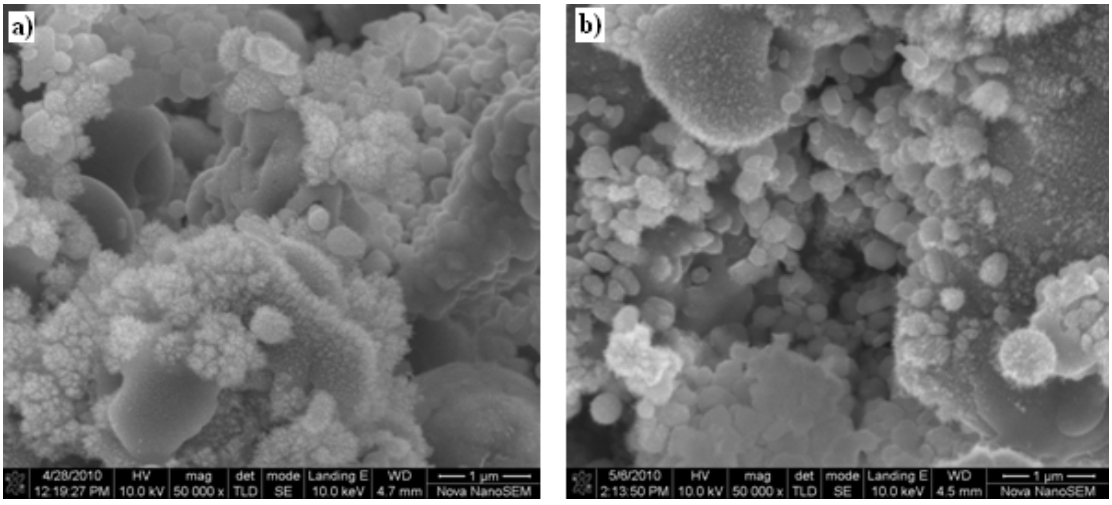

Fig. 7.18. SEM (secondary electrons) micrographs of suspension plasma sprayed TiO_2 coatings sprayed in run no. 1 (a) and run no. 5 (b) on titanium substrate [75].

The morphologies of the coatings sprayed using variable spray parameters were investigated more carefully: for the lowest coatings temperatures in run no. 5 and for the highest coatings temperatures in run no. 1. The coatings sprayed in run no. 1 exhibit more compact microstructure or even the recrystallized grains, as it can be seen in Fig. 7.18a. The coatings sprayed on stainless steel substrate with the lowest coatings temperature were very porous and show hardly molten lamellas.

The phase composition was estimated in the similar method, similarly to the case of titania coatings obtained from different injectors. The contents of the anatase phase, found with the X-ray method are shown in Table 7.6. The anatase contents were lower than 10 vol. %, and the greatest values were determined in the coatings sprayed on Ti substrate (run no. 5) and the lowest values for the coatings were obtained on Al substrate (run no. 1).

Table 7.6. Anatase contents in suspension plasma sprayed TiO_2 coatings on different substrates [74].

Experimental run no.	Fraction of anatase in samples, vol. %		
	Aluminum	Stainless steel	Titanium
1	1.7	5.5	7.0
2	5.8	6.0	5.4
3	6.8	8.6	5.5
4	6.7	6.7	7.7
5	5.3	5.7	9.8

7.2.1.3. COATINGS BASED ON ZIRCONIM OXIDE

Morphology of ZrO_2 + 8 wt.% Y_2O_3 coatings was tested on coatings' cross sections and surfaces using a ZEISS NEON40 field emission scanning electron microscope (SEM). The variable spray parameters are collected in Table 7.7. Both cross sections and the surface of coatings were coated with a carbon film to achieve electrical conduction of the observed surfaces. The coatings have a lamellar structure, similar to that sprayed with coarse feedstock (Fig.7.19a–c).

Table 7.7.Variable spray parameters and sample codes of suspension plasma sprayed 8YSZ coatings.

Experimental run	Spray distance [mm]	Linear torch velocity [mm/s]
1	60	300
2	50	300
3	40	500

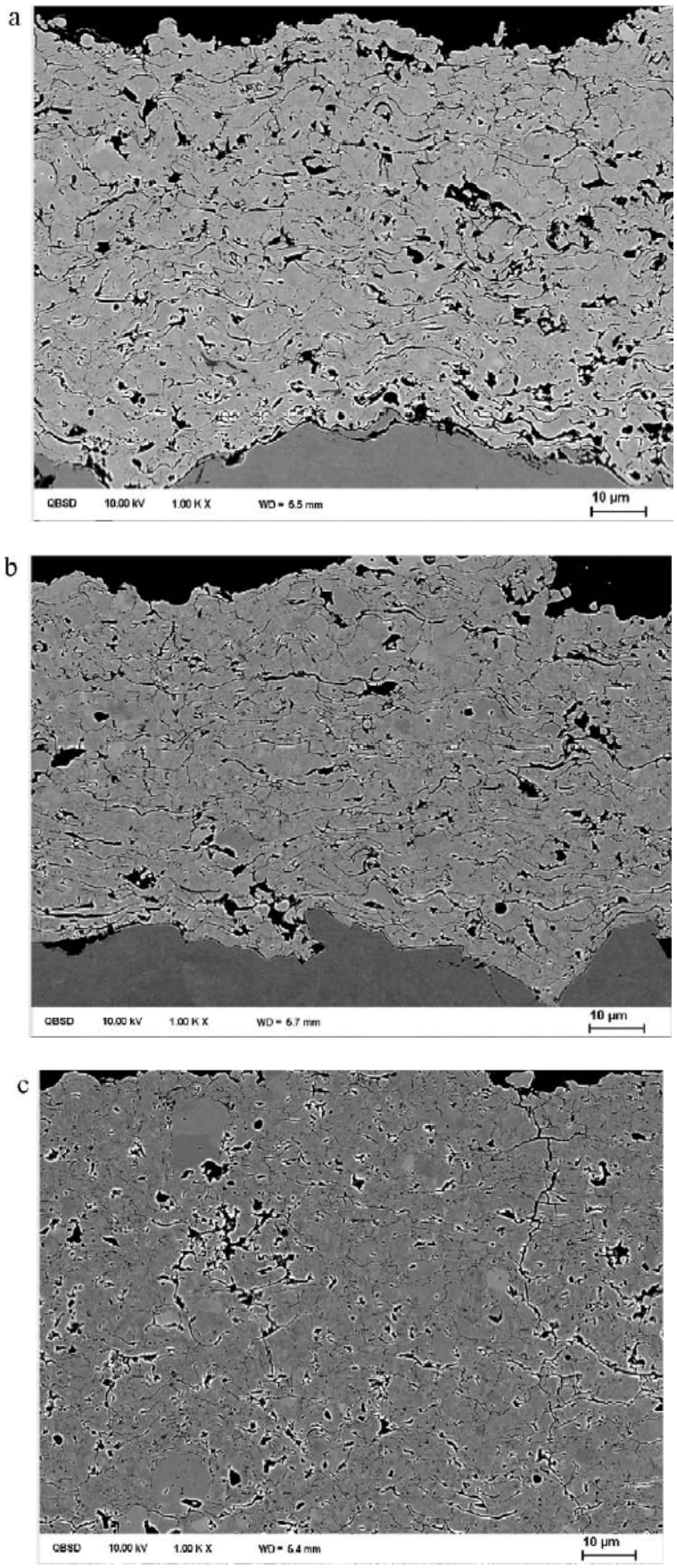

Fig 7.19. SEM micrograph (back-scattered electrons) of the cross-sections of the coatings sprayed in run 1 (a), in run 2 (b), and in run 3 (c) [71].

The samples obtained in the run 3 have some vertical cracks resulting from relaxation of thermal stresses generated at processing associated with an important convective heat input at short spray distance. The lamellar structure could have resulted from the presence of relatively large solid particles in the feedstock (Fig. 7.1). The cracks were not observed in the coatings sprayed in the runs 1 and 2, at the spray distances of 60 and 50 mm. On the other hand, the contacts between the lamellas, inside the coating sprayed in the run 3, are better and close porosity clearly smaller. The crystals inside the lamellas have a columnar or an equiaxed shape in the coatings sprayed in the all experimental runs (Fig. 7.20a–c). The coatings' surface shows *two zones microstructure* with well molten lamellas neighboring the finely grained zones (Fig. 7.21a–c). However, the majority of grains was well molten and the sintered zone is not visible in the coatings' cross-sections.

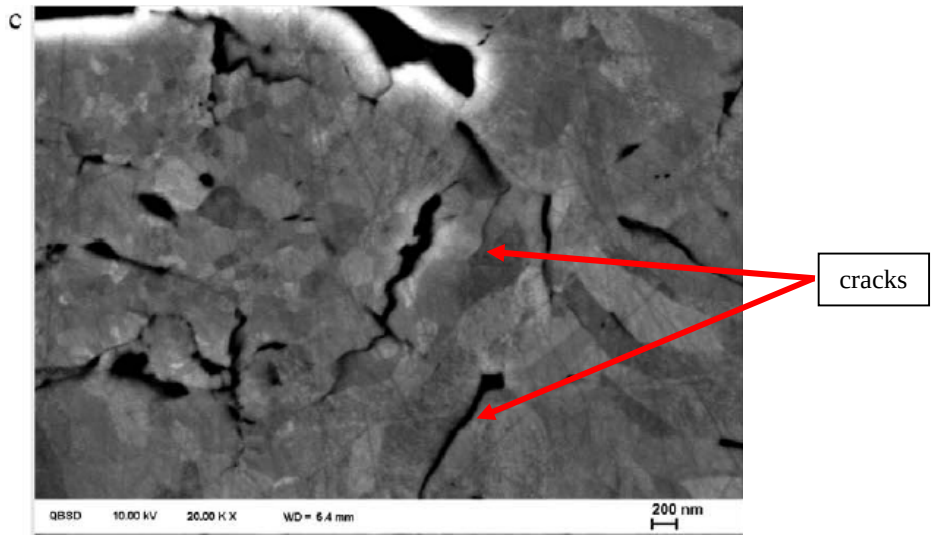

Fig 7.20. SEM micrograph (back-scattered electrons) of the cross-section of lamellas inside the coatings sprayed in run 1 (a), in run 2 (b), and in run 3 (c) [71].

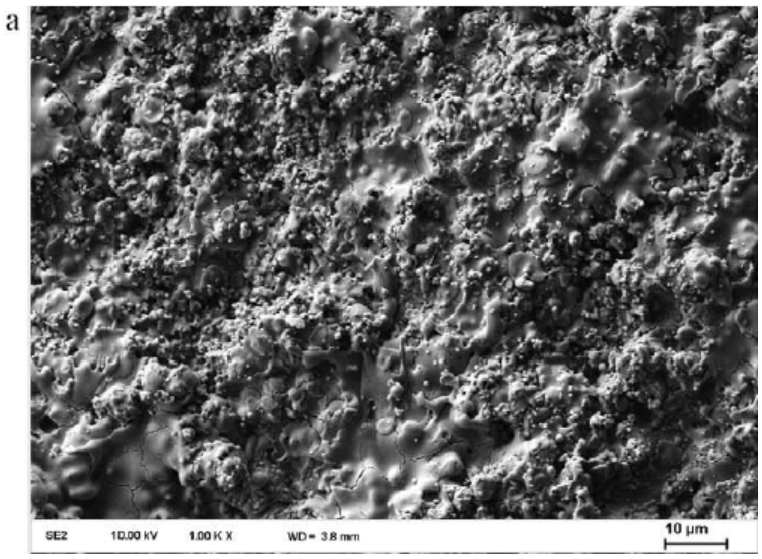

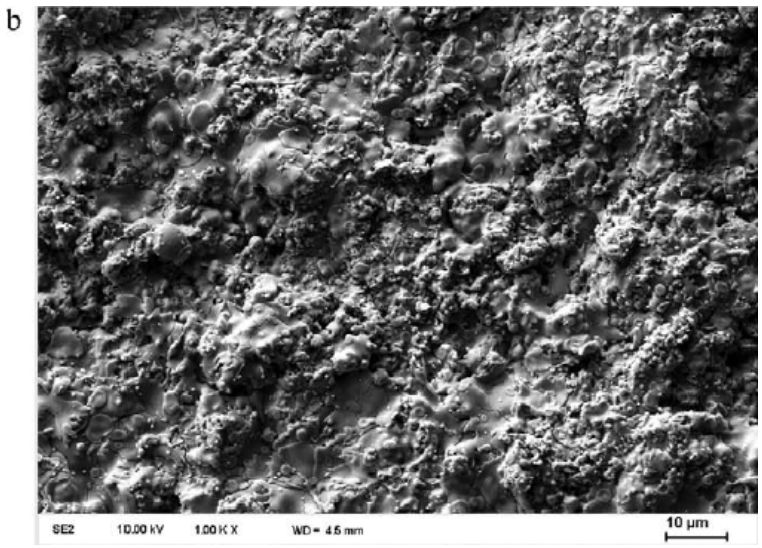

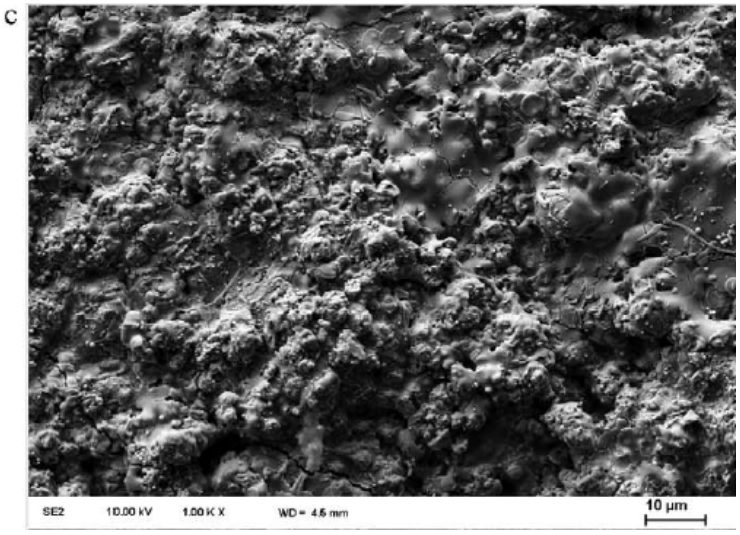

Fig. 7.21. SEM micrograph (secondary electrons) of the surface of coatings sprayed: in run 1 (a), in run 2 (b), and in run 3 (c) [71].

The X-ray diffraction diagram shows that the major phase is tetragonal ZrO_2 with a small quantity (about 4 wt.%) of monoclinic phase as shown in Fig. 7.22.

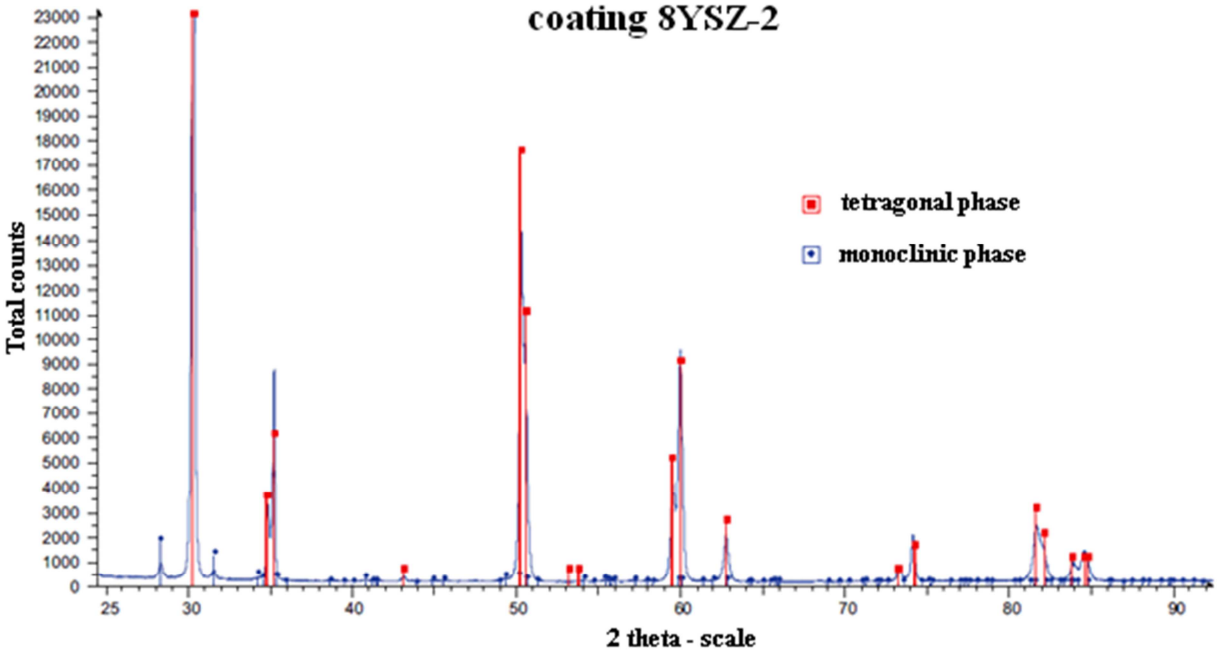

Fig. 7.22. Typical X-ray diagram of the plasma sprayed coating (sample sprayed in run 2) [71].

The phase composition of the initial powder Metco 204 NS was estimated by Ahmaniemi et al. [81] to be about 82 wt.% tetragonal phase and the rest being monoclinic phase. The presence of cubic zirconia, shown in Fig. 7.23, can be excluded because of high angular resolution resulting from purely monochromatic X-ray radiation.

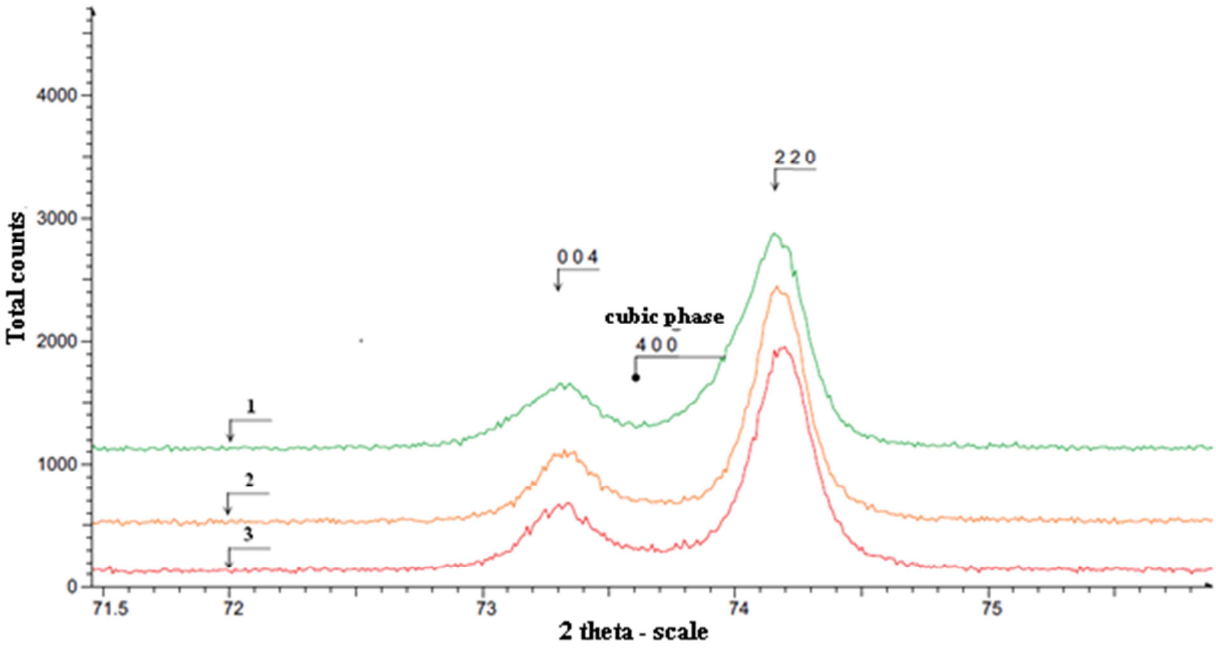

Fig 7.23. The part of X-ray diagram of the samples sprayed in the run 1 (top curve), run 2 (middle curve) and in run 3 (bottom curve) showing the absence of the peak corresponding to the cubic phase [71].

The proportion of both phases and their lattice parameters determined by the *Rietveld* method are reported in Table 7.8. The lattice parameters refined for monoclinic zirconia are not very accurate because of the low content of this phase (about 4 wt.%). The refined lattice parameters for tetragonal zirconia change only very slightly in three tested samples and they are very close to those determined for the deposits obtained using the conventional feedstock obtained by Ahmaniemi et al. [81]. The theoretical content in Y corresponding to these lattice parameters can be estimated to 8 mol.% Y, giving the formula $Y_{0.08}Zr_{0.92}O_{1.96}$ [71].

Table 7.8. Calculation of the content of phases and lattice parameters using *Rietveld* method of zirconia coatings suspension plasma sprayed in different runs [71].

Experimental run	Tetragonal zirconia			Monoclinic zirconia		
	Content, wt.%	*a*, Å	*c*, Å	Content, wt.%	*a*, *b*, Å	c, Å and γ, °
1	96.1	3.6158	5.1620	3.9	5.182 5.223	5.282 99.10°
2	96.5	3.6158	5.1625	3.5	5.180 5.199	5.314 99.13°
3	95.6	3.6165	5.1651	4.4	5.180 5.204	5.312 99.08°

Because of the big grain size distribution, powder 8YSZ was milled with the modified parameters. The change results in the narrower and monomodal grain size distribution. The morphology of obtained ceramic coatings, 8YSZ and 24CeYSZ, was characterized with the scanning electron microscope Philips 515 with use of secondary electrons detectors. Micrographs were made on the top of surfaces and on the cross-section of the coatings. The surface of the suspension plasma 8YSZ coatings shows generally fine grains having a spherical form and well molten large lamellae (Figs. 7.24a-7.26a). The cross section shows relatively well molten lamellae and some porosity between them (Figs. 7.24b-7.26b). It is possible to distinguish the small grains inside the lamellae. Some of them have vertical cracks, which could have been generated by relaxation of thermal stress after deposition. In case of 24CeYSZ coatings, the surface shows less well molten lamellae than the 8YSZ coatings and greater fine, spherical particles (Fig. 7.27a-7.29a). The cross-sections of 24CeYSZ coatings (Fig. 7.27b-7.29b) show greater porosity and revealed higher number of cracks than 8YSZ ones.

Table 7.9. Variable spray parameters and sample codes of suspension plasma sprayed 8YSZ and 24CeYSZ coatings.

Experimental run	Spray distance [mm]	Linear torch velocity [mm/s]
1	40	300
2	40	500
3	50	400
4	60	300
5	60	500

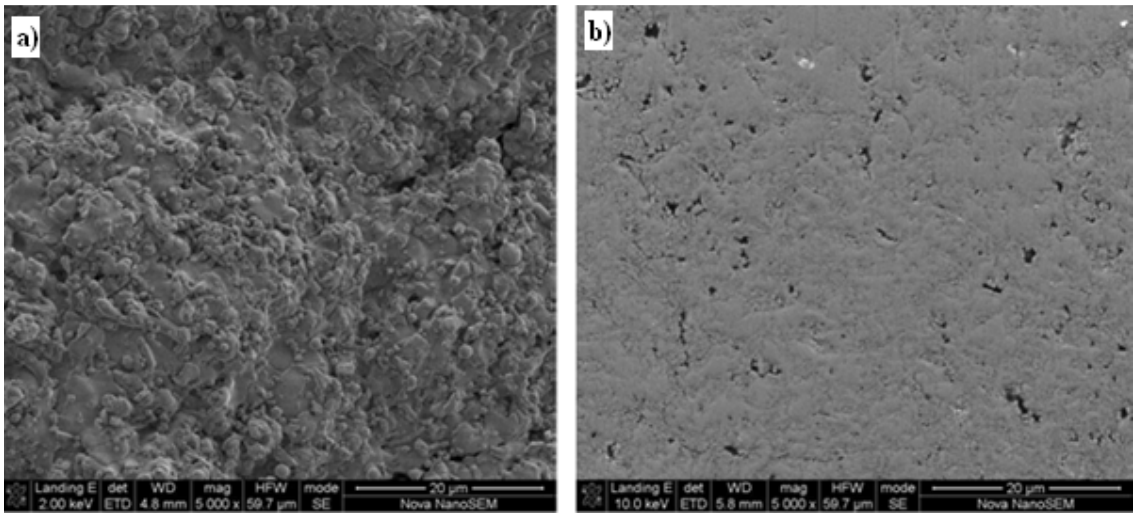

Fig. 7.24. SEM (secondary electrons) of 8YSZ coating sprayed in run 1: (a) surface, (b) cross-section.

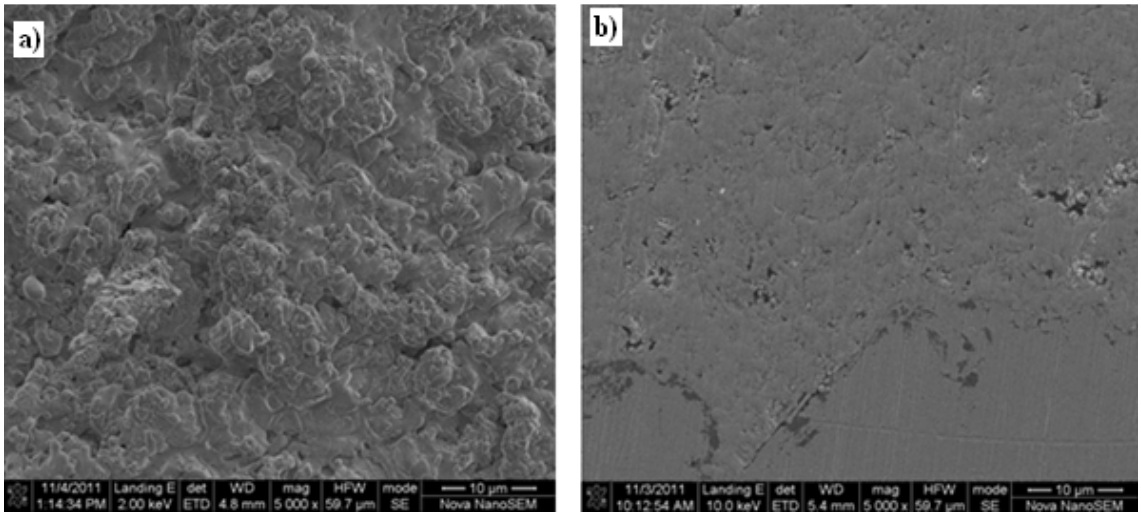

Fig. 7.25. SEM (secondary electrons) of 8YSZ coating sprayed in run 3: (a) surface, (b) cross-section [4.11].

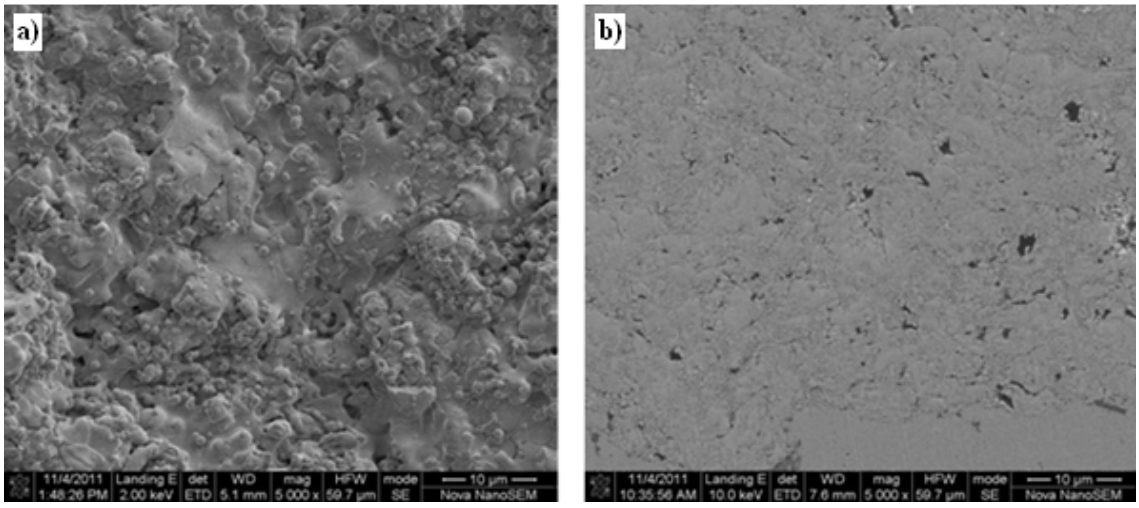

Fig. 7.26. SEM (secondary electrons) of 8YSZ coating sprayed in run 5: (a) surface, (b) cross-section.

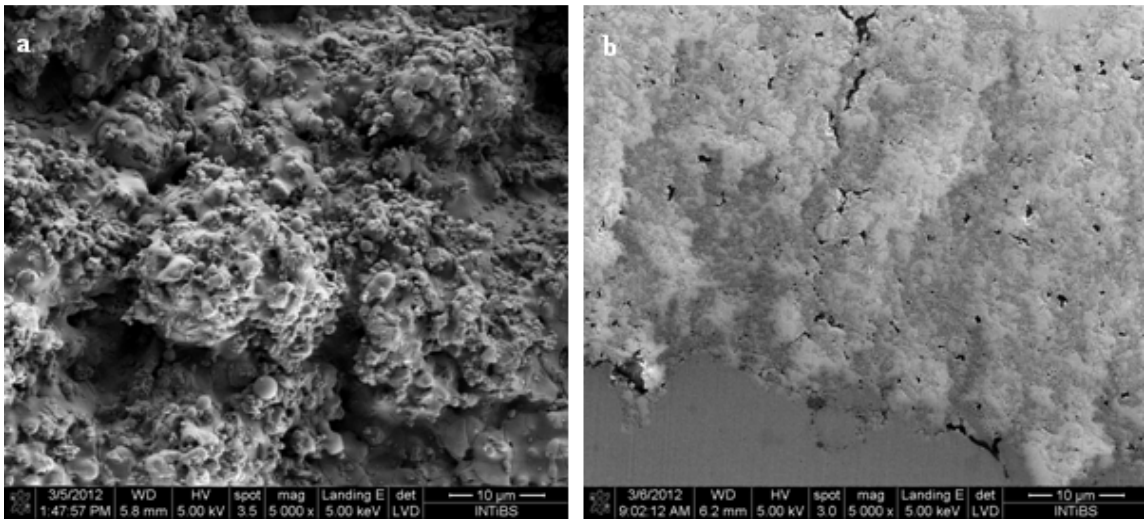

Fig. 7.27. SEM (secondary electrons) of 24CeYSZ coating sprayed in run 1: (a) surface, (b) cross-section.

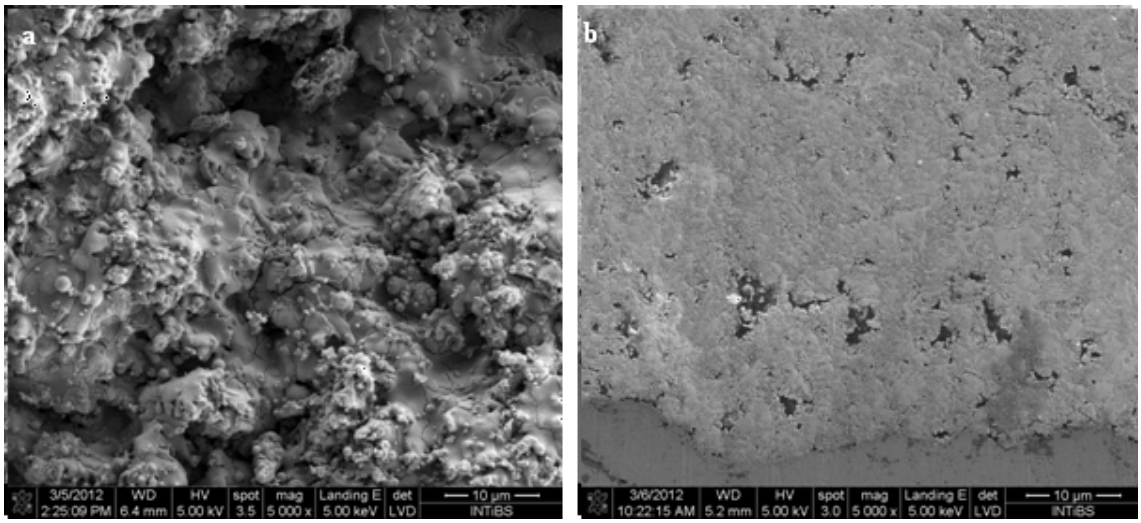

Fig. 7.28. SEM (secondary electrons) of 24CeYSZ coating sprayed in run 3: (a) surface, (b) cross-section.

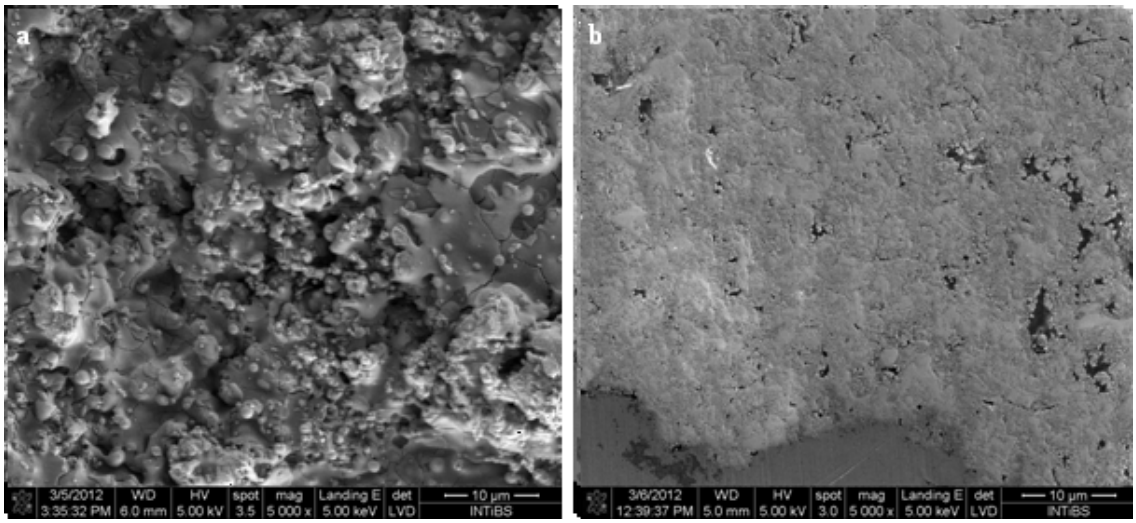

Fig. 7.29. SEM (secondary electrons) of 24CeYSZ coating sprayed in run 5: (a) surface, (b) cross-section.

Determination of the phase composition was made in a similar way, as in the previous case. A typical X-ray diffraction diagram is presented in Fig. 7.30.

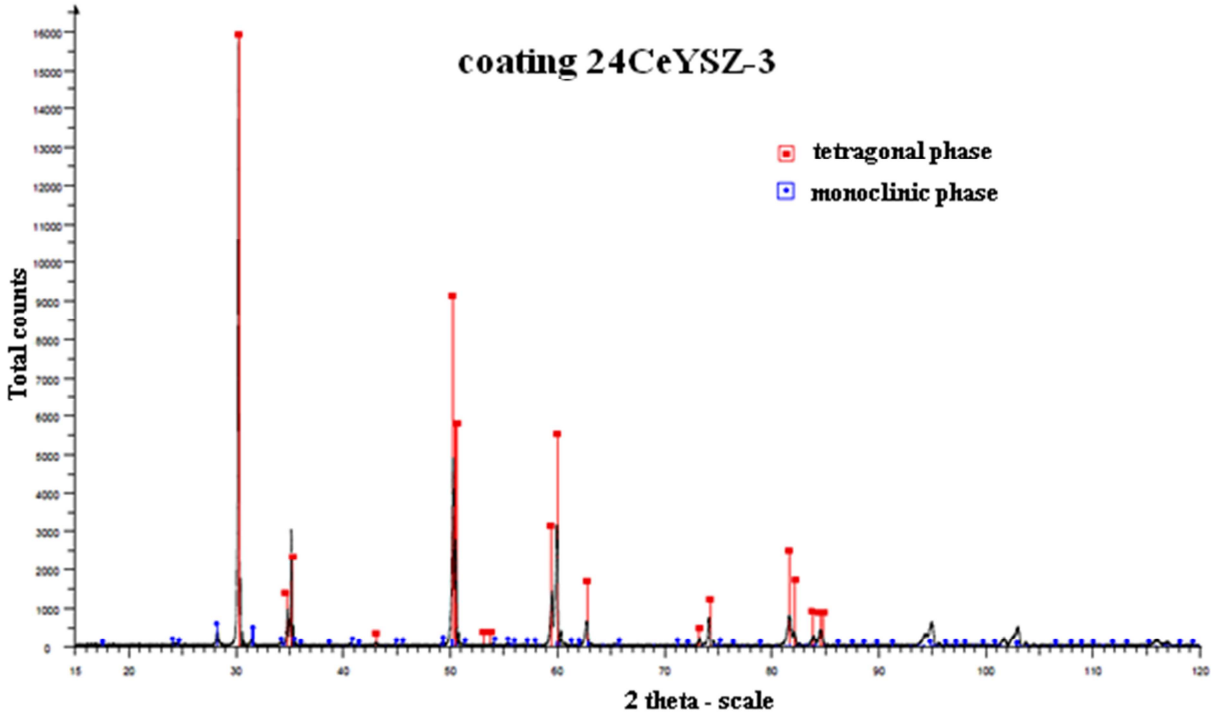

Fig. 4.29. Typical X-ray diagram of the plasma sprayed coating (sample sprayed in run 3).

All X-ray diffraction diagrams show that the major phase is tetragonal ZrO_2 with a quite small quantity, below 11 wt.% or below 5 wt.% of monoclinic phase, for 8YSZ and 24CeYSZ coatings, respectively. The proportion of both phases and their lattice parameters determined by the *Rietveld* method are reported in Tables 7.10 and 7.11. The refined lattice parameters for tetragonal zirconia change in quite a small range for all the tested samples.

Table 7.10. Calculation of the content of phases and lattice parameters using *Rietveld* method of 8YSZ coatings suspension plasma sprayed in different runs.

Sample	Tetragonal zirconia			Monoclinic zirconia		
	content, wt.%	*a*, Å	*c*, Å	content, wt. %	*a*, *b*, Å	*c*, Å and *γ*, °
8YSZ-1	89.2	3.6147	5.1650	10.8	5.172 5.206	5.319 99.12
8YSZ-2	90.4	3.6144	5.1657	9.6	5.171 5.204	5.318 99.11
8YSZ-3	91.6	3.6157	5.1634	8.4	5.167 5.207	5.318 99.15
8YSZ-4	92.6	3.6159	5.1630	7.4	5.168 5.207	5.318 99.16
8YSZ-5	92.9	3.6159	5.1629	7.1	5.170 5.204	5.318 99.13

Table 7.11. Calculation of the content of phases and lattice parameters using *Rietveld* method of 24CeYSZ coatings suspension plasma sprayed in different runs.

Sample	Tetragonal zirconia			Monoclinic zirconia		
	content, wt.%	*a*, Å	*c*, Å	content, wt. %	*a*, *b*, Å	*c*, Å; *γ*, °
24CeYSZ-1	95.0	3.6406	5.2172	5.0	5.161 5.246	5.284 99.04
24CeYSZ-2	96.1	3.6403	5.2168	3.9	5.150 5.256	5.281 99.06
24CeYSZ-3	95.9	3.6382	5.2159	4.1	5.155 5.209	5.333 99.14
24CeYSZ-4	95.4	3.6404	5.2176	4.6	5.172 5.251	5.280 99.03
24CeYSZ-5	95.9	3.6402	5.2166	4.1	5.162 5.261	5.279 99.06

7.2.2. MECHANICAL PROPERTIES

Mechanical properties of the obtained suspension plasma sprayed coatings were estimated with the method described in chapters no. 3 and no. 6. There were two: (i) microindentation, which makes determination of hardness and elastic modulus of the coatings possible and (ii) scratch test, which characterizes adhesion coatings to the substrates and cohesion in coatings. Adhesion and cohesion were determined using a CSM+ device, presented in Fig. 6.15, whereas hardness and bulk modulus were determined using a microhardness tester CSM 2-107 with Vickers indenter, which is presented in Fig. 6.17.

7.2.2.1. HYDROXYAPATITE COATINGS

The adhesion of the soaked coatings to the substrate was characterized by a critical load. All the values are presented in Fig 7.31. As it can be seen, the values of critical loads, describing adhesion of the coatings to the titanium substrate are roughly between 11 N and 6 N for experiment no. 1. The values, for run no. 2, are between 12 N and 9 N and their decrease is more monotonic.

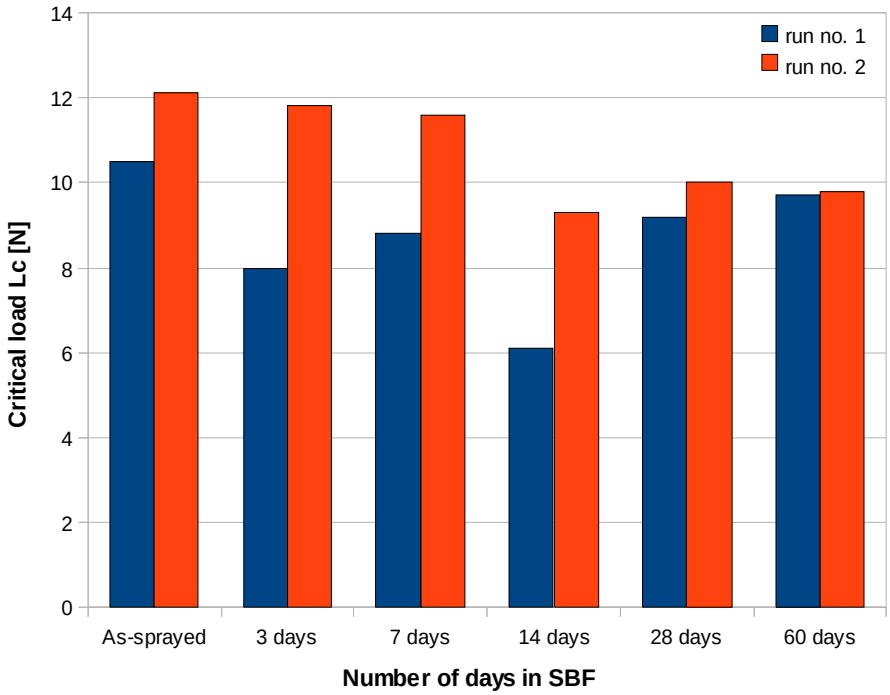

Fig. 7.31. Critical load of suspension plasma sprayed HA coatings vs. duration of soaking in SBF for samples sprayed in the experimental run no. 1 and run no. 2 [52].

The minimal critical load is in both cases after 14 days of soaking, which could have been correlated with the increase of coating porosity resulting from dissolution on the *sintered*

zone. This porosity could have been filled by the products of reprecipitation after longer soaking. The scratch hardness remained fairly constant for the samples sprayed in both experimental runs, Fig 7.32. As the coating thickness was varying from 50 to 100 μm, this hardness, measured on the surface of the deposits, could have been influenced by the hardness of the titanium substrate. Consequently, the modification of the mechanical properties by the soaking in SBF did not influence the values of scratch hardness. The samples sprayed in the run no. 2 were slightly harder than those sprayed in the run no. 1. [52].

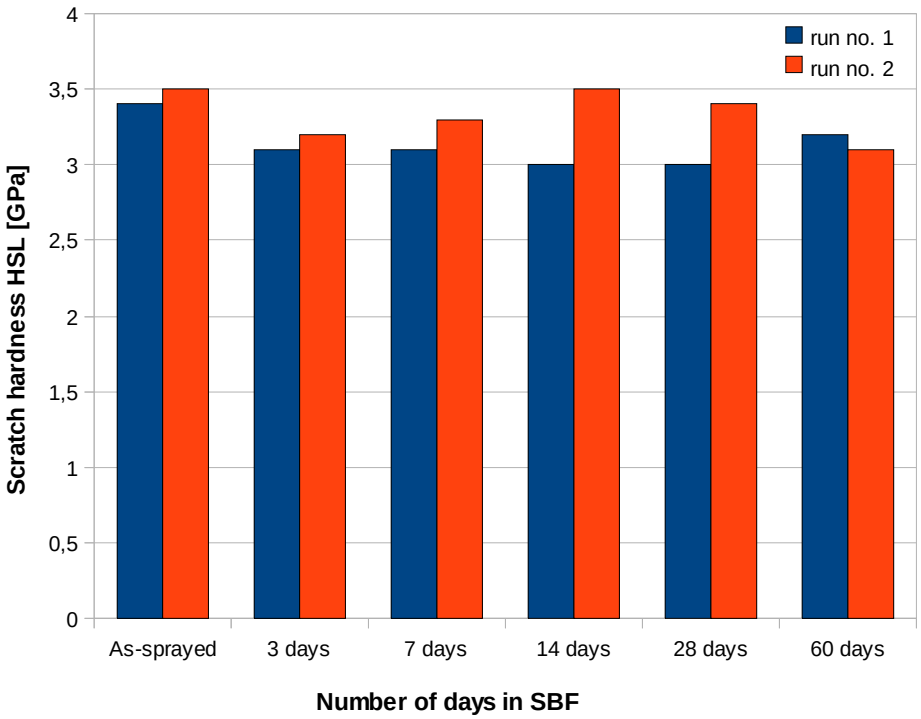

Fig. 7.32. Scratch hardness of suspension plasma sprayed HA coatings vs. duration of soaking in SBF for samples sprayed in the experimental run no. 1 and run no. 2 [52].

The indentation test determined elastic modulus and hardness of investigated coatings. During the indentation tests two types of curves were obtained, with monotonic loading part of curve (Fig 7.33a) or with some changes during the loading (Fig. 7.33b). These changes correspond to an increase in depth for a small increase in load. That can result from the presence of the zones of very different hardness, which may, correspond to the dense and sintered zone shown in Figs 7.10 and 7.11. Independently of this phenomenon the elastic modulus was calculated first and then hardness of the coatings [52].

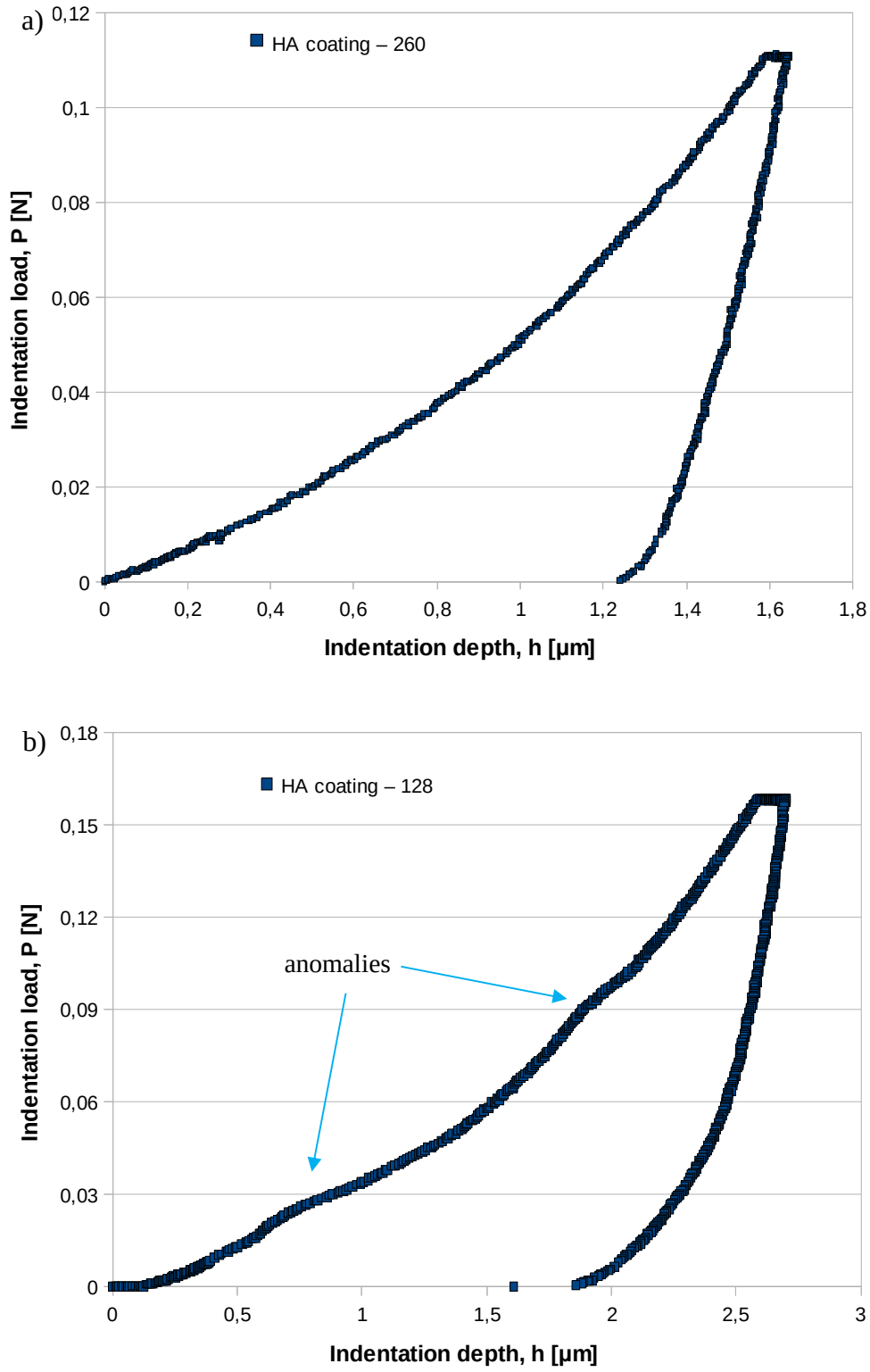

Fig. 7.33. Two types of indentation curves observed in the indentation tests performed on suspension plasma sprayed HA coating soaked in SBF: (a) sample no. 2 after 60 days; and (b) sample no. 1 after 28 days [52].

Fig. 7.34 presents the inverse of the unloading slope, $1/S$, as a function of the inverse of the contact indentation depth $1/h_c$, determined with the use of Eq. 3.2. It can be seen that

the anomalies observed in Fig. 7.33b during loading have no influence on the unloading used for the elastic modulus calculation. The slope was used to calculate the elastic modulus of the material by combining Eqs. 3.21 and 3.22.

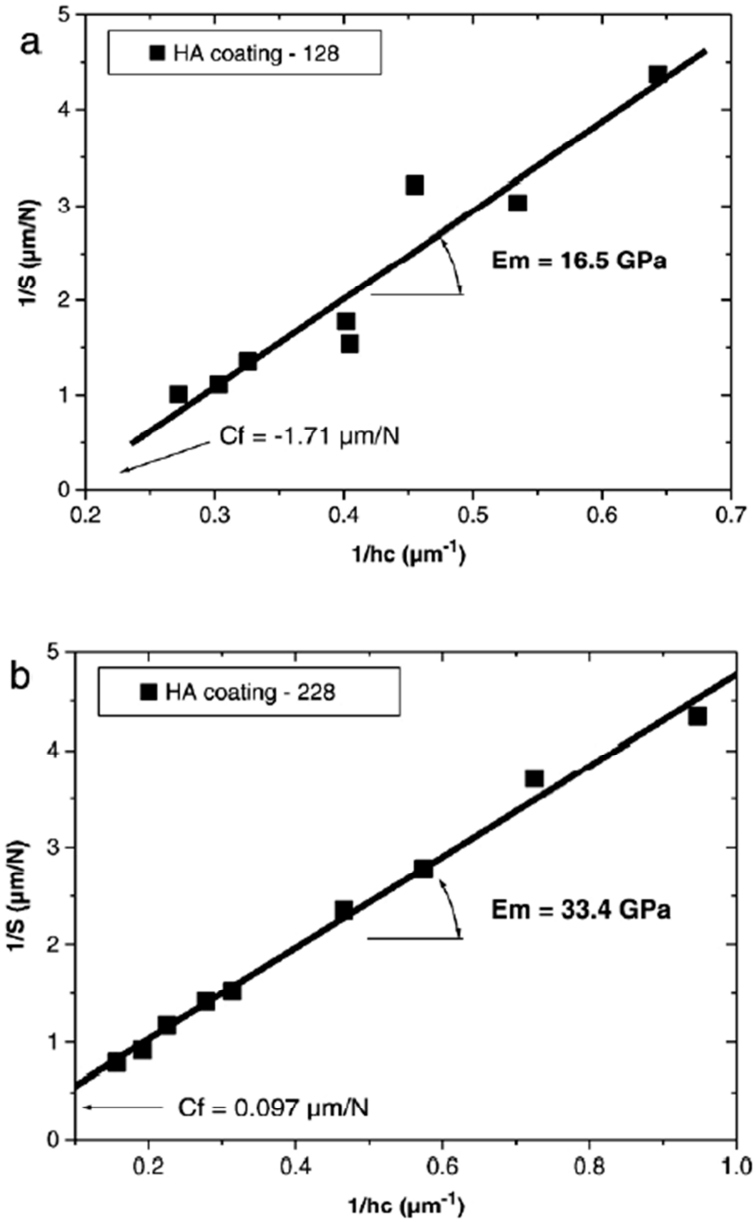

Fig. 7.34. Inverse of the unloading slope as a function of the inverse of the indentation depth, determined with the use of Eq. 3.2, for samples sprayed in two different experimental runs and soaked in SBF for the same duration of 28 days: (a) sample no. 1; and (b) sample no. 2 [52].

The elastic modulus for all tested samples is shown in Fig 7.35. As it can be seen on this figure, the time of soaking in the simulated body fluid has no influence on the elastic modulus of the HA coatings. Therefore a mean value of the elastic modulus was calculated,

according to the different experimental runs. For the spraying distance of 50 mm corresponding to the experimental run no. 2, the elastic modulus is equal to E_m = 28 GPa being about twice of the mean value for the elastic modulus for the samples sprayed using the distance of 60 mm corresponding to the experimental run no. 1, which is only E_m = 16 GPa [52].

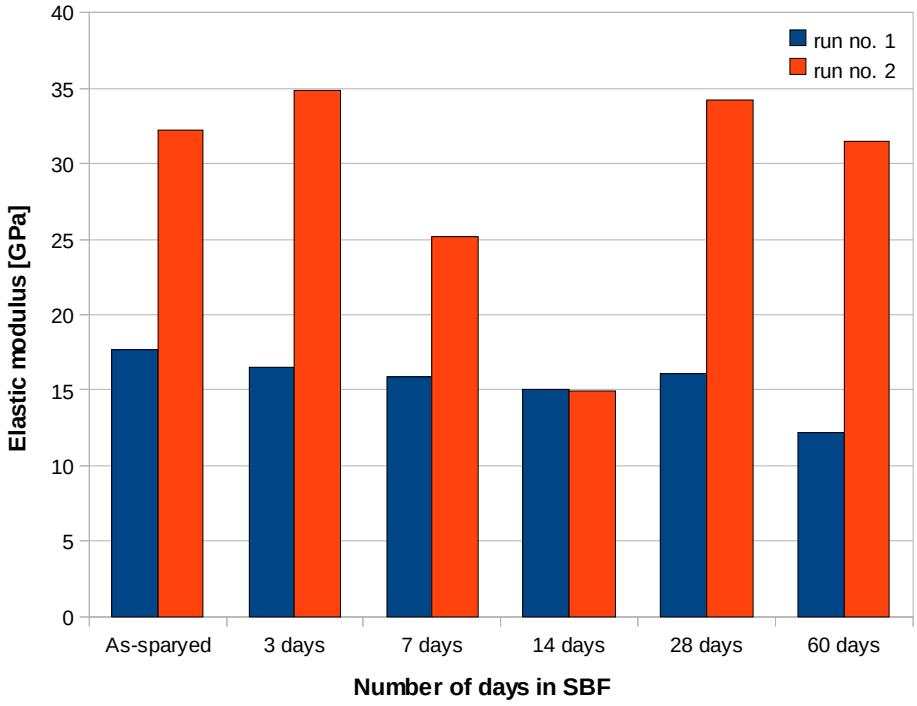

Fig. 7.35. Elastic modulus of suspension plasma sprayed HA coatings vs. duration of soaking in SBF [52].

Fig. 7.36a and 7.36b represent respectively the Martens macrohardness and the Hardness length-scale factor, according to Eq. 3.10, as a function of the number of soaking days in simulated body fluid for the two experimental runs corresponding to different spraying distances. It can be seen that the two parameters clearly increase as a function of the number of days indicating a general increase of the HA coating hardness.

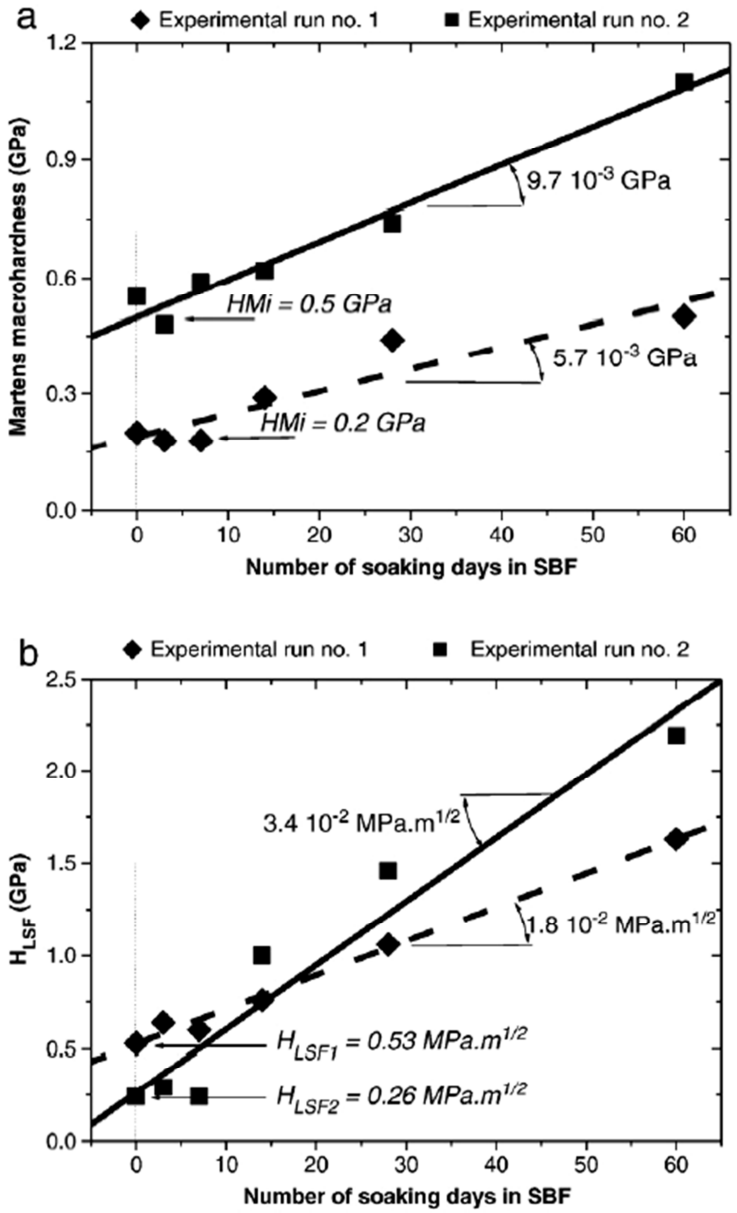

Fig. 7.36. Martens hardness (a); and hardness length-scale factor (b)
of suspension plasma sprayed HA coatings vs. duration of soaking in SBF [52].

7.2.2.2. TITANIUM DIOXIDE COATINGS

Mechanical properties of titania coatings were determined by the scratch test. There were adhesion and cohesion examinations, characterized by critical load and scratch hardness, respectively.

The scratch hardness, shown in Fig. 7.37, depends mainly on the substrate and does not depend on the spray parameters used in the experiments. The hardness of the coatings sprayed onto aluminium substrates was found to be about two times greater, i.e. between 0.6 and 0.7 GPa for the coatings of the same suspension but injected using an atomizer [67].

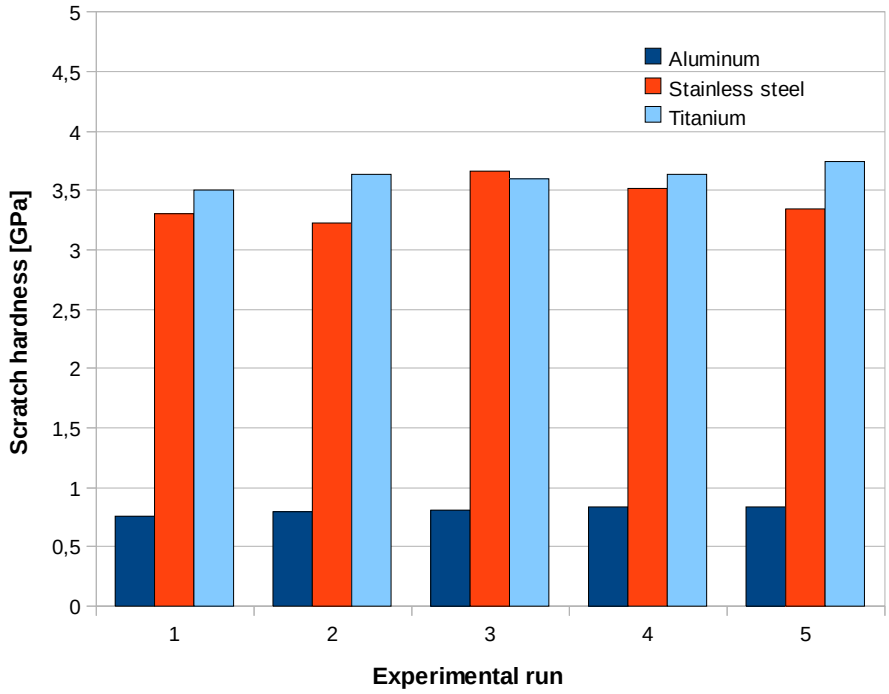

Fig. 7.37. Scratch hardness of TiO_2 coatings suspension plasma sprayed onto different substrates vs. spray runs [82].

The measurements of the critical load could have been carried out only for the coatings sprayed onto aluminum substrates (Fig. 7.38). The coatings sprayed onto other substrates had the critical load greater than 30 N. The critical load was slightly greater than that measured for TiO_2 coatings sprayed on the aluminum substrates with the use of the atomizer being in the range of 10 – 16 N [68]. However, the present coatings were about 50 µm thick being readily thicker than those sprayed with the use of the atomizer.

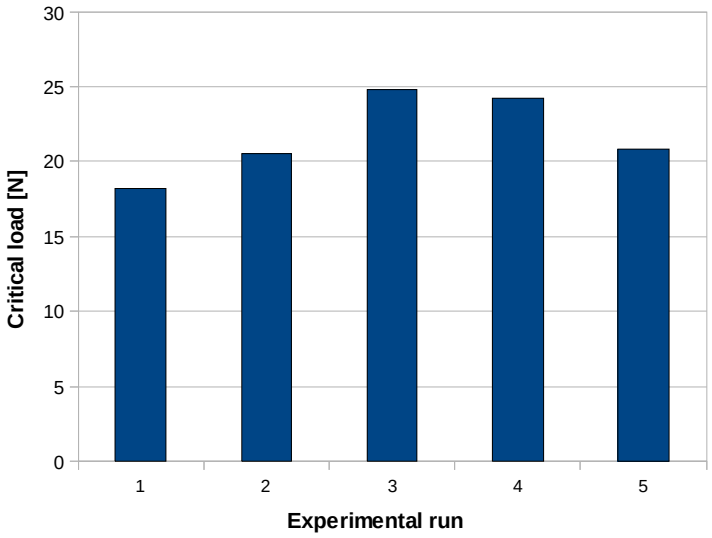

Fig 7.38. Critical load of TiO_2 coatings suspension plasma sprayed onto aluminum substrates vs. spray runs [4.14].

7.2.2.3. COATINGS BASED ON ZIRCONIUM OXIDE

Mechanical properties of ZrO_2 + 8 wt.% Y_2O_3 coatings were tested by the scratch test to estimate adhesion and cohesion. Also IIT was used to determine coatings' elastic modulus and hardness.

Firstly, coatings sprayed from 8YSZ powder with the big grain size distribution were tested. Two samples were tested for each experimental run and three scratches were made on each sample. The penetration depth was measured at the load at 24 N. The scratch hardness, HS_L was measured at the load 30 N. The results of the scratch test are collected in Table 7.12.

Table 7.12. Results of the scratch test in which the parameters are mean values of three measurements with the standard deviation of the measurements [71].

Experimental run	Sample	Penetration depth at force of 24 N, μm	Critical force, L_C, N	Scratch hardness, HS_L, GPa
1	1	25.5 ± 4.6	Greater than 30 N	4.8 ± 0.3
	2	49.3 ± 4.7	8.5 ± 0.6	0.51 ± 0.02
2	1	17.4 ± 1.4	–	–
	2	35.3 ± 1.8	–	–
3	1	15.4 ± 1.1	Greater than 30 N	4.1 ± 0.5
	2	54.5 ± 5.2	10.7 ± 1.1	0.63 ± 0.04

The results show that the samples sprayed in the same experimental runs are very different. Some of them are harder than 4 GPa and the critical force is greater than 30 N. The others have the hardness as low as 0.5 GPa and the critical force is close to 10 N [71].

Due to the big and bimodal grain size distribution, milling parameters were changed and a dispersant agent was added in next step. Then another suspensions were prepared, based on powders, which had a narrower and monomodal grain size distribution and new coatings 8YSZ and 24CeYSZ were sprayed.

Both types of coatings were too thick to carry out the measurement of the critical load and their scratch hardness was only characterized, which is presented in Fig. 7.39.

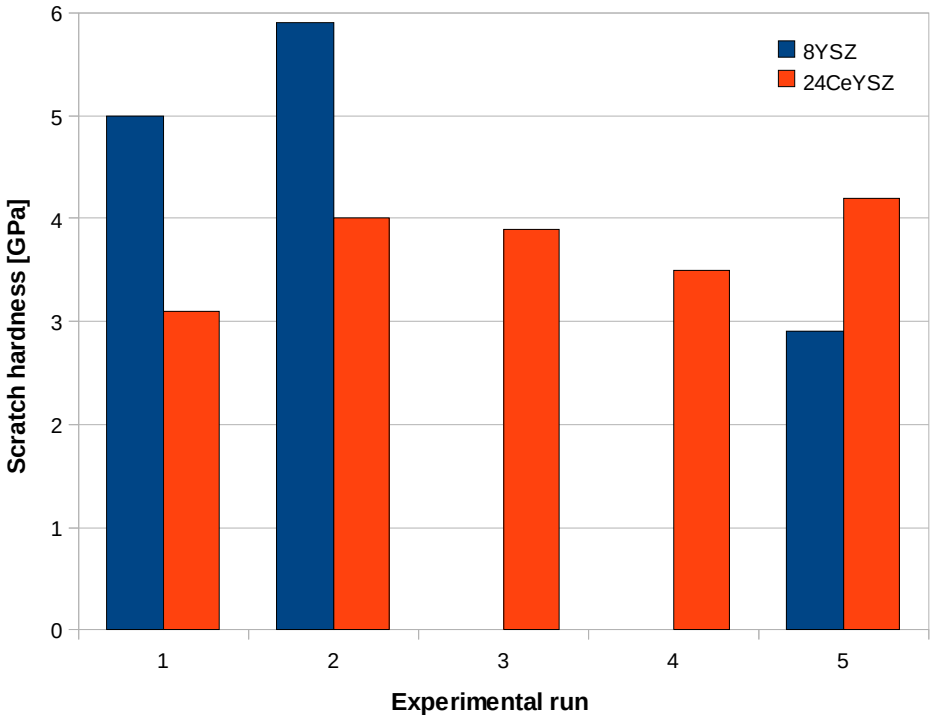

Fig. 7.39. Scratch hardness of suspension plasma sprayed zirconia coatings [78].

The scratch hardness varies between 3 and 6 GPa for all samples. The hardness for 8YSZ is greater for the samples sprayed in run 1 and 2 than these sprayed in run 5. This could have been related to the deposition temperature which is much higher in the runs 1 and 2 than in the run 5. On the other hand this could be the result of the spray distance, which is shorter (40 mm) in the runs 1 and 2 than in the run 5 (60 mm). The hardness of 24CeYSZ samples varies between 3 and 4 GPa for all the experimental runs and it is not correlated with the spray distance, as 8YSZ coatings [78].

In the next step Instrumented Indentation Test was used to determine elastic modulus and hardness of the coatings. The elastic modulus of the sprayed samples is shown in Fig. 7.40. The modulus of 24CeYSZ coatings for short spray distances reached more than 100 GPa. The modulus of 8YSZ coatings depends heavily on the spray distance. It is higher for the shorter spray distance, with the exception of the run 1, which is probably caused by the highest values of deposition temperatures, which result in some cracks.

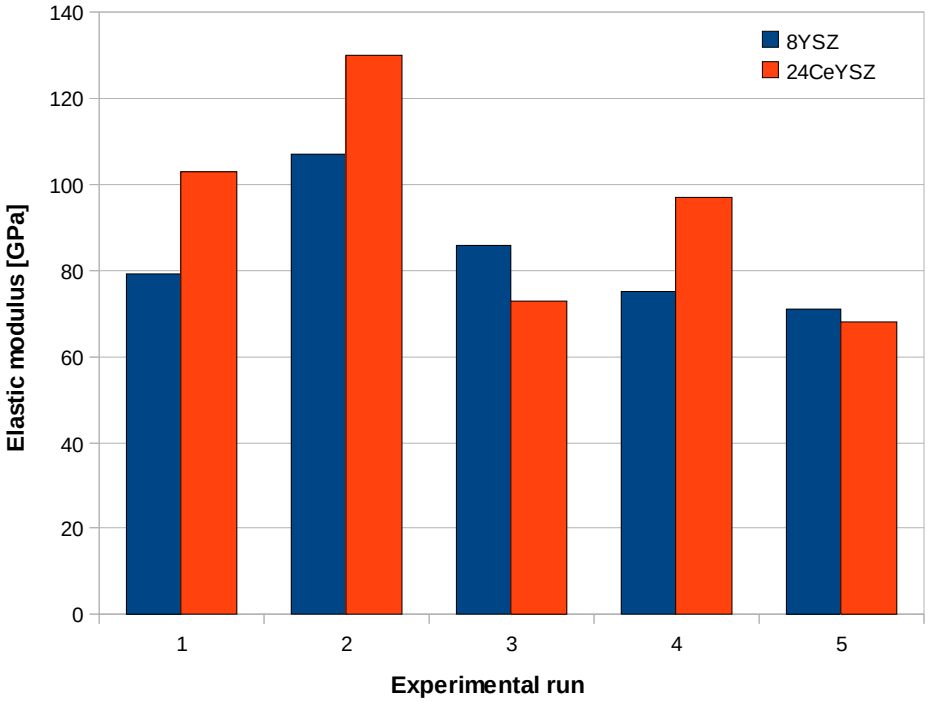

Fig. 7.40. Elastic modulus of suspension plasma sprayed zirconia coatings [78].

The mean values of Martens macrohardness, HM_0, obtained from the indentation tests, for the sprayed coatings are shown in Fig. 7.41. In case of 8YSZ coatings there is a tendency of decreasing of the hardness value with increasing the spray distance. The other spray parameter, the velocity of the torch, has not any influence on HM_0. As far as the 24CeYSZ samples are concerned, both spray parameters influence the macrohardness. In fact, HM_0 decreases with the increasing the torch velocity and increasing the spray distance.

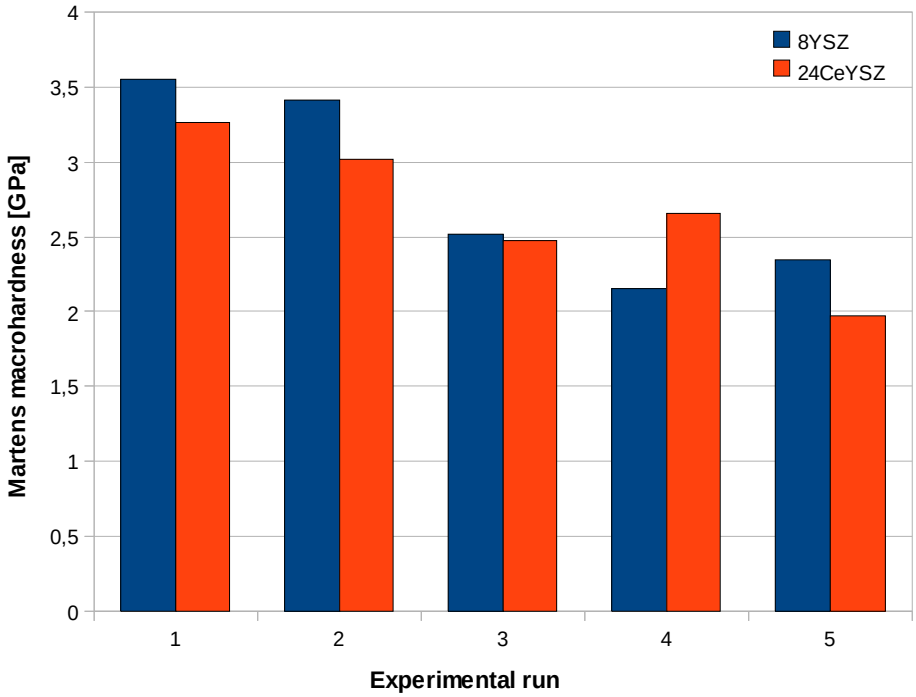

Fig. 7.41. Martens macrohardness of suspension plasma sprayed zirconia coatings [78].

7.2.3. THERMAL TRANSPORT PROPERTIES

The thermal transport and thermophysical properties of the ceramic coatings are very important because of their applications as thermal barrier coatings, *TBC* in gas turbines in aviation industry. They concern thermal diffusivity, conductivity and thermal expansion. These properties were determined for yttria stabilized zirconia and yttria with ceria stabilized zirconia coatings.

The thermal diffusivity of ZrO_2 + 8 wt.%Y_2O_3 coatings, for preliminary studies, have been made by F. Cernuschi, with a non-destructive method, single side thermographic technique, described in chapter no. 2. For each sample, the measurements have been repeated ten times. Then experimental surface temperature, was plotted versus the time and the next step was fitting a curve, which was used to determine the thermal diffusivity of the coatings. An example is presented in Fig. 7.42.

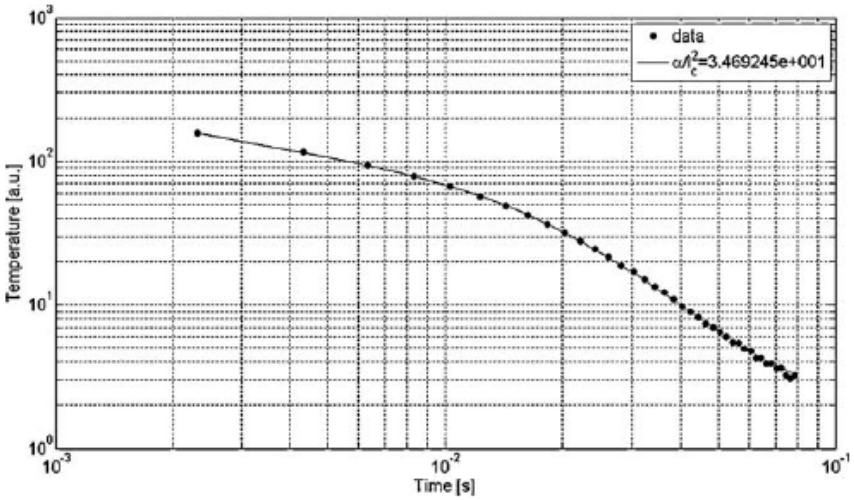

Fig. 7.42. Evolution of surface temperature as a function of time at the measurements and the best fitting curve for estimating the *through-the-thickness* thermal diffusivity of sample [71].

Thermal conductivity was calculated from eq. 6.3. The values of thermal diffusivity were from the experiment, whereas specific heat, c_p was found to be equal to 470 J/(kg·K) [81, 83] and density, ρ was estimated from the formula:

$$\rho = \rho_0 \cdot (1 - P) \qquad (7.1)$$

where:

ρ_0 – density for tetragonal yttria stabilized zirconia, equals 6050 kg/m^3

P – porosity

The values of thermal diffusivity and conductivity are shown in Table 7.13. These values are typical for those as sprayed porous nanostructured zirconia coatings [83]. Thermal diffusivity and conductivity increase with the increase of the spray distance. The coatings sprayed at the shortest distance of 40 mm conduct heat better than those sprayed using the distance of 60 mm. It can be related to low porosity and good contacts between the lamellas in these coatings, which is presented in the cross-sections of the coatings (Figs. 7.19 and 7.20).

Table 7.13. Experimentally determined thermal diffusivity (mean values from 10 measurements and standard deviations) and porosity and estimated values of thermal conductivity at room temperature for the samples sprayed in different runs [71].

Experimental run	Thickness, μm	Thermal diffusivity, 10^{-7} m^2/s	Porosity, %	Thermal conductivity, W/(m·K)
1	67 ± 7	2.95 ± 0.02	17.2 ± 0.8	0.69
2	127 ± 9	3.26 ± 0.02	12.9 ± 1.0	0.81
3	104 ± 8	3.79 ± 0.05	9.6 ± 0.5	0.97

Thermal diffusivity of 8YSZ and 24CeYSZ coatings have been measured with the Light Flash System, described in detail in chapter no. 6. The thermal diffusivity data for YSZ coatings are shown in Fig. 7.43. The samples sprayed in the run no. 2 have the greatest diffusivity and the samples sprayed in the run no. 4 – the lowest. Thermal diffusivity is the greatest for the porous samples and the porosity, in turn, decreases with the decrease of the spray distance (Table 7.14) [84].

Table 7.14. Results of thickness and porosity characterizations of suspension plasma sprayed 8YSZ coatings with spray parameters and coatings temperatures [84].

Exp. run	Thickness, mean value [μm]	Thickness, standard deviation [μm]	Porosity [%]	Scan velocity [mm/s]	Spray distance [mm]	Maximum surface temperature [°C]
1	100	0.9	9	300	40	570 – 690
2	106	1.5	8	500	40	490 – 650
3	54	0.9	9	400	50	460 – 530
4	51	2.9	10	300	60	410 – 570
5	60	4.5	12	500	60	380 – 460

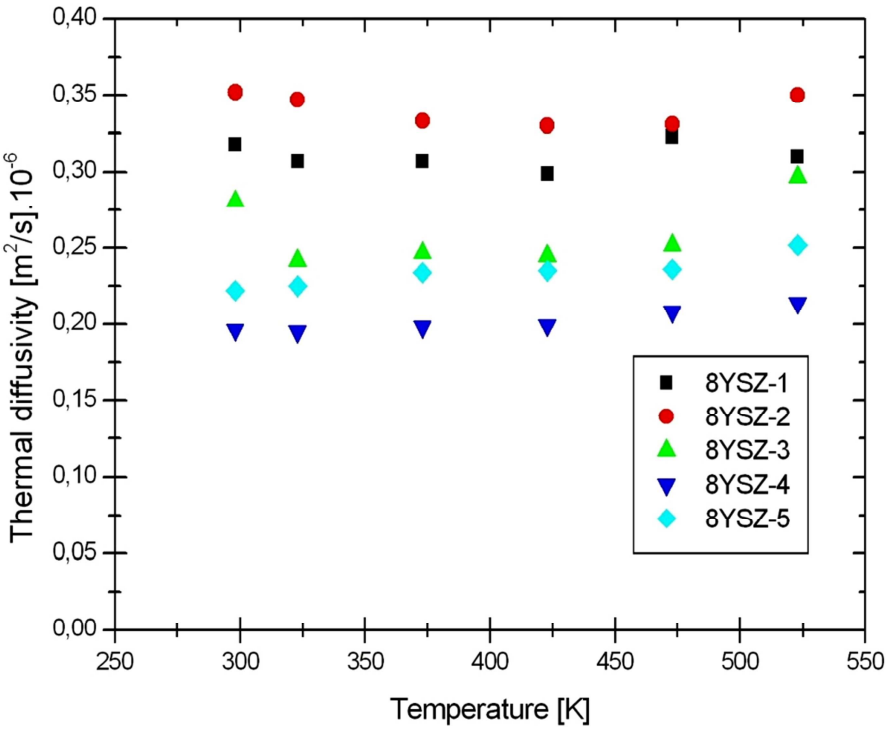

Fig. 7.43. Thermal diffusivity of 8YSZ coatings sprayed in different experimental runs [84].

Thermal diffusivity for 24CeYSZ coatings are shown in Fig. 7.44. As it can be seen, the samples sprayed in the run no. 4 have the greatest diffusivity, whereas the samples sprayed in the run no. 1 have the lowest. Similarly as in the case of 8YSZ coatings, thermal diffusivity is greater, when porosity of the coating is lower. And as it can be seen in Table 7.15, porosity decreases with the decrease of spray distance.

Table 7.15. Results of thickness and porosity characterizations of suspension plasma sprayed 24CeYSZ coatings with spray parameters and coatings temperatures.

Exp. run	Thickness, mean value [µm]	Thickness, standard deviation [µm]	Porosity [%]	Scan velocity [mm/s]	Spray distance [mm]	Maximum surface temperature [°C]
1	53	2.9	21.5	300	40	668 – 736
2	90	8.1	18.7	500	40	508 – 643
3	78	1.6	20.3	400	50	453 – 603
4	101	2.7	15.1	300	60	422 – 563
5	88	1.1	20.6	500	60	393 – 473

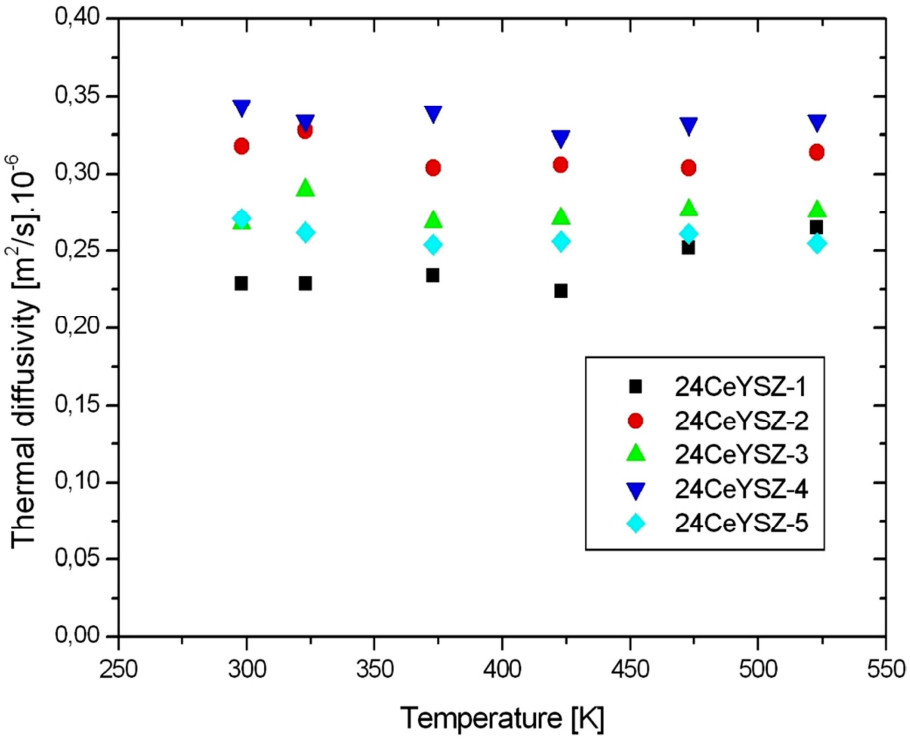

Fig. 7.44. Thermal diffusivity of 24CeYSZ coatings sprayed in different experimental runs.

Thermal conductivity was calculated with the use of eq. 6.5 using the specific heat and thermal expansion data collected in Table 7.16, for 8YSZ and 24CeYSZ coatings. The specific heat values were obtained from eq. 6.6, called Kopp-Neumann law.

Table 7.16. Thermal expansion and specific heat values used in calculations of thermal conductivity of 8YSZ and 24CeYSZ coatings [4.18, 4.19].

Temperature [K]	Specific heat c_p 8YSZ [J/kg·K]	Specific heat c_p 24CeYSZ [J/kg·K]	Thermal expansion — 8YSZ [–]	Thermal expansion — ZrO_2 [–]
298	438	427	$4.2606 \cdot 10^{-5}$	$3.4031 \cdot 10^{-5}$
323	453	441	$2.5646 \cdot 10^{-4}$	$2.0583 \cdot 10^{-4}$
373	480	465	$6.8840 \cdot 10^{-4}$	$5.5722 \cdot 10^{-4}$
423	501	485	$1.1262 \cdot 10^{-3}$	$9.1804 \cdot 10^{-4}$
473	518	501	$1.5702 \cdot 10^{-3}$	$1.2873 \cdot 10^{-3}$
523	531	514	$2.0206 \cdot 10^{-3}$	$1.6640 \cdot 10^{-3}$

The results of thermal conductivity are shown in Figs. 7.45 and 7.46 . The calculated values of thermal conductivity are in the range of 0.5 to 1.0 W/(m·K) in the measured temperatures for both types of ceramic coatings based on ZrO_2. Without the thermal dilatation

data for material ZrO_2 + 24 wt.% CeO_2 + 2.5 wt.% Y_2O_3 and after microstructural studies, in which tetragonal phase was more than 95% in coatings, probably with good approximation, thermal dilatation data for tetragonal ZrO_2 could be used. However, these results could include an error.

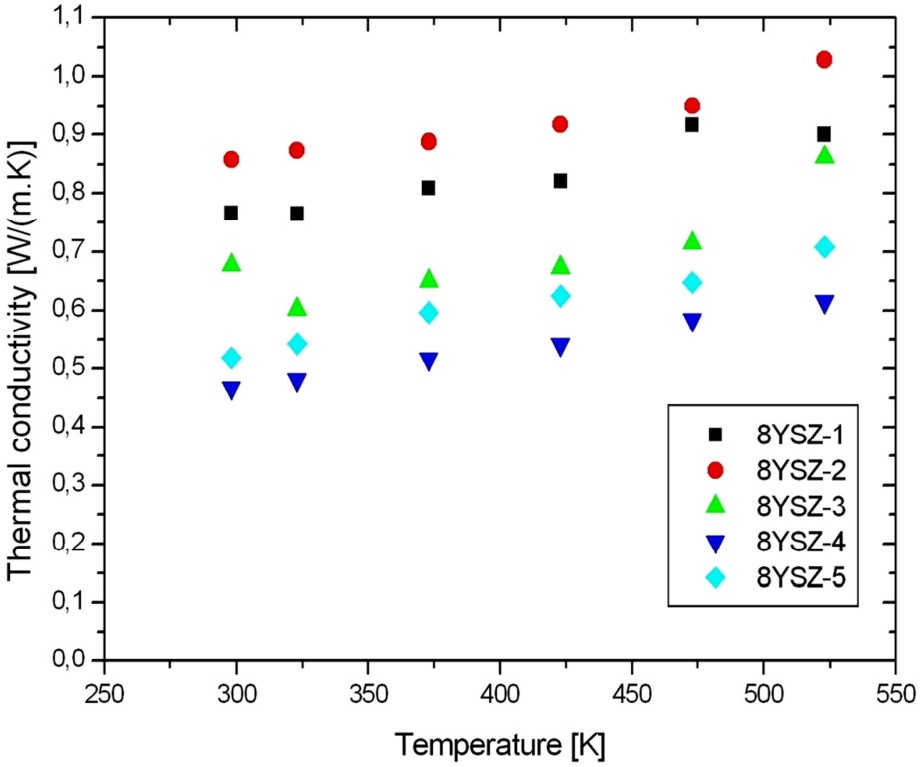

Fig. 7.45. Thermal conductivity of 8YSZ coatings sprayed in different experimental runs [84].

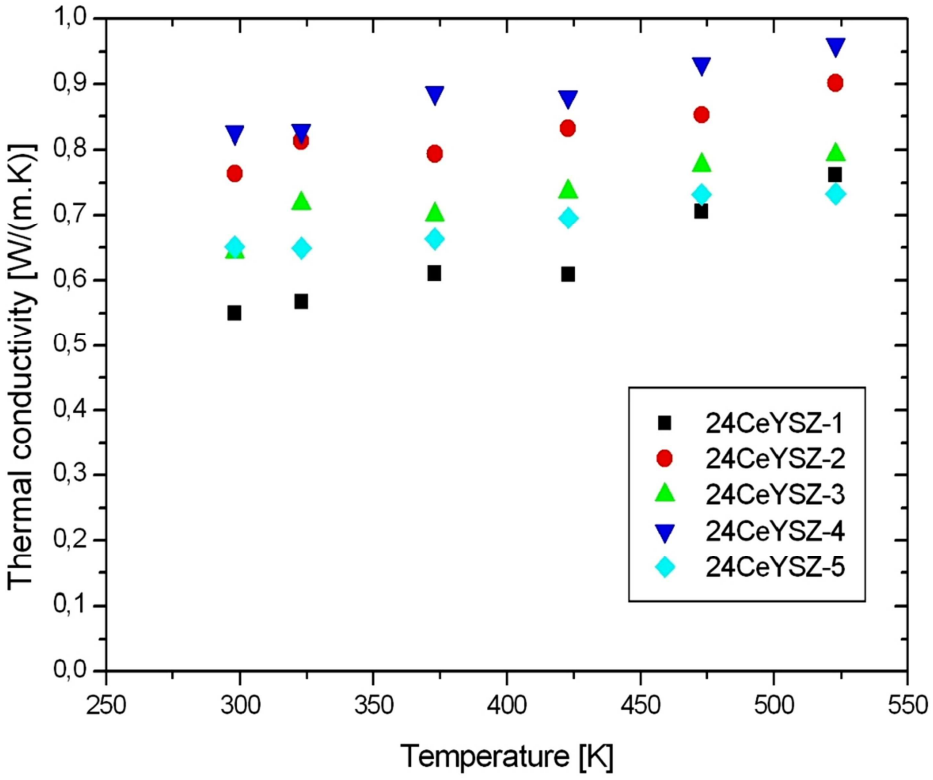

Fig. 7.46. Thermal conductivity of 24CeYSZ coatings sprayed in different experimental runs.

7.2.4. PHOTOCATALYTIC PROPERTIES

The photocatalytic activity of the titania samples (measured by Mrs. B. Leupolt in Fraunhofer Institute in Dresden) obtained using the internal injection mode of the suspension (with continuous jet injector) was determined by the degradation of dye methylene blue (MB), described in detail in chapter no. 2. The variation of the MB absorbance at λ = 664 nm for two different samples is shown in Fig. 7.47. The absorbance values of MB suffered no significant modifications while in the dark (no light). In presence of UV-irradiation the absorbance of MB decreased continuously. From these values of absorbance it was possible to determine the specific photocatalytic activity and photon efficiency of the samples using the eqs. 6.8–6.10 and to compare them with those of commercial Pilkington Active™ Glass [56].

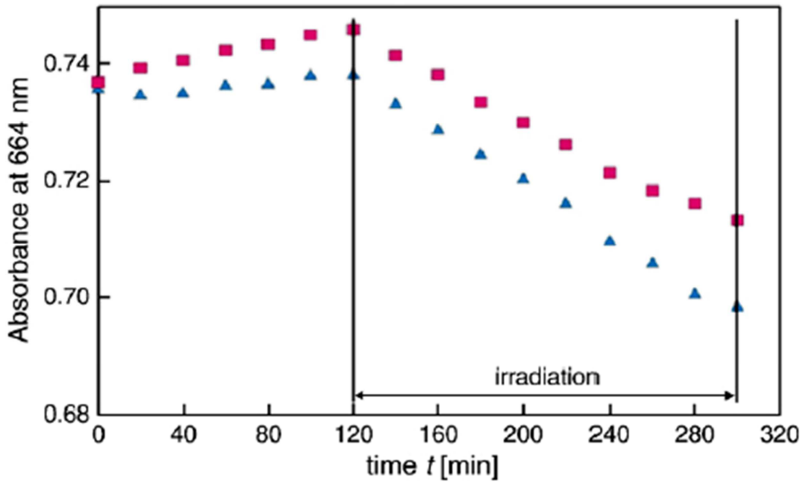

Fig. 7.47. Evolution of the MB absorbance during the photocatalytic test of the samples suspension plasma sprayed with internal injector in experimental runs no. 3 (▲) and no. 6 (■) [56].

The values of the specific photocatalytic activity and photon efficiency of internal injected suspension plasma sprayed coatings are shown in Fig. 7.48. The specific photocatalytic activity is in the range from $14 \cdot 10^{-6}$ to $35 \cdot 10^{-6}$ mol/($m^2 \cdot h$) if compared with Pilkington Active™ ($28 \cdot 10^{-6}$ mol/($m^2 \cdot h$)). The photon efficiency of the coatings varied from 0.022% to 0.032% when compared with that of Pilkington Active™ Glass (0.025%).

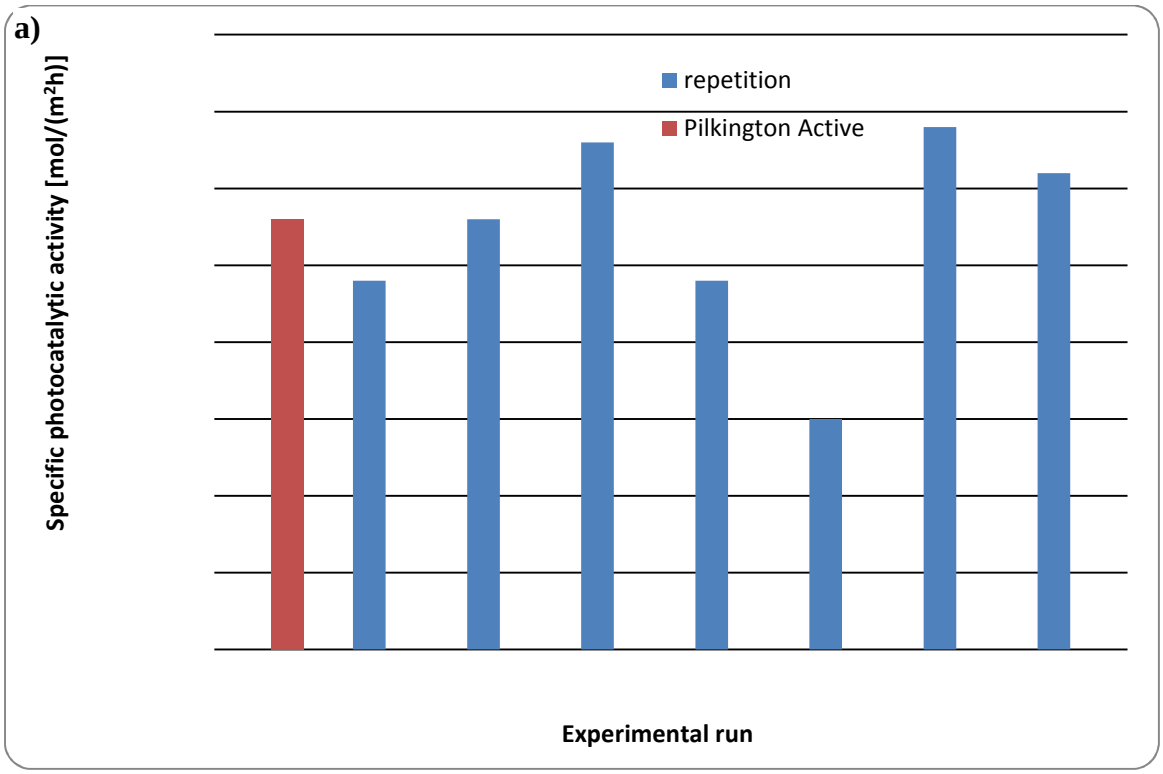

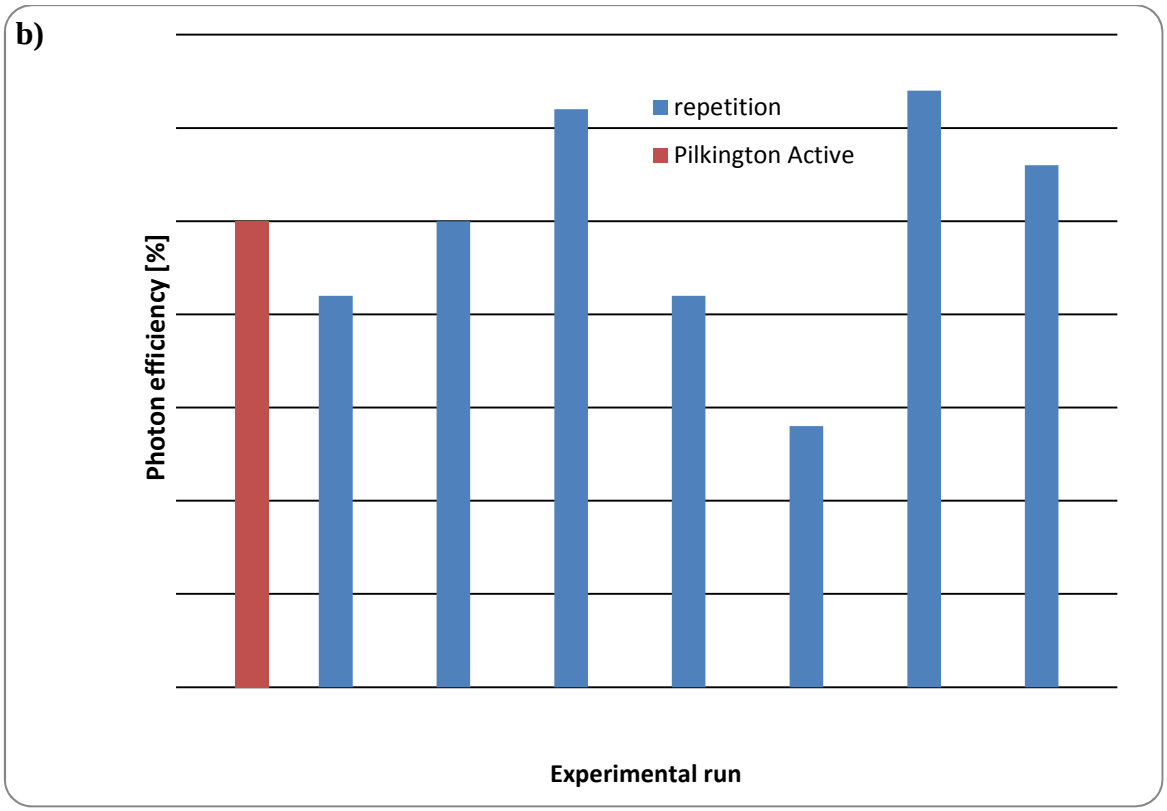

Fig. 7.48. Photocatalytic performances of suspension sprayed TiO_2 coatings using the internal injection mode during MB degradation: (a) specific photocatalytic activity; and (b) photon efficiency. The values are compared with that of commercial Pilkington Active™ Glass [56].

In general, better photocatalytic properties are associated with the higher anatase content in coating, e.g. [87]. In the case of coatings obtained with internal injection, this relation was not confirmed. It is easy to analyze this phenomenon by comparing Fig. 7.48. with Table 7.4.

The photocatalytic activity of the titania samples obtained on different substrates was determined with the same method, similarly to the previous ones. The initial investigations showed that in the presence of TiO_2 samples sprayed onto aluminum substrates, the concentration of MB decreased even without UV radiation. This decrease could have resulted from the absorption of the MB in the dense structure of the coating. Consequently, the photocatalytic tests were continued only for the samples sprayed onto stainless steel and titanium substrates. The values of the specific photocatalytic activity and photon efficiency of TiO_2 samples sprayed onto stainless steel and titanium are shown in Figs. 7.49 and 7.50, respectively. These values were compared with those of commercial Pilkington Active™ glass. Some measurements were repeated because during the photocatalytic tests, small titania flakes detached of the coatings.

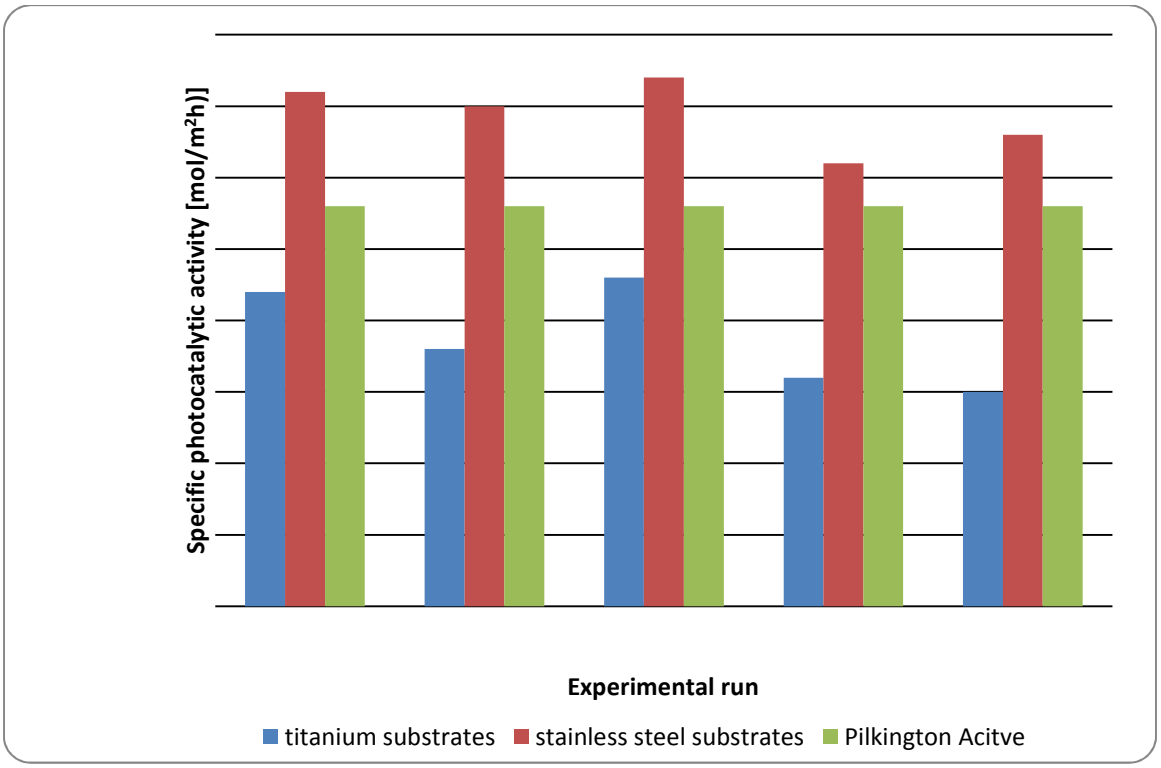

Fig. 7.49. Specific photocatalytic activity of suspension plasma sprayed TiO_2 coatings sprayed on titanium and stainless steel substrates in different experimental runs. The activity of commercial glass Pilkington Active™ is shown for comparison [75].

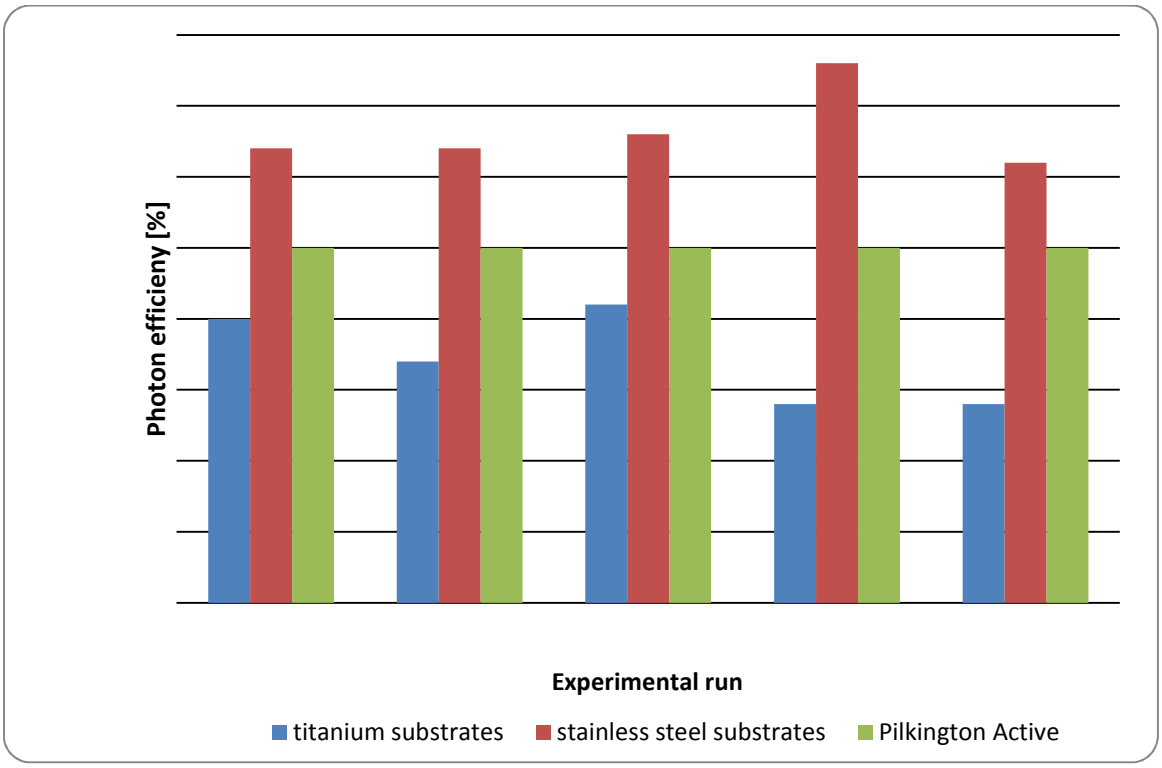

Fig. 7.50. Photon efficiency of suspension plasma sprayed TiO_2 coatings sprayed on titanium and stainless steel substrates in different experimental runs. The efficiency of commercial glass Pilkington Active™ is shown for comparison [75].

The results showed that the photocatalytic activity and photon efficiency could not be directly correlated with the anatase contents of the coatings. Actually the TiO_2 samples containing the highest anatase fraction, i.e. the coatings sprayed in run no. 1 onto stainless steel and in run no. 5 onto titanium substrate did not show the best photocatalytic performance. In this case, it is supposed, that the substrates could play an important role in the activity of the coatings. As depicted in Figs. 7.49 and 7.50, titania coatings sprayed onto stainless steel substrate were more active than those sprayed onto titanium ones. Moreover, the coatings sprayed onto stainless steel substrate indicate stronger photocatalytic activity than those of commercial Pilkington Active^{TM} glasses, independently of the spray parameters.

CHAPTER 8

DISCUSSION

This chapter deals with the discussion of the results presented in previous chapter. The chapter is divided into three parts, related to HA, TiO_2 and ceramics based on ZrO_2 coatings.

8.1. HYDROXYAPATITE COATINGS

The mechanical properties of suspension plasma sprayed HA coatings, which were tested *in vitro* conditions, are correlated with the coatings' microstructure. As it can be seen in Fig. 7.10, the HA coatings are composed of two different zones. The first one, the *dense zone* includes crystalline hydroxyapatite with its decomposition phases, such as tricalcium phosphate (TCP), tetracalcium phosphate (TTCP), CaO and others. The other one, the *sintered zone*, is composed of loosely bound (or sintered) initial hydroxyapatite grains. The soaking of the coatings in the simulated body fluid results in the dissolution of the fine hydroxyapatite grains from *sintered zone*, which is presented in Fig. 7.11. These fine grains were diluted also in all phases of the decomposition, from CaO, then β-TCP, TTCP and in the end α-TCP.

The effect of soaking in SBF on the adhesion of HA coatings, which was determined with the critical load in the scratch test, is a slight decrease of the initial value after 60 days of soaking. The elastic modulus of the HA coatings is independent of the number of days of soaking in SBF, but it depends only on the spray parameters, which is presented in Fig. 7.35. The mean value of the modulus is about 16 and 28 GPa for coatings sprayed in experimental run no. 1 and 2, respectively. These values are lower than the ones for coatings produced from coarse powder, as Fu et al. [88], who obtained E_m = 53 to 58 GPa for hydroxyapatite plasma sprayed coatings reinforced with ZrO_2 + 8 wt.% Y_2O_3. Also Chen et al. [89] obtained higher modulus equal to 72 GPa for sintered β-TCP. Cohesion in HA coatings, which was tested with the scratch test and determined with the scratch hardness, was found to be independent of the number of days of soaking in SBF, which is presented in Fig. 7.32. On the contrary,

Martens hardness, obtained from the indentation tests, which were made on the cross-sections of the coatings depends on the time of the soaking. This value increases with the soaking time (Fig. 7.36) from 0.2 to 0.6 and from 0.4 to 1 GPa for experimental run no. 1 and 2, respectively. The increase of microhardness in the function of the soaking time could be explained by the effect of fine grains dissolution in the SBF bath. It results that only the harder lamellae remain in the coatings.

8.2. TITANIUM DIOXIDE COATINGS

Discussion of the results for titanium dioxide coatings is divided into two parts, which are related to mechanical and photocatalytic properties.

8.2.1. MECHANICAL PROPERTIES

The mechanical properties of the suspension plasma sprayed titanium dioxide coatings were determined with the scratch test and given by critical loads and scratch hardness, which represented the coating adhesion to the substrate and cohesion in coatings, respectively. It was found, that microstructure of titania coatings is similar to the HA ones and is composed of the *dense and sintered zones*, which is presented in Figs. 7.16-7.18.

Scratch hardness and critical load depended mainly on the type of substrate. As it can be seen in Fig. 7.37, scratch hardness is much lower for aluminum substrate than for stainless steel and titanium ones. A similar tendency was observed with the critical load, which represented the adhesion parameter. The critical loads for aluminum substrate were equal or greater than 20 N, whereas for stainless steel and titanium substrates these loads were greater than 30 N in every experimental run. It could result in relatively important thickness of the coatings (about 50 μm).

8.2.2. PHOTOCATALYTIC PROPERTIES

The first process in the atomizing injection mode is to atomize suspension in fine droplets, which are smaller, than the ones obtained with the continuous-stream injector mode during the continuous jet breakup. These particles are agglomerated, sintered and they get molten in the plasma jet. Finally, the particles are significantly smaller than the ones, which are sprayed with the internal injection mode. Moreover, the fine and molten particles could

solidify during flight or after the impact on the substrate. There are two criteria of titania particles solidification: free energy of nucleation and interfacial energy between the solid and liquid phase. TiO_2 particles solidify either as anatase or rutile. The hypothetical temperatures of solidification, which correspond to the nucleation of anatase, lower than 2075 K were given by Li and Ishigaki [90]. On the other hand, the melting point of titania is equal to 2143 K and, consequently for the temperatures higher than 2075 K, melted particles solidify as a rutile phase [8]. The solidification temperature increase with decreasing undercooling effect. This phenomenon is effective for bigger particles. During solidification these particles are more intensively reheated by the flux of energy coming from the release of latent heat of fusion [56]. It is confirmed by this, that rutile is a major phase in the conventional plasma sprayed coatings from coarse powder. Obviously, while spraying of relatively coarse particles, formation of rutile is more possible. From this fact, the coatings sprayed with internal injection mode, which results in formation of large particles, exhibit a greater content of the rutile phase in comparison with the coatings sprayed with the atomizer injector.

A general assumption in the photocatalytic process is that the hydroxyl radicals (OH•) are responsible active groups for the photocatalytic degradation of pollutants. It is caused by their very high oxidation potential, which was determined by Koppenol and Liebman [91] to be in the range from 1.4 to 2.0 V. The ability of surface of the metallic oxides to adsorb water by the phenomena of physisorption and chemisortion is commonly known. According to Diebold [92], water molecules can be adsorbed to the surface by quite weak van der Waals bonds (hydrogen bonds) or more strongly by dissociation during the formation of surface hydroxyl groups. Electron and holes are photo-generated in conduction and valence bands, respectively by light excitation of titania with energy higher than the band gap, E_g, which is in range for 3.0 to 3.2 eV. These values correspond to UV-light with wavelength, λ, in the range from 360 to 380 nm. The excited groups diffuse to the oxide surface and are trapped there by adsorbed water and oxygen molecules, which is presented in Fig. 8.1. Photo-generated holes cause the oxidation process of water or OH- ions, which results in production of hydroxyl radicals. These radicals react with pollutants and oxidize them.

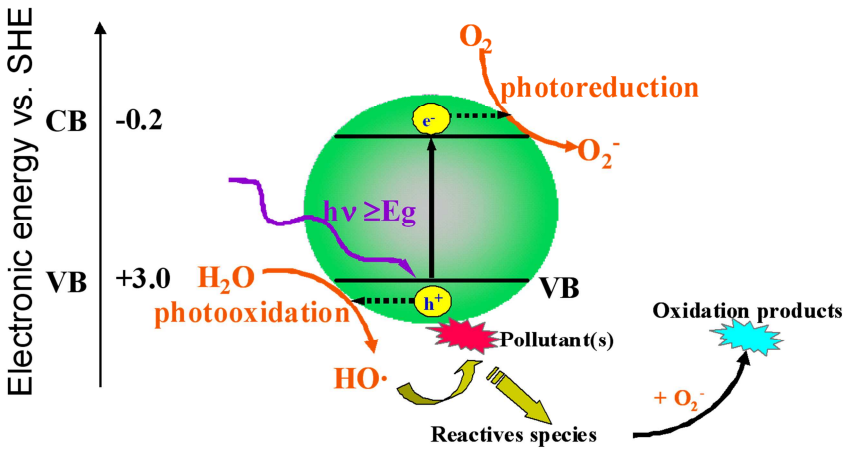

Fig. 8.1. Principle of the photocatalytic process on the TiO_2 particles [56].

Many researchers, e.g. [93, 94] have studied the mechanism of photocatalytic degradation of MB to clarify this process. Houas *et al.* [93] suggested, that the photocatalytic degradation pathway of MB occurs by the decyclization and mineralization of molecules under successive attacks of hydroxyl radicals, which is shown in Fig. 8.2a. On the other hand, Rauf *et al.* [94] proposed the explanation that the demethylation of MB occurs rather during the photocatalytic degradation process, which is presented in Fig. 8.2b.

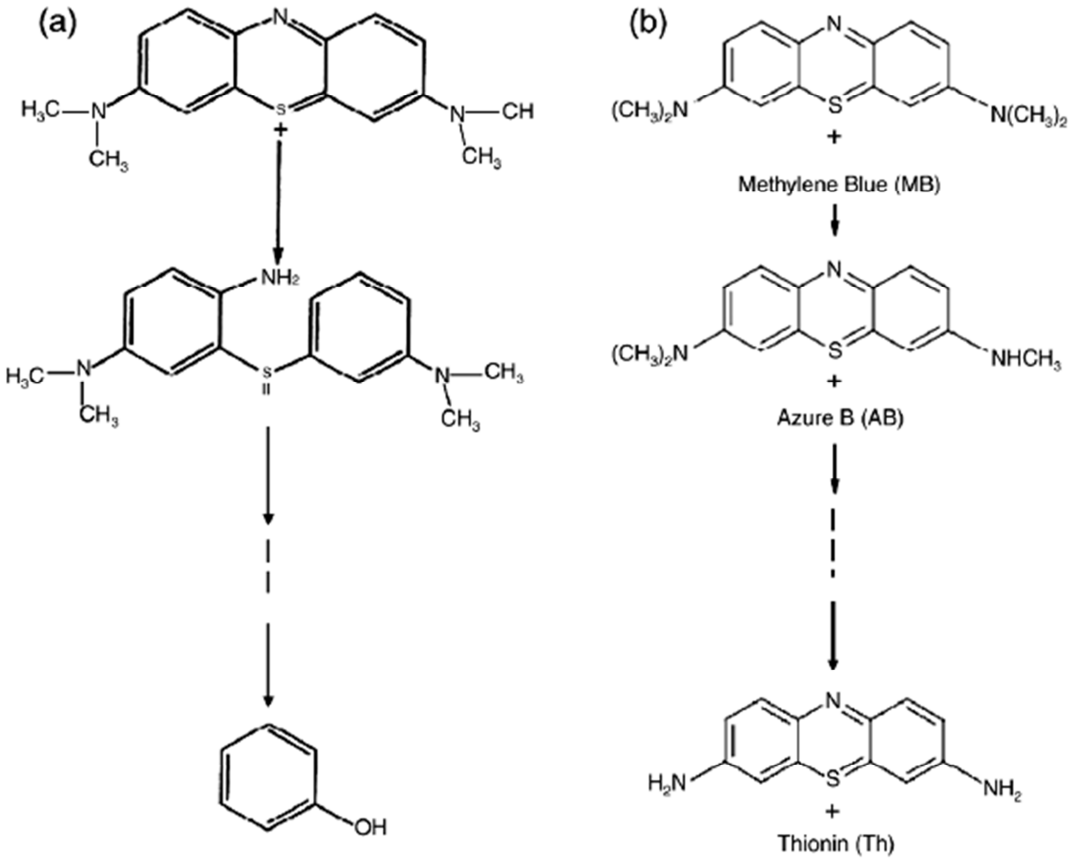

Fig. 8.2. Mechanism of photocatalytic degradation of MB following:
(a) decyclization and mineralization pathway; and (b) demethylation pathway [56].

The general opinion of the scientific community is namely that anatase is the phase more favorable to the photocatalytic properties than the rutile one. Some researchers [95 – 98] confirmed this opinion. However, the results of MB degradation do not confirm this. Coatings, in which the content of anatase was low, have greater specific photocatalytic activity than the commercial Pilkington Active™ Glass, which was adopted as a reference. This research showns, that photocatalytic properties of coatings are not correlated with their anatase content. It could be explained by other factors. One of them is the presence of the hydroxyl radicals [94]. The other factors could be porosity and roughness of coatings, because the higher specific surface area promoted the adsorption process. Also thickness of the coating could have an influence on these properties. The influence of type substrate, on which titania coatings were sprayed gave very interesting results. Photocatalytic properties were better for stainless steel substrates than for titanium ones. It could be explained by the difference in the deposition temperature, which was significantly higher for titanium substrates with the same spray parameters.

Finally, photocatalytic process takes place only on the very thin layer-surface of the coating. Also, as it was mentioned before, porosity in the surface, which results in higher specific surface area, improves the photocatalytic properties. This fact could explain the best photocatalytic performance of very porous coating (run no. 5 onto stainless steel substrate) from all produced coatings.

8.3. COATINGS BASED ON ZIRCONIUM OXIDE

The discussion of results for coatings based on zirconium oxide is divided into two parts, related to mechanical and thermal transport properties of these coatings.

8.3.1. MECHANICAL PROPERTIES

The microstructure of YSZ coatings is similarly composed of two zones, the *dense* and *sintered* one, but not the same, as in the case of hydroxyapatite or titania ones. As it can be seen in Fig 7.19a-c, well molten lamellas are the majority of YSZ coatings' microstructure. Well sintered small solids, which can be observed in Fig. 7.21a-c, are low percentage of the microstructure. Also the spray parameters, especially the spray distance, influences on the coatings' morphology. The shorter spray distance results in the better contact between lamellas, presented in Fig. 7.20a-c. Moreover, total porosity decrease, as well as agglomerated

particles are slightly better molten with the decreasing spray distance. On the other hand, the short spray distance results in the formation of vertical cracks, which are going through the entire thickness of the coatings, which come from relaxation of thermal stresses. The origin of these cracks takes place in the great heat flux, which for the spray distance equal to 40 mm could reach even 30 MW/m^2, in the case when the torch is static with regard to the substrate, as is reported by Etchart-Salas [99]. The heat flux significantly decreases with the increased spray distance and also, when the torch moves with regard to substrate. As it was reported in [100], heat flux was in the range from 0.1 to 0.5 MW/m^2 for the spray distance of 70 to 85 mm and the scan velocity of 250 to 500 mm/s.

Mechanical properties of the coatings sprayed from powder, which had a big grain size distribution were estimated with the scratch test. The results of adhesion and cohesion estimation show great differences between the samples sprayed in the same experimental run.

On the other hand, the coatings sprayed from the powders milled with changed parameters and addition of the dispersant agent exhibit better properties and a narrower distribution of values. For both series of coatings the scratch hardness was in range from 3 to even 6 GPa.

In the instrumented indentation test both, elastic modulus and Martens macrohardness depend on the spray parameters, especially the spray distance. In the case of 8YSZ coatings the highest values of HM are connected with the coatings sprayed from the shortest distance, equal to 40 mm. It is connected with the increase of the deposition temperature and, consequently in densification of coatings. The influence of second parameter, scan velocity, is practically invisible. On the other hand, in the case of 24CeYSZ coatings, both spray parameters influence the hardness value. The shorter spray distance and smaller scan velocity correspond to higher hardness of the coating. The elastic modulus reached the value equal to 130 GPa, which is close to the values obtained by Thompson and Clyne [101], who used coarse powder. Similar values of the elastic modulus for zirconia coatings were obtained by Vert *et al*. [102], who produced coatings with suspension plasma spraying. Elasticity modulus was the greatest for the greatest scan velocity and the shortest spray distance. It could be related in fractures of coatings in higher surface temperatures, which might result in the reduction of the elasticity modulus. The higher scan velocity slightly reduced the coating temperature.

Generally, scratch hardness as well as Martens macrohardness were smaller for 24CeYSZ coatings than for 8YSZ ones. It could result in a slightly greater porosity and number of cracks, which occur in the coatings with ceria.

8.3.2. THERMAL TRANSPORT PROPERTIES

Thermal conductivity of yttria stabilized zirconia suspension plasma sprayed coatings was in the range from 0.7 to 1.0 W/(m·K) (Table 7.13). These values depend on total porosity of coatings, which is a function of the spray distance. The obtained values of thermal conductivity are lower than those for the dense material ZrO_2 + 8 wt.% Y_2O_3, which was as high as 2 W/(m·K) [83]. The lower values of thermal conductivity result in the total porosity, which for YSZ coatings was in the range from 9.6 to 17.2 % (Table 7.13). The total porosity includes also bad contacts between the lamellas. But the lower values of thermal conductivity promoted these coatings for applications as thermal barriers.

The careful microstructure analysis shows the small grains inside the larger lamellae and microporosity. The total porosity for the coatings sprayed from the powders milled with changed parameters and with the dispersant agent is lower than that of for the coatings sprayed from the powder with big and bimodal grain size distribution. It should result in higher thermal conductivity values of the samples. But due to the microporosity, the thermal conductivity of 8YSZ coatings is lower than that of YSZ coatings sprayed previously with the same parameters. It is presented in Table 8.1.

Table 8.1. Comparison of porosity and thermal conductivity of YSZ (preliminary) and 8YSZ coatings obtained with the same spray parameters.

Samples code	Spray distance [mm]	Linear torch velocity [mm/s]	Porosity [%]	Thermal conductivity [W/m·K]
YSZ-1	60	300	17.2	0.69
8YSZ-4			10.0	0.47
YSZ-3	40	500	9.6	0.97
8YSZ-2			8.0	0.86

In the case of 24CeYSZ coatings, a similar tendency was observed. Also the total porosity, as well as microporosity have a great influence on the values of thermal conductivity. But thermal conductivity was calculated for the thermal dilatation coefficient for the tetragonal phase of ZrO_2, whose content was more than 95 % for every sample. The value of thermal dilatation coefficient for yttria with ceria stabilized zirconia (24 wt.% of CeO_2 and 2.5 wt.% of Y_2O_3) is no available.

CHAPTER 9

CONCLUSIONS

In this chapter the main conclusions are presented. The chapter is divided into three parts related to three different coatings types, HA, TiO_2 and ceramics based on ZrO_2 ones.

9.1. HYDROXYAPATITE COATINGS

1. Microstructure coatings sprayed from the suspension is different in comparison to conventional thermal spraying. It is composed of molten grains which correspond to the lamellas commonly observed in thermal spraying deposition and fine sintered or partially molten initial grains of hydroxyapatite. The sintered zone disappears after soaking in simulated body fluid.

2. Pores, which were observed in the coatings, after soaking in simulated body fluid get filled by the products of calcium phosphate reprecipitation.

3. Adhesion was higher for the coatings sprayed from the shorter distance. Also the distribution of values was more monomodal for the coatings sprayed from 50 mm.

4. The minimum value of the critical load was observed for the coatings sprayed in experimental run no. 1 and 2 after 14 days of soaking in the simulated body fluid.

5. The elastic modulus depends only on the operational spray parameters, especially on the spray distance. The time of the soaking in the simulated body fluid does not influence its value. The main value for coatings sprayed from 50 mm was equal to 28 GPa and it was almost two times higher than for the coatings sprayed from 60 mm, it was equal to 16 GPa.

6. The hardness of the hydroxyapatite coatings depends on the time of the soaking in the simulated body fluid and increases with the increasing soaking time. For the coatings sprayed from 50 mm the values were in range from 0.5 to 1.1 GPa and for the coatings sprayed from 60 mm from 0.2 to 0.6 GPa.

7. Scratch hardness does not change significantly with the time of soaking in the simulated body fluid for both series of the coatings. The values for coatings sprayed from 50 mm were slightly higher than for the ones sprayed from 60 mm.

8. The suspension plasma sprayed hydroxyapatite coatings onto titanium substrate could be used for bioactive coatings because of their good mechanical properties.

9.2. TITANIUM DIOXIDE COATINGS

1. A strong influence of the type of substrate on mechanical properties is observed. The values of the critical load were higher than the range of the measuring instrument for the coatings sprayed onto titanium and stainless steel substrates.

2. The scratch hardness for the coatings sprayed onto stainless steel substrates was in the range from 3.2 to 3.6 GPa, for the coatings sprayed onto titanium substrates was in the range from 3.5 to 3.8 GPa and for the coatings sprayed onto aluminum substrates was in range from 0.7 to 0.9 GPa.

3. The coatings sprayed with the internal injection system exhibit lower anatase friction (from 1.6 to 8.8 %) than the ones sprayed with the external atomizing system (from 9.4 to 15.4 %). It is caused probably by size of titania particles.

4. It was found, that the photocatalytic properties of suspension plasma sprayed coatings do not depend directly on the anatase content.

5. The influence of substrate on photocatalytic properties was observed. The coatings sprayed onto stainless steel substrates exhibit the best properties, better than commercial Pilkington Active™.

6. The suspension plasma sprayed titanium coatings could be used for photocatalytic surfaces because of their very good photocatalytic properties.

9.3. COATINGS BASED ON ZIRCONIUM OXIDE

1. The coatings sprayed from the powder with big grain size distribution exhibit a wide dispersion of the mechanical properties.

2. Better mechanical and thermal transport properties were found for the coatings sprayed from powders milled with changed parameters and addition of dispersant agent.

3. The hardness of 8YSZ coatings was in the range from 2.15 to 3.55 GPa and for 24CeYSZ coatings it was in the range from 1.97 to 3.26 GPa. The hardness increases with decreasing the spray distance.

4. The elastic modulus of 8YSZ coatings was in the range from 71 to 107 GPa and for 24CeYSZ coatings it was in the range from 68 to 130 GPa. The spray distance influences strongly the value of the elastic modulus.

5. The scratch hardness for 8YSZ coatings increases with the decreasing spray distance and it was in the range from 3 to 6 GPa. On the other hand for 24CeYSZ coatings was in range from 3 to 4 GPa and was independent on operational spray parameters.

6. The thermal conductivity for coatings sprayed from powder with big grain size distribution was in the range from 0.69 to 0.97 W/(m·K) in temperature 298 K. It increases with decreasing porosity.

7. The thermal conductivity for the coatings sprayed from the powder with narrower and monomodal grain size distribution was measured in the temperature range from 298 to 523 K. The values for both series of coatings were in the range from 0.5 to 1.0 W/(m·K).

8. Coatings sprayed from the powder with a big grain size distribution have higher thermal conductivity and also porosity values than the coatings sprayed from the powder with a narrower grain size distribution.

9. Suspension plasma sprayed coatings based on zirconium oxide could be used as thermal barrier coatings because of their small thermal conductivity values.

9.4. FURTHER RESEARCH

1. Further research concerning better use of scratch test to determine adhesion of suspension plasma sprayed coatings is required.

2. The photocatalytic properties should be determined by degradation another organic compounds, e.g. salicylic acid.

3. The thermal conductivity should be determined at temperatures up to 1300K, whereas the thermal shock resistance should be estimated for thermal barrier coatings.

4. The numerical studies are required to better understanding phenomena occurring in suspension plasma spraying and their influence on the process of coatings manufacturing and their properties.

5. It is necessary to find application of suspension plasma sprayed coatings in the other fields, e.g. fuel cells.

6. Examinations of hydroxyapatite coatings should be done *in vivo*.

The French Embassy in Poland financed the stay of author in France with agreement co-tutelle. Researches were partially financed by Ministry of Science and Higher Education of Poland, grant NN503 134138.

REFERENCES:

[1] Pawlowski L., *The science and engineering of thermal spray coatings*, 2nd ed. Wiley, Chichester, England, 2008.

[2] *An Introduction to Thermal Spray* – Sulzer Metco Bulletin

[3] Tomaszek R., *Suspension plasma spraying of functional gradient coatings*, PhD Thesis, ENSCL, 2006.

[4] Siegel R.W. Sci. Am. 275 (1996) 42.

[5] Pawlowski L., *Finely grained nanometric and submicrometric coatings by thermal spraying: A review*, Surface and Coatings Technology, 202 (2008) 4318-4328.

[6] Fauchais P., Montavon G., *Latest developments in suspension and liquid precursor thermal spraying*, Journal of Thermal Spray Technology, 19 (2010) 226-239.

[7] Kelsall R., Hamley I.W., Geoghegan M., *Nanotechnologie*, PWN Warszawa 2008.

[8] Pawlowski L., *Suspension and solution thermal spraying coatings*, Surface and Coatings Technology, 203 (2009) 2807-2829.

[9] Gitzhofer F., Bouyer E., Boulos M.I., *Suspension plasma spraying*, US Patent 5 609 921, 3 November 1997.

[10] Fauchais P., Etchart-Salas R., Rat V., Coudert J.F., Caron N., Wittmann-Teneze K., *Parameters controlling liquid plasma spraying: solutions, sols or suspensions*, Journal of Thermal Spray Technology, 17 (2008) 31-59.

[11] www.colloidal-dynamics.com – ZetaProbe and AcoustoSizer II instruction

[12] Zetasizer Nano Series, chapter 16, *Zeta Potential theory*

[13] Killinger A., Gadow R., Mauer G., Guignard A., Vassen R., Stover D., *Review of new developments in suspension and solution precursor thermal spray processes*, Journal of Thermal Spray Technology, 20 (2011) 677-695.

[14] Pawlowski L., *Corrigendum to "Finely grained nanometric and submicrometric coatings by thermal spraying: A review" [Surface and Coatings Technology, 202 (2008) 4318-4328]*, Surface and Coatings Technology, 203 (2008) 397.

[15] Cao X.Q., Vassen R., Stoever D., *Ceramic materials for thermal barrier coatings*, Journal of the European Ceramic Society, 24 (2004) 1-10.

[16] www.dynacer.com

[17] Bannier E., Darut G., Sanchez E., Denoirjean A., Bordes M.C., Salvador M.D., Rayon E., Ageorges H., *Microstructure and photocatalytic activity of suspension plasma sprayed TiO_2 coatings on steel and glass substrates*, Surface and Coatings Technology, 206 (2011) 378-386.

[18] www.nanoprotec.co.uk

[19] Vassen R., Kassner H., Mauer G., Stoever D., *Suspension plasma spraying: process characteristics and applications*, Journal of Thermal Spray Technology, 19 (2010) 219-225.

[20] Wang Y., Legoux J.-G., Neagu R., Hui R., Maric R., and Marple B.R., *Deposition of NiO/YSZ Composite and YSZ by Suspension Plasma Spray on Porous Metal*, Thermal Spray: Global Solutions for Future Application, Vol 264, May 3-5, 2010 (Singapore, DVS-Berichte), DVS Media, Du¨ sseldorf, Germany, 2010, p 446-453.

[21] Brousse E., Montavon G., Denoirjean A., Fauchais P., and Wittmann-Teneze K., *Gastight Yttria-Partially Stabilized Zirconia Layers Manufactured by Suspension Plasma Spraying for SOFC Electrolyte Functional Layers*, Thermal Spray 2009: Expanding Thermal Spray Performance to New Markets and Applications, May 4-7, 2009 (Las Vegas, Nevada, USA), B.R. Marple, M.M. Hyland, Y.-C. Lau, C.-J. Li, R.S. Lima, and G. Montavon, Ed., ASM International, Materials Park, Ohio, USA, 2009, p 120-125.

[22] Waldbilig D. and Kesler O., *The effect of solids and dispersant loadings on the suspension viscosities and deposition rates of suspension plasma sprayed YSZ coatings*, Surface and Coatings Technology, 203 (2009) 2098-2101.

[23] Marchand O., Bertrand P., Mougin J., Comminges C., Planche M.-P., Bertrand G., *Characterization of Suspension Plasma-Sprayed Solid Oxide Fuel Cell Electrodes*, Surface and Coatings Technology, 205 (2010) 993-998.

[24] Kassner H., Siegert R., Hathiramani D., Vassen R., Stoever D., *Application of Suspension Plasma Spraying (SPS) for Manufacture of Ceramic Coatings*, Journal of Thermal Spray Technology, 17 (2008) 115-123.

[25] Vassen R., Kassner H., Mauer G., Stoever D., *Suspension plasma spraying: process characteristics and applications*, Journal of Thermal Spray Technology, 19 (2010) 219-225.

[26] Vassen R., Hi Z., Kassner H., Stoever D., *Suspension plasma spraying of TiO_2 for the manufacture of photovoltaic cells*, Surface and Coatings Technology, 203 (2009) 2146-2149.

[27] Tingaud O., Bertrand P., Bertrand G., *Microstructure and tribological behavior of suspension plasma sprayed Al_2O_3 and Al_2O_3-YSZ composite coatings*, Surface and Coatings Technology, 205 (2010) 1004-1008.

[28] Oliker V.E., Terent'ev A.E., Shedova L.K., Martsenyuk I.S., *Use of aqueous suspensions in plasma spraying of alumina coatings*, Powder Metallurgy and Metal Ceramics, 48 (2009) 115-120.

[29] Darut G., Ageorges H., Denoirjean A., Montavon G., Fauchais P., *Effect of the structural scale of plasma sprayed alumina coatings on their friction coefficients*, Journal of Thermal Spray Technology, 17 (2008) 788-795.

[30] Chicot D., Tricoteaux A., *Mechanical Properties of Ceramics by Indentation: Principle and Applications*, in: Ceramic Materials, ed. W. Wunderlich, 115-153.

[31] Olivier W.C., Pharr G.M., *An improved technique for determining hardness and elastic modulus using load and displacement sensing indentation experiments*, Journal of Materials Research, 7 (1992) 1564-1583.

[32] Cheng Y.T., Cheng C.M., *Scaling dimensional analysis and indentation measurements*, Material Science and Engineering: R: Reports, 44 (2004) 91-149.

[33] Nix W.D., Gao H., *Indentation size effects in crystalline materials: A law for strain gradient plasticity*, Journal of the Mechanics and Physics of Solids, 46 (1998) 411-425.

[34] Buckle H. in: J.H. Westbrook, H. Conrad (Eds.), *The Science of Hardness Testing and Its Research Applications*, ASME, Metal Park, OH, p.453.

[35] Meyer E., *Untersuchen über Härteprüfung und Härte*. Z. Ver. deutscher Ing. Vol. 52 (1908), 645-654.

[36] Li H., Bradt R.C., *The microhardness indentation load/size effect in rutile and cassiterite single crystals*, Journal of Materials Research, 28 (1993) 917-926.

[37] Chicot D., *Hardness length-scale factor to model nano- and micro-indentation size effects*, Materials Science and Engineering: A, 499 (2009) 454-461.

[38] Durst K., Backes B., Goken M., *Indentation size effect in metallic materials: Correcting for the size of the plastic zone*, Scripta Materialia, 52 (2005) 1093-1097.

[39] Giannkopoulos A.E., Larson P.L., Vestergaard R., *Analysis of Vickers indentation*, International Journal of Solids and Structures, 31 (1994) 2679-2708.

[40] Giannkopoulos A.E., Larson P.L., *Analysis of pyramid indentation of pressure-sensitive hard metals and ceramics*, Mechanics of Materials, 25 (1997) 1-35.

[41] Zeng K., Chiu C.H., *An analysis of load-penetration curves from instrumented indentation*, Acta Materialia, 49 (2001) 3539-3551.

[42] Chicot D., Gil L., Silva K., Roudet F., Puchi-Cabrera E.S., Staia M.H., Teer D.G., *Thin film hardness determination using indentation loading curve modeling*, Thin Solid Films, 518 (2010), 5565-5571.

[43] Marshall D.B., Noma T., Evans A.G., *A simple method for determining elastic-modulus-to-hardness ratios using Knoop indentation measurements*, Journal of American Ceramic Society, 65 (1980) C175-C176.

[44] Doener M.F., Nix W.D., *A method of interpreting the data from the depth-sensing indentation instruments*, Journal of Materials Research, 1 (1986) 601-609.

[45] Chicot D., Roudet F., Zaoui A., Louis G., Lepingle V., *Influence of visco-elasto-plastic properties if magnetite on the elastic modulus: Multicyclic indentation and theoretical studies*, Materials Chemistry and Physics, 119 (2010) 75-81.

[46] King R.B., *Elastic analysis of some punch problems for layered medium*, International Journal of Solids and Structures, 23 (1987) 1657-1664.

[47] Dao M., Chollacoop M., Van Vliet K.J. Venkatesh T.A., Suresh S., *Computational modeling of the forward reverse problems in instrumented sharp indentation*, Acta Materialia, 49 (2001) 3899-3918.

[48] Antunes J.M., Menezes L.F., Fernandes J.V., *Three-dimensional numerical simulation of Vickers indentation tests*, International Journal of Solids and Structures, 43 (2006) 784-806.

[49] Hay J.C., Bolshakov A., Pharr G.M., *Critical examination of the fundamental relations used in the analysis of nano-indentation data*, Journal of Materials Research, 14 (1999) 2296-2305.

[50] Chicot D., Mendoza J., Zaoui A., Louis G., Lepingle V., Roudet F., Lesage J., *Mechanical properties of magnetite (Fe_3O_4), hematite (α-Fe_2O_3) and goethite (α-FeO·OH) by instrumented indentation and molecular dynamics analysis*, Materials Chemistry and Physics, 129 (2011) 863-870.

[51] **Łatka L.**, Chicot D., Cattini A., Pawlowski L., Ambroziak A., *Modeling of elastic modulus and hardness determination by indentation of porous yttria stabilized zirconia coatings*, Surface and Coatings Technology (in press).

[52] **Łatka L**., Pawlowski L., Chicot D., Pierlot C., Petit F., *Mechanical properties of suspension plasma sprayed hydroxyapatite coatings submitted to simulated body fluid*, Surface and Coatings Technology, 205 (2010) 954-960.

[53] Jaworski R., Pierlot C., Pawlowski L., Bigan M., Quivrin M., *Synthesis and Preliminary Tests of Suspension Plasma Spraying of Fine Hydroxyapatite Powder*, Journal of Thermal Spray Technology, 17 (5-6) (2008) 679-684.

[54] Jaworski R., Pierlot C., Pawlowski L., Bigan M., Martel M., *Design of the synthesis of fine HA powder for suspension plasma spraying*, Surface and Coatings Technology, 203 (2009) 2092-2097.

[55] Dyshlovenko S., Pateyron B., Pawlowski L., Murano D., *Numerical simulation of hydroxyapatite powder behavior in plasma jet*, Surface and Coatings Technology, 179 (2004) 110-117.

[56] Kozerski S., Toma F-L., Pawlowski L., Leupolt B., **Łatka L**., Berger L-M., *Suspension plasma sprayed TiO_2 coatings using different injectors and their photocatalytic properties,* Surface and Coatings Technology, 205 (2010) 980-986.

[57] Tomaszek R., Pawlowski L., Gengembre L., Laureyns J., Znamirowski Z., Zdanowski J., *Microstructural characterization of plasma sprayed TiO_2 functional coating with gradient of crystal grain size*, Surface and Coatings Technology 201 (2006) 45-56.

[58] www.azom.com

[59] *Material Product Data Sheet 8% Yttria Stabilized Zirconia Agglomerated and HOSP™ Thermal Spray Powders,* www.sulzermetco.com

[60] *Thermal Spray Materials Guide,* Sulzer Metco, www.sulzermetco.com

[61] www.labx.com

[62] Pierlot C., Pawlowski L., Bigan M., Chagnon P., *Design of experiments in thermal spraying: A review*, Surface and Coatings Technology, 202 (2008) 4483-4490.

[63] Kokubo T., Kushitani H., Sakka S., Kitsugi T., Yamamuro T., *Solutions able to reproduce in vivo surface-structure changes in bioactive glass-ceramic A-W3*, Journal of Biomedical Materials Research, 24 (1990) 721-734.

[64] d'Haese R., Pawlowski L., Bigan M., Jaworski R., Martel M., *Phase evolution of hydroxyapatite coatings suspension plasma sprayed using variable parameters in simulated body fluid*, Surface and Coatings Technology, 204 (2010) 1236-1246.

[65] Prevey P.S., *X-ray diffraction characterization of crystallinity and phase composition in plasma-sprayed hydroxyapatite coatings*, Journal of Thermal Spray Technology, 9 (2000) 369-376.

[66] ASTM 633-01, *Standard Test Method for Adhesion and Cohesion Strength of Thermal Sprayed Coatings*, March 10, 2001.

[67] polish standard *PN-EN 582:1993*

[68] Jaworski R., Pawlowski L., Roudet F., Kozerski S., Petit F., *Characterization of mechanical properties of suspension plasma sprayed TiO_2 coatings using scratch test*, Surface and Coatings Technology, 202 (2008) 2644-2653.

[69] *CSM Scratch Testers from CSM+ instruments*, www.csm-instruments.com

[70] Bison P., Cernuschi F., Grinzato E., Marinetti S., Robba D., *Ageing evaluation of thermal barrier coatings by thermal diffusivity*, Infrared Physics and Technology, 49 (2007) 286-291.

[71] Kozerski S., **Łatka L.**, Pawlowski L., Cernuschi F., Petit F., Pierlot C., Podlesak H., Laval J.P., *Preliminary study on suspension plasma sprayed ZrO_2 + 8 wt.% Y_2O_3 coatings*, Journal of the European Ceramic Society, 31 (2011) 2089-2098.

[72] Bison P., Cernuschi F., Grinzato E., *In-depth and in-plane thermal diffusivity measurements of thermal barrier coatings by IR camera: evaluation of ageing*, International Journal of Thermophysics, 29 (2008) 2149-2161.

[73] W.J. Parker, R.J. Jenkins, C.P. Butler, G.L. Abbott, *Flash method of determining thermal diffusivity, heat capacity, and thermal conductivity*, Journal of Applied Physics, 1961, 11 (9), 1679-84.

[74] www.civil.columbia.edu

[75] **Łatka L.**, Pawlowski L., Kozerski S., Toma F-L., Leupolt B., Berger L-M., *Photocatalytic properties of suspension plasma sprayed TiO_2 coatings obtained on different substrates*, Surface modification technologies XXIV : proceedings of the Twenty Fourth International Conference on Surface Modification Technologies, Dresden, Germany, September 7-9, 2010 / eds. T. S. Sudarshan, Eckhard Beyer, Lutz-Michael Berger. [Madras] : Valardocs, 2011. 95-106.

[76] Jaworski R., Pawlowski L., Roudet F., Kozerski S., Le Maguer A., *Influence of suspension plasma spraying process parameters on TiO_2 coatings microstructure*, Journal of Thermal Spray Technology, 17 (2008) 73-81.

[77] *Photocatalytic Activity of Surfaces – Determination of Photocatalytic Activity in Aqueous Medium by Degradation of Methylene Blue*, German Standard Draft, E DIN 52980:2007-11, in German.

[78] **Łatka L.**, Chicot D., Pawłowski L., Cattini A., Kozerski S., Petit F., Denoirjean A., *Mechanical properties of yttria and ceria stabilized zirconia coatings obtained by suspension plasma spraying*, ITSC2012, Houston, USA, may 21-24, 2012.

[79] Kozerski S., Pawlowski L., Jaworski R., Roudet F., Petit F., *Two zones microstructure of suspension plasma sprayed hydroxyapatite coatings*, Surface and Coatings Technology, 204 (2010) 1380-1387.

[80] Podlesak H., Pawlowski L., d'Haese R., Laureyns J., Lampke T., Bellayer S., *Advanced microstructural study of suspension plasma sprayed hydroxyapatite coatings*, Journal of Thermal Spray Technology, 19 (2010) 657-664.

[81] Ahmaniemi S., Vuoristo P., Mantyla T., Cernuschi F., Lorenzoni L., *Modified thick thermal barrier coatings, thermophysical characterization*, Journal of the European Ceramic Society, 24 (2004) 2669-2679.

[82] **Łatka L.**, Pawlowski L., Petit F., Kozerski S., *Scratch test mechanical properties of suspension plasma sprayed TiO_2 coatings*, ITSC 2011, Hamburg, Germany, September 27-29, 2011.

[83] Raghavan S., Wang H., Dinwiddie R.B., Porter W.D., Mayo M.J., *The effect of grain size, porosity and yttria content on the thermal conductivity of nanocrystalline zirconia*, Scripta Materialia, 39 (1998) 1119-1125.

[84] **Łatka L.**, Cattini A., Pawlowski L., Valette S., Pateyron B., Lecompte J.P., Kumar R., Denoirjean A., *Thermal diffusivity and conductivity of yttria stabilized zirconia coatings obtained by suspension plasma spraying*, Surface and Coatings Technology, 208 (2012) 87-91.

[85] Pankratz L.B., *Thermodynamic Properties of Elements and Oxides*, U. S. Bureau of Mines Bulletin, 1982, 672.

[86] Takeda Y., Tu H.Y., Sakaki H., Imanishi N., Yamamoto O., Philips M.B., Sommes N.M., *Gd1-xAxMnO3 (A = Ca and Sr) for the electrode of solid oxide fuel cells*, Journal of The Electrochemical Society, 144 (1997) 2810-2816.

[87] Toma F.-L., Berger L.-M., Stahr C.C., Naumann T., Langner S., *Microstructures and functional properties of suspension-spayed Al_2O_3 and TiO_2 coatings: An overview*, Journal of Thermal Spray Technology, 19 (2010) 262-274.

[88] Fu L., Khor K.A., Lim J.P., *Processing, microstructure and mechanical properties of yttria stabilized zirconia reinforced hydroxyapatite coatings*, Materials Science and Engineering A316 (2001) 46-51.

[89] Chen B., Zhang Z., Zhang J., Lin Q., Jiang D., *Fabrication and mechanical properties of β-TCP pieces by gel-casting method*, Materials Science and Engineering C28 (2008) 1052-1056.

[90] Li Y., Ishigaki T., *Thermodynamic analysis of nucleation of anatase and rutile from TiO_2 melt*, Journal of Crystal Growth 242 (2002) 511-516.

[91] Koppenol W.H., Liebman J.F., *The oxidizing nature of the hydroxyl radical. A comparison with the ferryl ion (FeO_2+)*, Journal of Physical Chemistry, 88 (1984) 99-101.

[92] Diebold U., *The surface of titanium dioxide*, Surface Science Reports, 48 (2003) 53-229.

[93] Houas A., Lachheb H., Ksibi M., Elaloui E., Guilard C., Herrmann J-M., *Photocatalytic degradation pathway of methylene blue in water*, Applied Catalysis B: Environmental 31 (2001) 145-157.

[94] Rauf M.A., Meetani M.A., Khallel A., Ahmed A., *Photocatalytic degradation of methylene blue using a mixed catalyst and product analysis by LC/MS*, Chemical Engineering Journal, 157 (2010) 373-378.

[95] Xu M., Gao Y., Moreno E.M., Kunst M., Muhler M., Wang Y., Idriss H., Woll Ch., *Photocatalytic activity of bulk TiO_2 anatase and rutile single crystals using infrared absorption spectroscopy*, Physical Review Letters, 106 (2011) 138302.

[96] Safarzadeh-Amiri A., Boltor J.R., Cater S.R., *The use of iron in advanced oxidation processes*, Journal of Advanced Oxidation Technologies, 29 (1996) 18-26.

[97] Tanaka K., Capule M.F.V., Hisanaga T., *Effect of crystallinity of TiO_2 on its photocatalytic action*, Chemical Physics Letters, 187 (1991) 73-76.

[98] Linsebigler A.L., Lu G.Q., Yates J.T., *Photocatalysis on TiO_2 surfaces: principles, mechanisms and selected results*, Chemical Reviews, 95 (1995) 735-758.

[99] Etchart-Salas R., PhD Thesis, *Projection par plasma d'arc de particules submicroniques en suspension. Approche expérimentale et analytique des phénomènes impliqués dans la reproductibilité et la qualité des dépôts*, University of Limoges 2007, in French.

[100] **Łatka L.**, Goryachev S.B., Kozerski S., Pawlowski L., *Sintering of fine particles in suspension plasma sprayed coatings*, Materials (open access journal), 3 (2010) 3845-3866.

[101] Thompson J.A., Clyne T.W., *The effect of heat treatment on the stiffness of zirconia top coats in plasma sprayed TBCs*, Acta Materialia, 49 (2001) 1565-1575.

[102] Vert R., Chicot D., Decoopman X., Gruescu I.C., Meillot E., Vardelle A., Mariaux G., *Adhesive and cohesive properties of nanostructured ZrO_2 coatings by the original Vickers Indentation Cracking technique*, Thin Solid Films, 519 (2011) 7789-7795.